2012

Chemical crystallography at the interface of physics, chemistry, and in engineering: structure determination of highly correlated extended solids, main group compounds, coordination complexes, and bioceramics

Gregory Todd McCandless
Louisiana State University and Agricultural and Mechanical College

CHEMICAL CRYSTALLOGRAPHY AT THE INTERFACE OF PHYSICS, CHEMISTRY, AND ENGINEERING: STRUCTURE DETERMINATION OF HIGHLY CORRELATED EXTENDED SOLIDS, MAIN GROUP COMPOUNDS, COORDINATION COMPLEXES, AND BIOCERAMICS

A Dissertation

Submitted to the Graduate Faculty of the
Louisiana State University and
Agricultural and Mechanical College
in partial fulfillment of the
requirements for the degree of
Doctor of Philosophy

in

The Department of Chemistry

by
Gregory Todd McCandless
B.S., Louisiana State University, 1999
M.S., Louisiana State University, 2008
December 2012

ACKNOWLEDGEMENTS

TABLE OF CONTENTS

ABSTRACT

Multi-disciplinary research is essential to address the major challenges in science, engineering, and medicine. For these three areas, crystallography has played and continues to play a huge role by providing researchers with the means to determine the structure of a compound and relate these to its properties. This dissertation is highly interdisciplinary, focusing on structure determination of complex systems and materials with tailored applications. This work includes the characterization by single crystal and powder X-ray diffraction of intermetallic extended solids, layered metal oxides, inorganic complexes, discrete organic molecules, and bioceramics.

These projects range from modeling translational disorder with pseudo-hexagonal symmetry ($Yb_2Pd_3Ga_9$), determining the influence of chemical doping on structure and physical properties (P-, Yb-, Co-, and Cu-doping of $CaFe_4As_3$ and Mn-doping of $Sr_3Ru_2O_7$), elucidating the structure of transition metal corrole complexes to understand its regioselectivity of various substituents and its electrochemical tenability, unmasking a high temperature binary polymorph (CoAs), identifying a minor organic product (dimer of two planar fused-carbon ring moieties) that may help mechanistically how to improve synthetic yields, and developing implants from porous, biodegradeable, and mechanically strong scaffolded composite materials (akermanite and poly-ε-caprolactone) for bone tissue regeneration. Knowing what is structurally important in a compound and how to best obtain this information are both vital in the process of revealing the structure and making property correlations.

CHAPTER 1

INTRODUCTION – A SYMMETRY OBSERVED

> I can remember the exact spot on the Backs where
> the idea suddenly leapt into my mind that Laue's
> spots were due to the reflection of X-ray pulses by
> sheets of atoms in the crystal.[1]
> - William Lawrence Bragg

That autumn day in 1912 along the Cambridge riverside (or the "Backs") while he was a

graduate student at Trinity College under the direction of Nobel Laureate J. J. Thomson (Physics,

1906), William Lawrence Bragg would interpret Max von Laue's X-ray diffraction experiments

(**Figure 1.1**) with single crystals – experiments that would lead to Laue winning the 1914 Nobel

Prize in Physics – into a single equation that would revolutionize the structural determination of

both naturally occurring and synthetic crystalline compounds. Bragg's Law would simplify

Laue's attempts to calculate the periodic arrangement of atoms in a single crystal by relating the

a)

b)
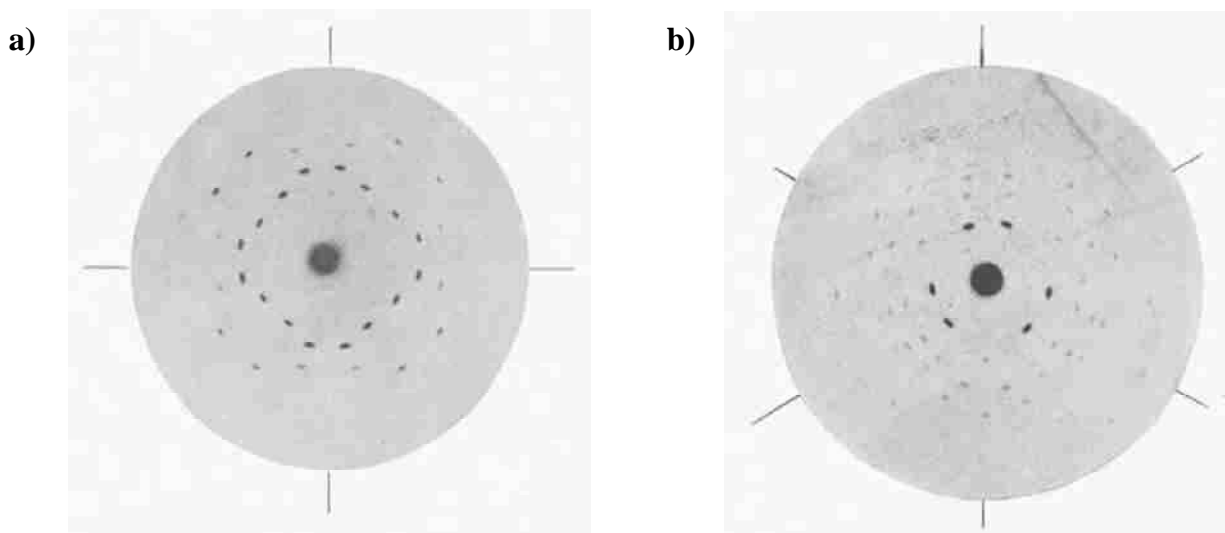
Figure 1.1. Laue's diffraction image of sphalerite (ZnS) along four-fold and three-fold axes
(as obtained from Friedrich, W.; Knipping, P.; Laue, M. *Interferenzscheinungen
bei Röntgenstrahlen*; Verlag der Königlich-Bayerischen Akademie der
Wissenschaften: München, 1912).[2]

spacing between successive parallel diffraction (*hkl*) planes, d, with the "glancing" angle, θ, and the wavelength, λ, of the X-ray source (**Figure 1.2**). After Bragg's landmark paper[3] (accepted on November 11, 1912…three months prior to Von Georg Wulff's publication[4] with a similar equation), Bragg, with his father, William Henry Bragg, solved the structure of a variety of crystals, such as halite (NaCl),[5-7] potassium ferrocyanide ($K_4[Fe(CN)_6] \cdot 3H_2O$),[5] calcite ($CaCO_3$),[5-7] pyrite ($FeS_2$),[5-7] sphalerite (ZnS),[5-7] potassium dichromate ($K_2Cr_2O_7$),[5] sylvite (KCl),[6] potassium bromide (KBr),[6] fluorite (CaF_2),[6,7] sodium nitrate ($NaNO_3$),[7] dolomite ($CaMg(CO_3)_2$),[7] rhodochrosite ($MnCO_3$),[7] siderite ($FeCO_3$),[7] diamond (C),[8] and copper (Cu),[9] that would demonstrate the versatility of this remarkable equation which would lead to garnering the 1915 Nobel Prize in Physics "for their services in the analysis of crystal structure by means of X-rays".[1]
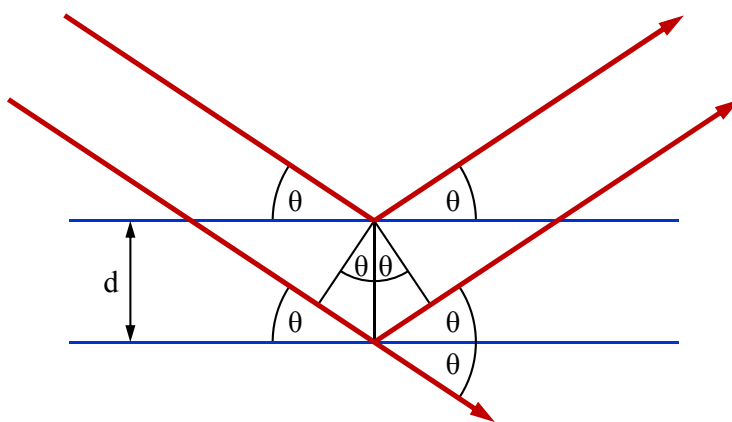
Figure 1.2.   Schematic diagram depicting Bragg's Law: $n\lambda = 2d \sin\theta$ (where n = 1, 2, 3…).

The ability to accurately identify a crystalline product from its pattern of diffraction (see **Figure 1.3**) and determine its structure with diffraction experiments is valuable to every area of science, engineering, and medicine. The range is vast in the types of compounds that can be characterized and, therefore, crystallography has made a tremendous contribution in a number of high-impact research discoveries. This is also evident by the 26 crystallography related Nobel

Prizes awarded to date (from the discovery of X-rays by Wilhelm Conrad Röntgen, the first

Nobel Prize in Physics in 1901, to the discovery of quasicrystals by Daniel Shechtman, the

Nobel Prize in Chemistry 2011).[10]
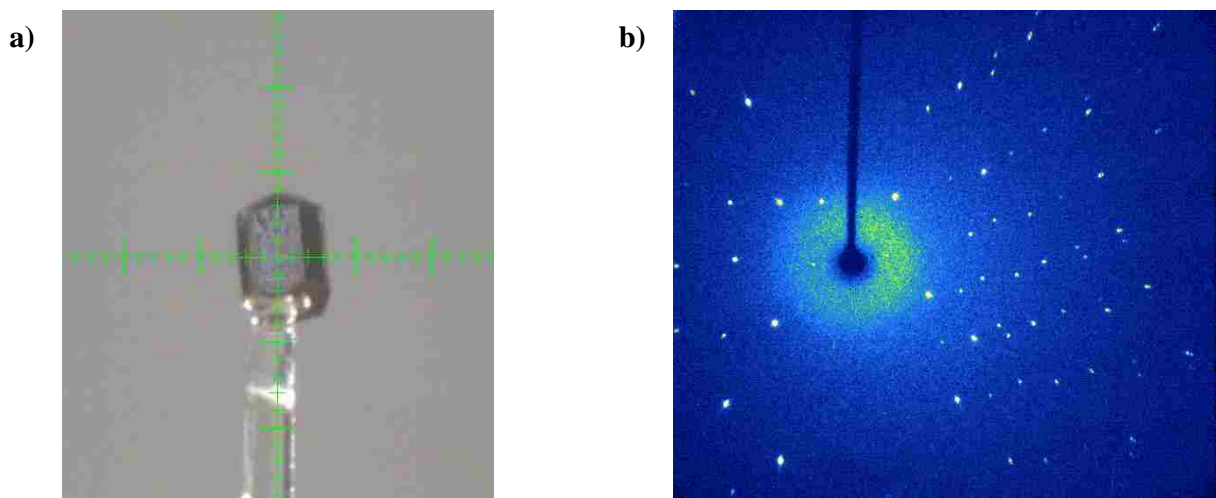
Figure 1.3.   a) A mounted crystal of FeCrAs (each small division line = 0.05 mm) and b) its diffraction image of a phi scan of 15° (MoKα radiation source, λ = 0.71073 Å).

This dissertation is highly interdisciplinary, focusing on structure determination of

complex systems and materials with tailored applications.   This work includes the

characterization of intermetallic extended solids, layered metal oxides, inorganic complexes,

discrete organic molecules, and bioceramics. The diverse nature of these investigations has led

to collaboration with researchers in chemistry, physics, engineering, and biomedicine. Knowing

what is structurally important in a compound and how to best obtain this information are both

vital in the process of revealing the structure and making property correlations.

A selection of projects will be covered in this dissertation with emphasis on the structure

determination and demonstrating the challenges as well as the current limits of crystallography.

This selection begins with the structure of $Yb_2Pd_3Ga_9$, which does not adopt the $Y_2Co_3Ga_9$

structure-type, even though there are several 2-3-9 ternary phases – gallides and aluminides –

that do. The key to solving this structure was the observation of translational disorder and the subsequent misleading selection of pseudo-hexagonal symmetry which led others to suggest $Yb_2Pd_3Ga_9$ adopts a new hexagonal structure-type.

A series containing Yb-, P-, Co-, and Cu-doped $CaFe_4As_3$ compounds show the significant effect of chemical pressure on the physical properties of the material even when the structural changes are very small (or, in some cases, statistically insignificant). An attempt to synthesize a new Ba-Co-As phase would lead to a structure-type investigation to unmask the identity of a high-temperature polymorph.

Attention will then be focused on a Ruddlesden-Popper phase, $Sr_3Ru_2O_7$, and a series of Mn-doped $Sr_3Ru_2O_7$ compounds. The influence of Mn-doping on the RuO_6 octahedral rotation and metal-to-insulator transition will be discussed after a thorough structure determination of the Ru end-member and a study of its temperature dependence.

In addition to extended solids, the structure determination of the transition metal complex family of corroles will be presented with emphasis on the analysis of the bonding, conformation, and crystal packing of a 5-coordinate Fe corrole with *meso*-phenyl and β-NO_2 substituents. The elucidation of this complex's structure is beneficial towards the design of chemical sensors with tunable electrochemical properties.

The structure of a highly conjugated organic dimer of two planar tetracyclic pyracene frameworks was also determined. This discrete molecule was a minor product during the synthesis of fullerene fragments, and two halves of this compound are twisted by ~51° along the central C=C bond. Discussion of the planarity of the fused carbon rings, out-of-plane deviation of peripheral substituents, unusual bond lengths, and intermolecular carbonyl-carbonyl interactions (both antiparallel and parallel) are provided.

The final project in this dissertation focused on synthesis and characterization of composite scaffolds containing both bioceramic and polymeric materials. These scaffolds are developed for the use as moldable implants for bone tissue regeneration. Our goal is to design scaffolds that are highly porous, biodegradeable, and mechanically strong enough for load-bearing applications. A ceramic method was established for $CaO-MgO-SiO_2$ phases using powder X-ray diffraction to evaluate sample homogeneity. Preliminary *in vitro* results using composites of akermanite and poly-ε-caprolactone have promise.

1.1 References

(1)   "The Nobel Prize in Physics 1915 - Perspectives". Nobelprize.org. http://www.nobelprize.org/nobel_prizes/physics/laureates/1915/perspectives.html (accessed Sept 18, 2012).

(2)   Friedrich, W.; Knipping, P.; Laue, M. *Interferenzerscheinungen bei Röntgenstrahlen*; Verlag der Königlich-Bayerischen Akademie der Wissenschaften: München, 1912.

(3)   Bragg, W. L. *Proc. Cambridge Philos. Soc.* **1913**, *17*, 43-57.

(4)   Wulff, G. *Physik. Zeitschr.* **1913**, *14*, 217-220.

(5)   Bragg, W. H.; Bragg, W. L. *Proc. R. Soc. Lond. Ser. A-Contain. Pap. Math. Phys. Character* **1913**, *88*, 428-438.

(6)   Bragg, W. L. *Proc. R. Soc. Lond. Ser. A-Contain. Pap. Math. Phys. Character* **1913**, *89*, 248-277.

(7)   Bragg, W. L. *Proc. R. Soc. Lond. Ser. A-Contain. Pap. Math. Phys. Character* **1914**, *89*, 468-489.

(8)   Bragg, W. H.; Bragg, W. L. *Nature* **1913**, *91*, 557-557.

(9)   Bragg, W. L. *Philos. Mag.* **1914**, *28*, 355-360.

(10)   "The Nobel Prizes". Nobelprize.org. http://www.nobelprize.org/nobel_prizes/ (accessed Sept 18, 2012).

STRUCTURE DETERMINATION OF Yb$_2$Pd$_3$Ga$_9$ WITH TRANSLATIONAL DISORDER AND MISLEADING PSEUDO-HEXAGONAL SYMMETRY

2.1   Introduction

Recent exploratory synthesis of Yb-based intermetallics yielded single crystals of Yb$_2$Pd$_3$Ga$_9$. Considering the list of ternary compounds (gallides and aluminides)[1-9] that adopt the Y$_2$Co$_3$Ga$_9$ structure-type[10] (orthorhombic, *Cmcm*), it was surprising that unit cell determinations for single crystal X-ray diffraction data consistently indicated hexagonal lattice parameters ($a = b \neq c$, $\alpha = \beta = 90°$, $\gamma = 120°$). In support of this unexpected crystal system, there are allusions in the literature[7,11] to dissertation work[12,13] on this compound as a "new structure-type" (hexagonal, $P6_122$). Unfortunately, neither models based on the ordered orthorhombic Y$_2$Co$_3$Ga$_9$ structure-type, nor the "new hexagonal structure-type" are a good fit to the data collected from single crystals that diffract well, have decent crystal mosaicity ($\sim 0.4°$), and do not show obvious signs of twinning. After several other possibilities were ruled out, the structure determination of Yb$_2$Pd$_3$Ga$_9$ proved to have similarities to a pair of aluminides (Ho$_2$Rh$_3$Al$_9$ and Er$_2$Ir$_3$Al$_9$) with translational (or positional) disorder.[14]

2.2   Experimental Details

For the crystals supplied by my collaborators, the following synthesis protocol was used: "Yb, Pd, and Ga elements with purities greater than 99.9% were weighed out in the molar ratio 1.5 : 1 : 15, heated at a rate of 150 K h^{-1} to 1423 K, and dwelled for 7 h. The samples were then rapidly cooled (150 K h^{-1}) to 773 K and, finally, slow cooled to 673 K at a rate of 8 K h^{-1}. The

---

samples were then inverted and centrifuged to separate crystals from excess gallium flux. The resulting crystals were metallic silver in color with typical dimensions of ~ 2 x 2 x 3 mm^3 [(**Figure 2.1**)]."[15]

Figure 2.1. Crystals of Yb$_2$Pd$_3$Ga$_9$ (red gridlines for inset picture represent 1 mm scale).

A crystal with sufficient size (0.05 x 0.05 x 0.05 mm^3) was used to collect room temperature single-crystal X-ray diffraction data. Diffraction images were collected on a Nonius KappaCCD X-ray diffractometer with Mo Kα radiation source (λ = 0.71073 Å) and a graphite monochromator. HKL Denzo and Scalepack were used for indexing *hkl* reflections, initial unit cell determination, and correcting absorption (multi-scan method).[16] SIR97[17] generated preliminary starting models and extensive refinement was carried out using SHELXL-97.[18] The ADDSYM option within PLATON[19] was employed to locate missing symmetry, obtain space group suggestions, and generate unit cell transformation matrices.

2.3   Results and Discussion

"Difficulties in the refinement of the crystal structure led to a literature search for other structurally related 2-3-9 intermetallic compounds. This search yielded a list of compounds adopting the orthorhombic $Y_2Co_3Ga_9$ structure-type[10] (*Cmcm*, No. 63) which have been reported for the ternary aluminides ($Ce_2Rh_3Al_9$,[1] $Gd_2Ir_3Al_9$,[2] $Nd_2Co_3Al_9$,[3] and $U_2Co_3Al_9$[4]), and the ternary gallides ($Y_2Rh_3Ga_9$,[5,6] $Eu_2Rh_3Ga_9$,[7] $Eu_2Ir_3Ga_9$,[7] $Dy_2Ru_3Ga_9$,[8] $Ho_2Co_3Ga_9$,[10] and $Lu_2Rh_3Ga_9$[9])."[15] A rendering of this structure-type is depicted in **Figure 2.2** with local point group symmetry shown in **Figure 2.3** and **Figure 2.4** for two non-equivalent transition metal polyhedra and rare
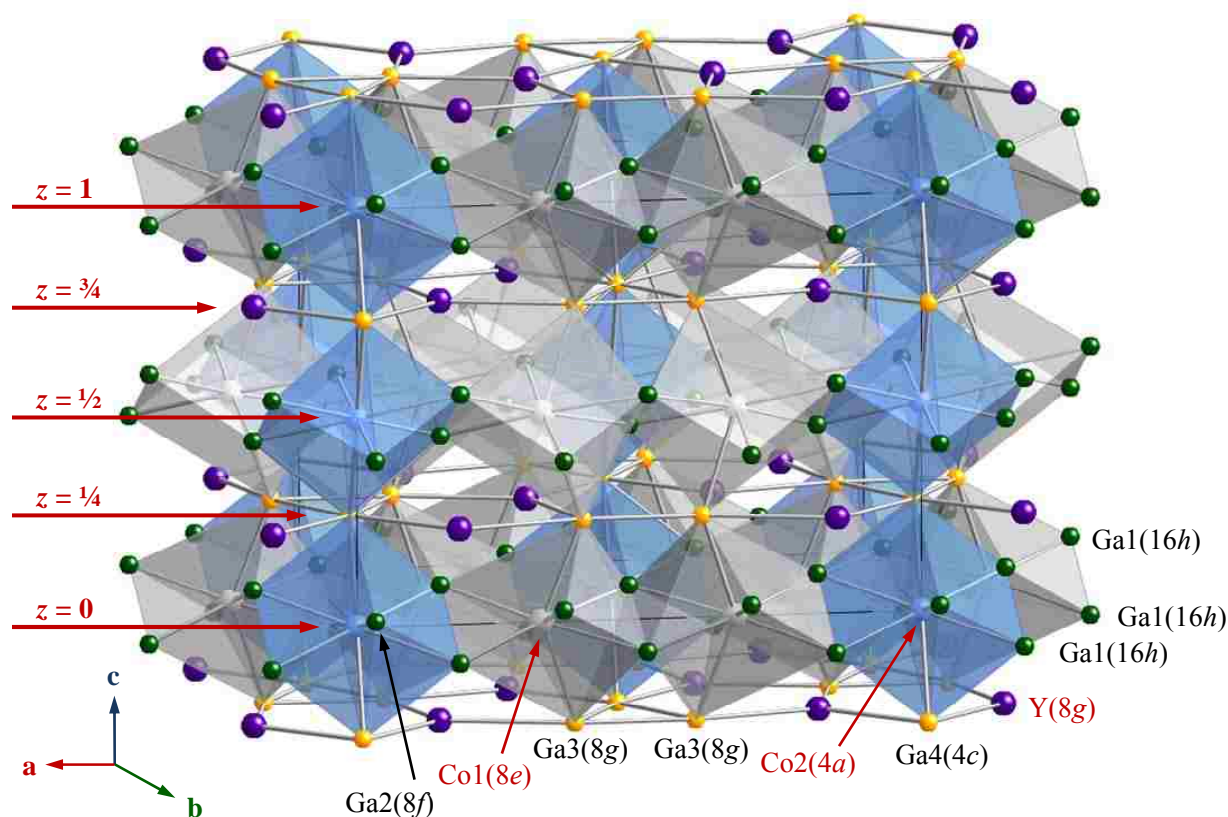
Figure 2.2.   Representation of compounds adopting the $Y_2Co_3Ga_9$ structure-type with selected bonds between slabs omitted for clarity. The fractional *z* coordinates for the slabs built along the crystallographic *c*-axis are labeled.

8
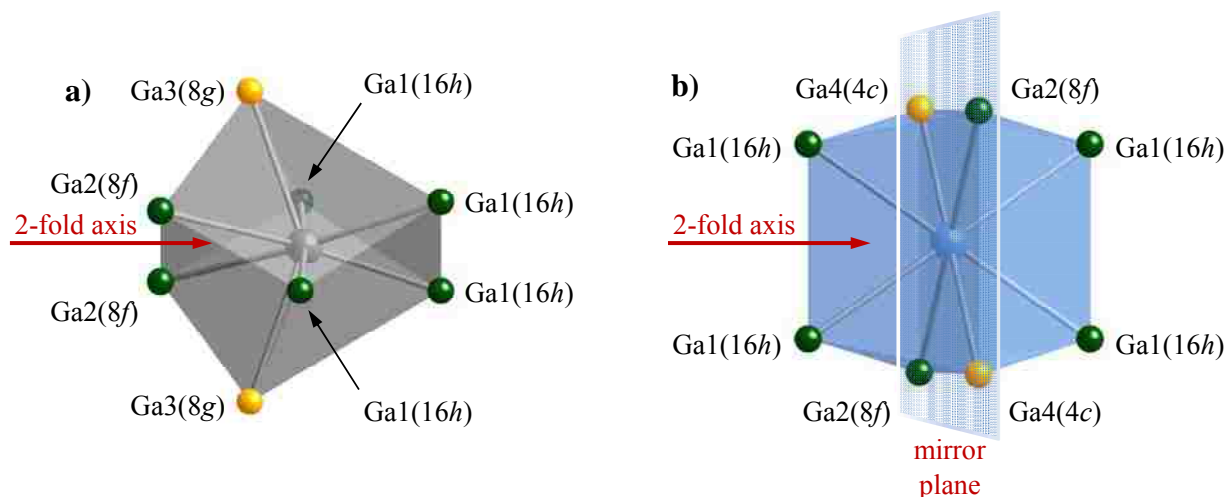
Figure 2.3. Local environments of a) Co1 and b) Co2 polyhedra with C_2 and C_{2h} point group symmetry, respectively, in the $Y_2Co_3Ga_9$ structure-type.
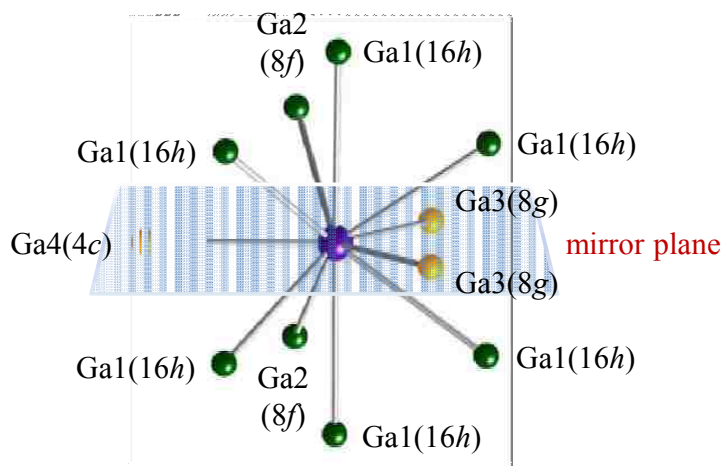
Figure 2.4. Rare earth element, Y, coordination environment with C_s point group symmetry, respectively, in the $Y_2Co_3Ga_9$ structure-type.

earth element coordination environment, respectively. As shown in **Figure 2.5**, "the models for these compounds share the same number of unique and fully occupied [orthorhombic *Cmcm*] Wyckoff atomic sites with one rare earth element site (8*g*), two transition metal sites (4*a* and 8*e*),
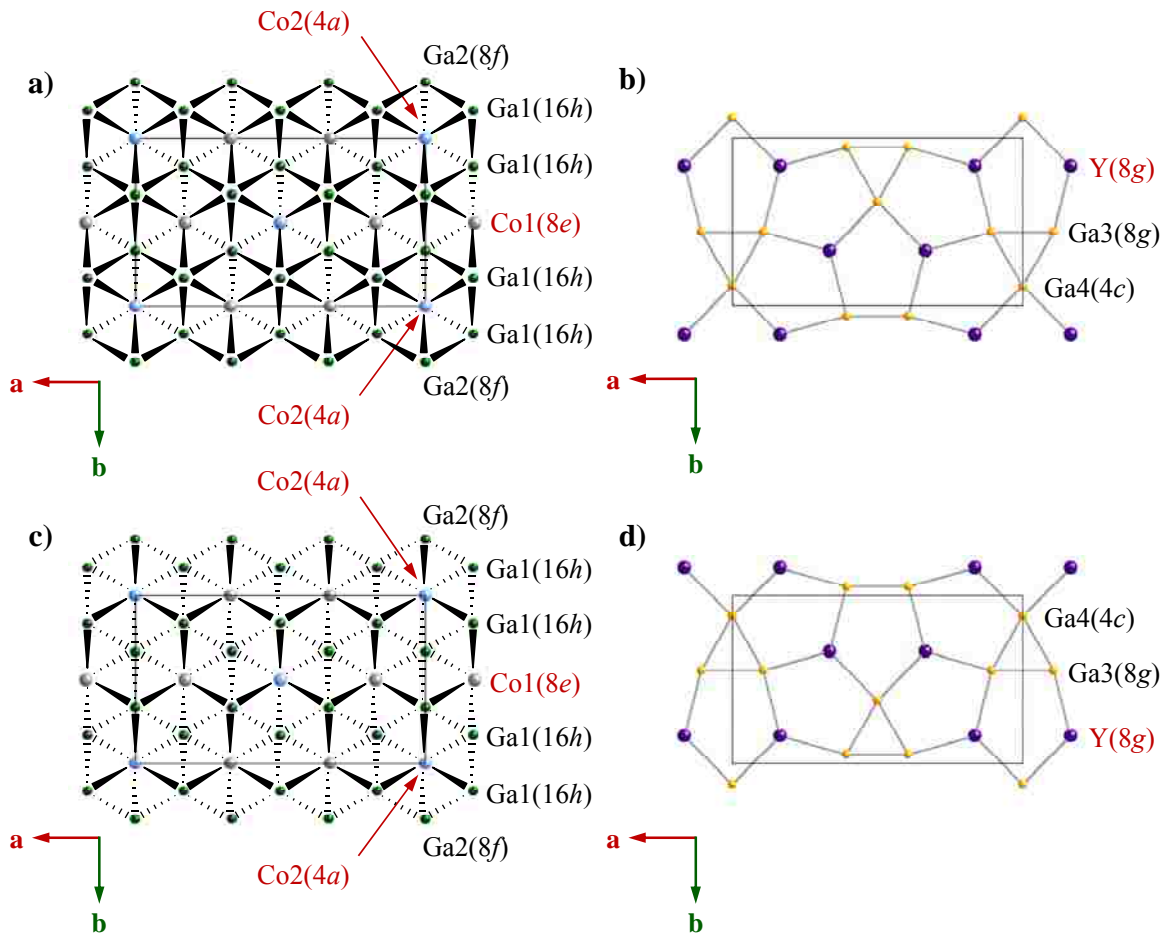
Figure 2.5. Slabs within the $Y_2Co_3Ga_9$ structure-type. Views of the *ab* planes are shown along the crystallographic *c*-axis at a) $z = 0$ or 1, b) $z = \frac{1}{4}$, c) $z = \frac{1}{2}$, and d) $z = \frac{3}{4}$ (see **Figure 2.2** for three dimensional stacking of these slabs). Wyckoff sites are labelled in parentheses following the atomic site name. Solid wedges and dashed wedges are used to depict Ga atoms puckering above and below the *ab* plane, respectively.

and four Group 13 element sites (4*c*, 8*f*, 8*g*, and 16*h*). Unfortunately, the ordered $Y_2Co_3Ga_9$ model could not be adopted as a good fit for the data collected for our single crystals of $Yb_2Pd_3Ga_9$ with a crystal mosaicity of $0.439(3)°$" due to a significant number of atomic sites with lower than expected electron density, additional atomic sites that should not be present in this 2-3-9 structure-type, and several unreasonably short interatomic distances.[15]

Models for the crystal structures of $Ho_2Rh_3Al_9$ and $Er_2Ir_3Al_9$ are structurally related to the ordered $Y_2Co_3Ga_9$ with the inclusion of both partially occupied atomic positions and positional disorder to represent the translationally misplaced slabs.[14] "Along with the Wyckoff atomic sites used for the $Y_2Co_3Ga_9$ structure-type, an additional rare earth element site (4c) and four more Group 13 element sites (each one is 8g) are present" in the Ln_2Al_3 (Ln = Ho, Er) slabs (**Figure 2.6**).[15] "The structures of $Ho_2Rh_3Al_9$ and $Er_2Ir_3Al_9$ are composed of an alternating stack of puckered hexagonally closed packed MAl_2" (M = Rh, Ir) slabs (same as shown previously for $Y_2Co_3Ga_9$ in **Figures 2.5a** and **2.5c**) "alternating with planar Ln_2Al_3 (Ln = Ho, Er) slabs containing a net of distorted pentagons and equilateral triangles along the crystallographic c-axis [(**Figure 2.6**)]. The unique aspect about the structures for $Ho_2Rh_3Al_9$ and $Er_2Ir_3Al_9$ is the occupational and positional disorder of the Ln_2Al_3 layer that occurs when slabs are misplaced (via translation along the crystallographic a-axis by 1/3 or 2/3 of the lattice dimension a [as shown in **Figure 2.7**)] from the 'correct' (or ordered) position based on the $Y_2Co_3Ga_9$ structure-type."[15]

An overlay of the three possible translational arrangements per Ln_2Al_3 slab (**Figure 2.8a** and **2.8b**) reveals how the combination of partially occupied atomic sites (occupation of both Ln atomic sites $\approx$ 66% and all the positions for the Group 13 elements within the disordered slabs $\approx$ 33%) in the average structure allows chemically and structurally unreasonable (due to short interatomic distances) *pseudo* symmetry to appear. It is also observed (**Figure 2.8c**) that the $z = $ ¼ and $z = $ ¾ slabs when combined can mislead the structure determination to a hexagonal space group selection. Furthermore, **Figure 2.8c** looks very similar to an overlay of the six Yb_2Ga_3 slabs in the $P6_122$ model (**Figure 2.9**) for $Yb_2Pd_3Ga_9$. Six slabs are needed (instead of 2 slabs as used for the orthorhombic structure modeled with translational disorder) in order to use this hexagonal space group's 6-fold screw axis symmetry (6_1) to account for the six possible
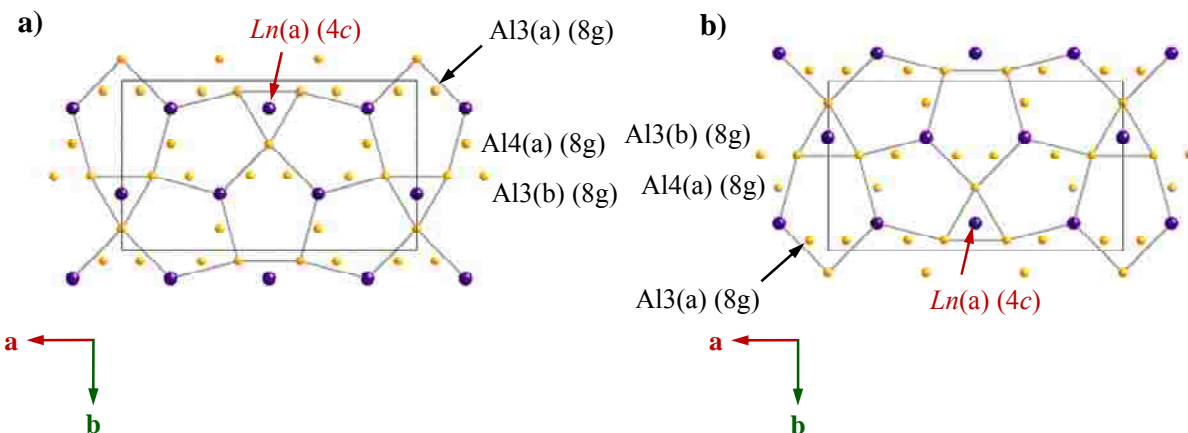
Figure 2.6. Disordered Ln_2Al_3 slabs at a) $z = \frac{1}{4}$ and b) $z = \frac{3}{4}$ with only bonding shown between atoms that occurs in the $Y_2Co_3Ga_9$ structure-type (as shown in **Figures 2.5b** and **2.5d**). The additional atomic sites required for the translational disorder are labeled.
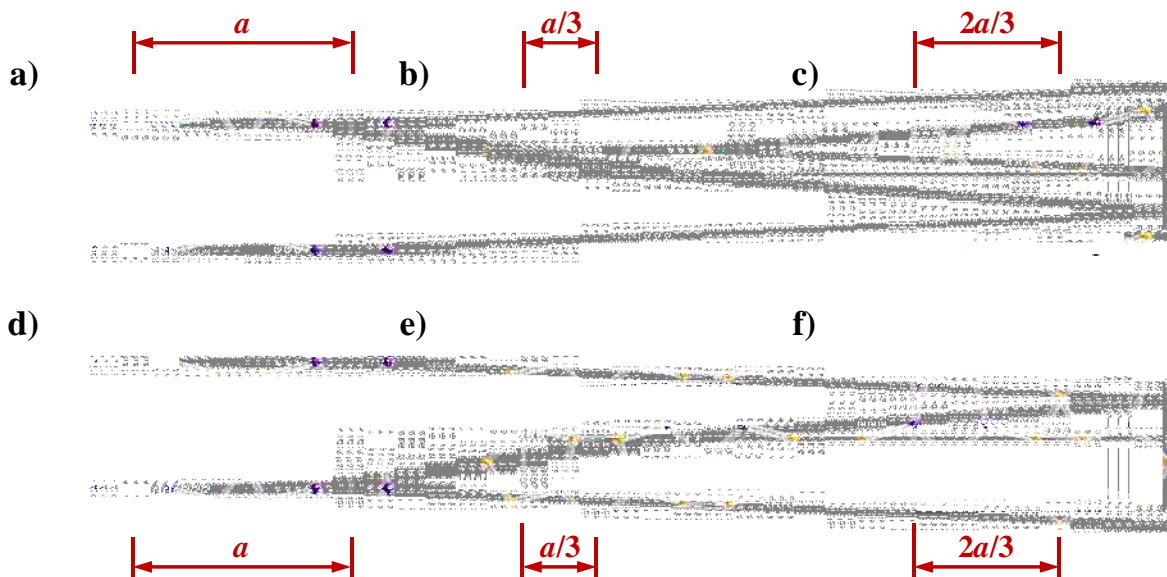
Figure 2.7. Translationally disordered Ln_2Al_3 slabs shown along the crystallographic c-axis at $z = \frac{1}{4}$ (a-c) and $z = \frac{3}{4}$ (d-f). The ordered position (a and d) is translated by 1/3 times the lattice parameter a in (b and e) and 2/3 times the lattice parameter a in (c and f). The result of this translational disorder is a refined occupancy of ~66% and ~33% for Ln and Al atomic sites with the Ln_2Al_3 slabs.
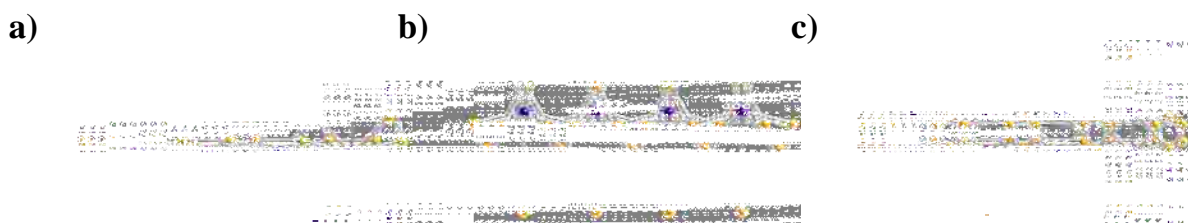
Figure 2.8. Representations of overlay of the three translationally disordered positions of the Ln_2Al_3 slabs shown in Figure 2.7 at a) $z = \frac{1}{4}$ and b) $z = \frac{3}{4}$. These overlays illustrate that the average structure can create *pseudo* 3-fold symmetry. When considering c) both slabs, it can be envisioned how *pseudo* hexagonal elements (such as faux 6-fold screw axes) might be misleading the structure determination.
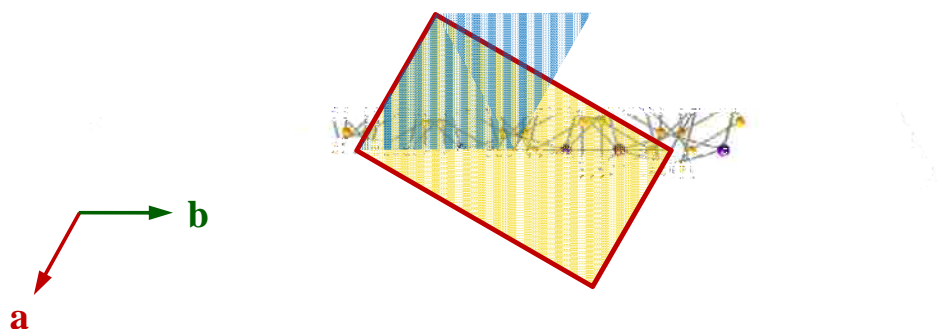
Figure 2.9. Overlay of the six Yb_2Ga_3 slabs in the hexagonal $P6_122$ model. The hexagonal cell is shaded blue while an orthorhombic cell is shaded gold.

arrangements shown in **Figure 2.7**. This explains why both hexagonal models ($P6_122$ and $P6_522$) require a longer lattice parameter c which is three times longer than the c-axis length used for the orthorhombic *Cmcm* unit cell. **Figure 2.10** illustrates the relationship between hexagonal and orthorhombic unit cells and how pseudo symmetry can lead the structure determination away from space group *Cmcm* and toward hexagonal options, such as $P6_122$.

"It is interesting to note that if the orthorhombic unit cell is used to model the diffraction data, the 'E-statistics' calculation $|E^2-1|$ (where E is the normalized structure factor magnitude)
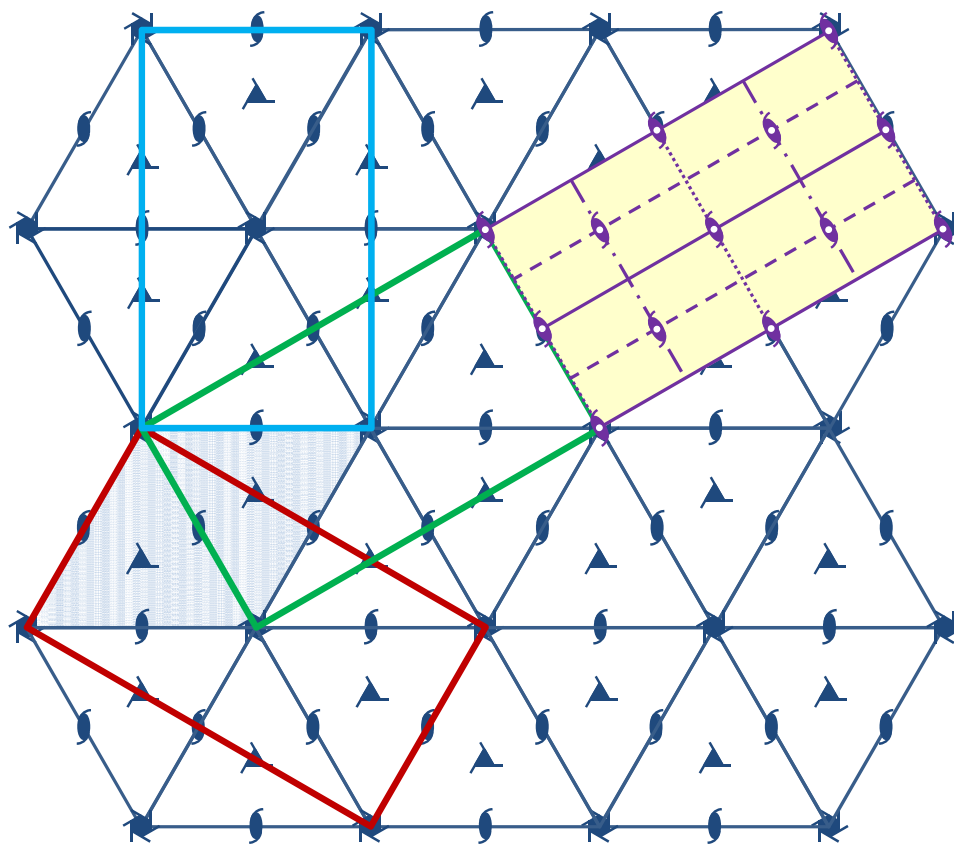
13

Figure 2.10. Relationship between hexagonal (shaded blue) and orthorhombic unit cells (outlined). More detailed information for space groups $P6_122$ and *Cmcm*, such as additional symmetry elements omitted for clarity, can be found in *International Tables for Crystallography* (2006), Vol. A, pp. 300–301, 568-569.

led to a value of 1.532 and implies the structure is centrosymmetric (the standard $|E^2\text{-}1|$ values of centrosymmetric is 0.968 and non-centrosymmetric is 0.736).[20] However, when the hexagonal lattice is used for modeling the data, $|E^2\text{-}1|$ indicates a non-centrosymmetric structure with value of 0.630. Here, the 'E-statistics' are misleading – a point that is noted by Richard Marsh in his paper[21] on space group determination."[15]

"Several models have been evaluated to solve the crystal structure of $Yb_2Pd_3Ga_9$" and the details for the four most suitable models are provided in this section and summarized in **Table 2.1**.[15] Our best attempt to solve the structure in a disordered orthorhombic model was with space group *Cmcm* "with the cell parameters of $a \approx 13.2$ Å, $b \approx 7.6$ Å, $c \approx 9.5$ Å, $V \approx 951$ Å^3, $Z = 4$."[15] Based on the suggested systematic reflection conditions (*hkl*: $h + k = 2n$, *h*00: $h = 2n$, 0*k*0: $k = 2n$, 00*l*: $l = 2n$, *hk*0: $h + k = 2n$, *h*0*l*: $h = 2n$, *h*0*l*: $l = 2n$, *h*0*l*: $h + l = 2n$, 0*kl*: $k = 2n$, *hhl*: $l = 2n$, *h*-*hl*: $l = 2n$), this centrosymmetric space group had the highest figure of merit in the *mmm* Laue class. "Although a model based on the ordered $Y_2Co_3Ga_9$ structure-type did not provide an acceptable fit, the data collected from the $Yb_2Pd_3Ga_9$ single crystal could be modeled in a similar fashion as described[14] for $Ho_2Rh_3Al_9$ and $Er_2Ir_3Al_9$ by Niermann *et al.*"[15]

"Unlike the published structures for $Ho_2Rh_3Al_9$ and $Er_2Ir_3Al_9$, the final refined occupancies of the atomic sites involved in the translational position disordered slabs were left as free variables without any constraints and the atomic positions, displacement parameters, and selected interatomic distances (**Tables 2.2-2.4**). There are two partially occupied Ga sites within the misplaced Yb_2Ga_3 slabs that have been identified as 'non-positive definite' in the list of principal mean square atomic displacements *U*. This is probably caused by both the low partial site occupation (~32%) and the large uncertainties for the anisotropic displacement parameters (i.e., the uncertainty is the same size, or close to the same size, as the calculated displacement). The least squares refinement of the model converged with a R_1 of 0.030, R_{int} of 0.093, $\Delta\rho_{max}$ of

Table 2.1. Crystallographic Parameters of $Yb_2Pd_3Ga_9$ Models (T = 298 K)[15]

Crystal data				
Formula	$Yb_{1.97}Pd_3Ga_9$	$Yb_2Pd_3Ga_9$	$Yb_2Pd_3Ga_9$	$Yb_2Pd_3Ga_9$
MW (g mol^{-1})	1287.14	1292.76	1292.76	1292.76
Crystal system	Orthorhombic	Hexagonal	Hexagonal	Monoclinic
Space group	$Cmcm$ (No. 63)	$P6_122$ (No. 178)	$P6_522$ (No. 179)	$C2/c$ (No. 15)
a (Å)	13.166 (4)	7.608 (3)	7.608 (3)	13.186 (3)
b (Å)	7.605 (2)	7.608 (3)	7.608 (3)	7.5987 (15)
c (Å)	9.496 (3)	28.508 (15)	28.508 (15)	10.476 (2)
β (°)	90	90	90	114.900 (9)
V (Å^3)	950.8 (4)	1428.9 (11)	1428.9 (11)	952.0 (3)
Z	4	6	6	4
$F(000)$	2219	3342	3342	2228
d (g cm^{-3})	8.992	9.014	9.014	9.019
μ (mm^{-1})	49.61	49.84	49.84	49.86
Data collection				
Total reflections	4499	13976	13976	4537
Unique reflections	776	1427	1427	1410
Reflections $I>2\sigma(I)$	271	654	654	1154
[a]R_{int}	0.093	0.371	0.371	0.081
θ_{max}(°),θ_{min}(°)	30.2, 3.1	30.3, 3.1	30.3, 3.1	30.2, 3.2
h	-18→18	-10→10	-10→10	-18→18
k	-10→10	-10→10	-10→10	-10→10
l	-13→13	-39→40	-39→40	-14→14
Refinement				
Reflections	776	1427	1427	1410
Parameters	71	67	67	67
Restraints	0	0	0	0
[b]$R_1[F^2>2\sigma(F^2)]$	0.030	0.074	0.073	0.053
[c]$wR_2(F^2)$	0.098	0.149	0.144	0.197
[d]S	0.89	1.02	1.00	1.35
$\Delta\rho_{max}$ (eÅ^{-3})	2.53	3.54	3.84	14.79
$\Delta\rho_{min}$ (eÅ^{-3})	-2.98	-5.97	-6.22	-4.33
Extinction coefficient	0.00136 (9)	0.00064 (4)	0.00066 (4)	0.00116 (17)
Flack x parameter	n/a	0.3 (3)	0.6 (3)	n/a
Hooft y parameter	n/a	0.5 (3)	0.6 (3)	n/a

[a]$R_{int} = \Sigma \mid F_o{}^2 - F_o{}^2 \text{ (mean)} \mid / \Sigma [F_o{}^2]$

[b]$R_1 = \Sigma \mid\mid F_o \mid - \mid F_c \mid\mid / \Sigma \mid F_o \mid$

[c]$wR_2 = [\Sigma [w(F_o{}^2 - F_c{}^2)^2] / \Sigma [w(F_o{}^2)^2]]^{1/2}$ where $w = 1 / [\sigma^2(F_o{}^2) + (0.0419P)^2]$ for $Cmcm$ model, $w = 1 / [\sigma^2(F_o{}^2) + (0.0280P)^2]$ for $P6_122$ model, $w = 1 / [\sigma^2(F_o{}^2) + (0.0274P)^2]$ for $P6_522$ model, and $w = 1 / [\sigma^2(F_o{}^2) + (0.1000P)^2]$ for $C2/c$ model

[d]$S = [\Sigma [w(F_o{}^2 - F_c{}^2)^2] / (n - p)]^{1/2}$

Table 2.2. Atomic Positions and Equivalent Isotropic Displacement Parameters for Orthorhombic *Cmcm* Model[15]

Atom	Wyckoff site	x	y	z	Occ.[a]	U_{eq} (Å²)[b]
Yb	8g	0.33315(10)	0.33323(10)	1/4	0.667 (2)	0.0080 (3)
Pd1	8e	0.33299(9)	0	0	1	0.0082 (3)
Pd2	4a	0	0	0	1	0.0074 (5)
Ga1	16h	0.16665(9)	0.16653(10)	0.07629(12)	1	0.0100 (3)
Ga2	8f	0	0.33409(17)	0.5761(2)	1	0.0096 (5)
Ga3	8g	0.1048(4)	0.4357(6)	1/4	0.391 (4)	0.0165 (19)
Ga4	4c	0	0.1254(8)	1/4	0.346 (7)	0.014 (3)
Yb(a)	4c	0	0.33335(18)	1/4	0.641 (3)	0.0067 (6)
Ga3(a)	8g	0.4375(4)	0.4376(6)	1/4	0.305 (4)	0.0069 (18)
Ga3(b)	8g	0.2293(4)	0.4330(7)	1/4	0.322 (5)	0.010 (2)
Ga4(a)	8g	0.3326(4)	0.1257(5)	1/4	0.310 (4)	0.0052 (15)

[a] Occupancy
[b] U_{eq} is defined as one-third of the trace of the orthogonalized U^{ij} tensor.

Table 2.3. Anisotropic Atomic Displacement Parameters (Å²) for Orthorhombic *Cmcm* Model[15]

Atom	U^{11}	U^{22}	U^{33}	U^{12}	U^{13}	U^{23}
Yb	0.0061 (6)	0.0093 (6)	0.0085 (6)	0.0017 (7)	0.000	0.000
Pd1	0.0048 (6)	0.0098 (5)	0.0099 (7)	0.000	0.000	0.0009 (4)
Pd2	0.0061 (9)	0.0102 (9)	0.0058 (11)	0.000	0.000	−0.0016 (8)
Ga1	0.0037 (6)	0.0091 (6)	0.0172 (8)	0.0003 (6)	0.0010 (8)	0.0004 (5)
Ga2	0.0071 (11)	0.0103 (9)	0.0112 (12)	0.000	0.000	0.0001 (9)
Ga3	0.015 (4)	0.014 (3)	0.021 (4)	0.003 (3)	0.000	0.000
Ga4	0.015 (6)	0.012 (5)	0.016 (6)	0.000	0.000	0.000
Yb(a)	0.0029 (10)	0.0097 (11)	0.0076 (10)	0.000	0.000	0.000
Ga3(a)	0.008 (4)	0.007 (3)	0.005 (4)	−0.003 (3)	0.000	0.000
Ga3(b)	0.002 (4)	0.015 (4)	0.012 (4)	−0.005 (3)	0.000	0.000
Ga4(a)	0.001 (3)	0.009 (3)	0.005 (3)	−0.010 (3)	0.000	0.000

2.53 e Å⁻³, and $\Delta\rho_{min}$ of -2.98 e Å⁻³. In addition, the goodness of fit parameter, S, is 0.89 after applying a weighting scheme of $w = 1/[\sigma^2(F_o^2) + (0.0419P)^2]$ where $P = (F_o^2 + 2F_c^2)/3$."[15]

Table 2.4. Selected Interatomic Distances (Å) for Orthorhombic *Cmcm* Model[15]

Yb-Ga1 (x2)	3.0221 (15)	Pd1-Ga1 (x2)	2.6316 (16)
Yb-Ga1 (x2)	3.0243 (13)	Pd1-Ga1 (x2)	2.6375 (10)
Yb-Ga1 (x2)	3.0986 (14)	Pd1-Ga2 (x2)	2.6361 (14)
Yb-Ga2 (x2)	3.0285 (17)	Pd1-Ga3 (x2)	2.558 (2)
Yb-Ga3	3.105 (5)	Pd1-Ga3(b) (x2)	2.563 (2)
Yb-Ga3	3.132 (5)	Pd1-Ga4(a) (x2)	2.5593(15)
Yb-Ga4	3.125 (5)		
Yb-Ga3(a)	3.122 (6)		
Yb-Ga3(b)	3.153 (5)		
Yb-Ga4(a)	3.116 (5)		
Yb(a)-Ga1 (x4)	3.0240 (14)	Pd2-Ga1 (x4)	2.6349 (12)
Yb(a)-Ga2 (x2)	3.021 (2)	Pd2-Ga2 (x2)	2.6416 (15)
Yb(a)-Ga2 (x2)	3.097 (2)	Pd2-Ga4 (x2)	2.558 (2)
Yb(a)-Ga3(a) (x2)	3.120 (5)	Pd2-Ga3(a) (x2)	2.5571 (19)
Yb(a)-Ga3(b) (x2)	3.112 (5)		
Yb(a)-Ga4(a) (x2)	3.131 (5)		
Yb-Pd1 (x2)	3.4683 (13)	Ga3-Ga3	2.760 (10)
Yb-Pd1 (x2)	3.4725 (9)	Ga3-Ga4	2.734 (7)
Yb-Pd2 (x2)	3.4742 (11)	Ga3(a)-Ga3(b)	2.741 (7)
Yb(a)-Pd1 (x4)	3.4752 (11)	Ga3(a)-Ga4(a)	2.744 (7)
Yb(a)-Pd2 (x2)	3.4731 (12)	Ga3(b)-Ga4(a)	2.704 (8)

"A hexagonal unit cell ($a \approx 7.6$ Å, $b \approx 7.6$ Å, $c \approx 28.5$ Å, $V \approx 1429$ Å^3) has also been identified for this compound and is related to the orthorhombic unit cell by the following relationships: $a_o = \sqrt{3}\, a_h$, $b_o = b_h$, $c_o = 1/3\, c_h$, and $V_o = 2/3\, V_h$ (where o = orthorhombic and h = hexagonal). This same hexagonal unit cell was used in the graduate work of Giedigkeit *et al.*,[12,13] which has been cited in the literature,[7,11] and it was suggested that $Yb_2Pd_3Ga_9$ is a "new structure-type" in hexagonal space group $P6_122$ (No. 178). This structure is built along the crystallographic *c*-axis of puckered hexagonally closed packed $PdGa_2$ slabs alternating with planar Yb_2Ga_3 slabs containing a triangular arrangement of Ga atoms within a hexagonal net of Yb atoms. Based on the suggested systematic reflection conditions (00*l*: *l* = 2*n*, 00*l*: *l* = 3*n*, 00*l*:

18

$l = 6n$), there are two space group options in the $6/m$ Laue class ($P6_1$, No. 169, and $P6_5$, No. 170) and two space group options in the $6/mmm$ Laue class ($P6_122$, No. 178, and $P6_522$, No. 179) with the highest figure of merits. Models in $6/m$ Laue class would lead to the recognition of missing multiple two-fold symmetry, which is included in the recommended $6/mmm$ Laue class options. The best $P6_122$ model has the atomic coordinates (which are similar to Giedigkeit's model)", displacement parameters, and selected interatomic distances shown in **Tables 2.5-2.7**.[15]

Table 2.5. Atomic Positions and Equivalent Isotropic Displacement Parameters for Hexagonal $P6_122$ Model[15]

Atom	Wyckoff site	x	y	z	Occ.[a]	U_{eq} (Å^2)[b]
Yb	12c	0.9992 (2)	0.66755 (19)	0.00016 (4)	1	0.0084 (2)
Pd1	6b	0.0040 (5)	0.0020 (2)	1/12	1	0.0076 (6)
Pd2	6b	0.3304 (5)	0.6652 (3)	1/12	1	0.0087 (8)
Pd3	6b	0.6655 (5)	0.3327 (3)	1/12	1	0.0074 (7)
Ga1	6a	0.8718 (5)	0	0	1	0.0110 (10)
Ga2	12c	0.4570 (4)	0.7903 (4)	0.00047 (14)	1	0.0099 (6)
Ga3	12c	0.3295 (5)	0.9983 (5)	0.05692 (8)	1	0.0095 (5)
Ga4	12c	0.0038 (5)	0.3369 (5)	0.05674 (9)	1	0.0086 (5)
Ga5	12c	0.6661 (4)	0.6650 (5)	0.06026 (10)	1	0.0095 (5)

[a] Occupancy
[b] U_{eq} is defined as one-third of the trace of the orthogonalized U^{ij} tensor.

Table 2.6. Anisotropic Atomic Displacement Parameters (Å^2) for Hexagonal $P6_122$ Model[15]

Atom	U^{11}	U^{22}	U^{33}	U^{12}	U^{13}	U^{23}
Yb	0.0081 (6)	0.0092 (6)	0.0086 (4)	0.0048 (5)	0.0002 (7)	0.0005 (6)
Pd1	0.0079 (15)	0.0084 (10)	0.0062 (16)	0.0039 (7)	0.000	0.0009 (11)
Pd2	0.0090 (16)	0.0083 (11)	0.009 (2)	0.0045 (8)	0.000	−0.0004 (12)
Pd3	0.0056 (15)	0.0065 (11)	0.010 (2)	0.0028 (8)	0.000	−0.0010 (12)
Ga1	0.0139 (18)	0.012 (2)	0.006 (2)	0.0062 (11)	−0.0017 (12)	−0.003 (2)
Ga2	0.0085 (14)	0.0094 (17)	0.0122 (14)	0.0048 (11)	−0.0017 (16)	0.0012 (16)
Ga3	0.0062 (15)	0.0096 (16)	0.0103 (12)	0.0022 (14)	0.0018 (15)	0.0025 (17)
Ga4	0.0063 (15)	0.0071 (15)	0.0114 (12)	0.0026 (15)	−0.0016 (17)	−0.0021 (16)
Ga5	0.0081 (16)	0.0051 (15)	0.0168 (11)	0.0044 (14)	−0.0008 (17)	−0.0003 (16)

Table 2.7.   Selected Interatomic Distances (Å) for Hexagonal $P6_122$ Model[15]

Yb-Ga1	3.129 (4)	Pd1-Ga1 (x2)	2.577 (2)
Yb-Ga2	3.118 (3)	Pd1-Ga3 (x2)	2.602 (4)
Yb-Ga2	3.122 (3)	Pd1-Ga4 (x2)	2.659 (3)
Yb-Ga3	2.990 (3)	Pd1-Ga5 (x2)	2.650 (4)
Yb-Ga3	3.011 (3)		
Yb-Ga3	3.133 (3)	Pd2-Ga2 (x4)	2.549 (4)
Yb-Ga4	2.990 (3)	Pd2-Ga3 (x2)	2.647 (3)
Yb-Ga4	3.003 (3)	Pd2-Ga4 (x2)	2.604 (4)
Yb-Ga4	3.129 (3)	Pd2-Ga5 (x2)	2.639 (4)
Yb-Ga5	3.051 (3)		
Yb-Ga5	3.067 (3)	Pd3-Ga2 (x4)	2.568 (4)
Yb-Pd1	3.455 (3)	Pd3-Ga3 (x2)	2.659 (4)
Yb-Pd1	3.4648 (16)	Pd3-Ga4 (x2)	2.668 (4)
Yb-Pd2	3.466 (3)	Pd3-Ga5 (x2)	2.609 (3)
Yb-Pd2	3.4785 (16)		
Yb-Pd3	3.477 (3)		
Yb-Pd3	3.480 (3)		

"The least squares refinement of the $P6_122$ model converged with a R_1 of 0.074, $\Delta\rho_{max}$ of 3.54 e Å^{-3}, and $\Delta\rho_{min}$ of -5.97 e Å^{-3}."[15]   These parameters are less desirable than the translationally disordered orthorhombic *Cmcm* model and indicate a poorer fit of the hexagonal $P6_122$ model to the data.   Also, "the Flack x parameter[22] is 0.3(3) and the Hooft y parameter[23] is 0.5(3) for this model.   These parameters, which have large respective uncertainties, do not provide conclusive evidence that a single enantiomer is present for this non-centrosymmetric model. R_{int} of 0.371 is a strong indicator of wrong crystal system, Laue class, or space group. This high R_{int} value cannot be attributed to poor crystal diffraction data because the crystal did not scatter weakly, the images contain well-defined single diffraction peaks with no evidence of twinning and there was sufficient data collected (triclinic data collection with a redundancy of 2). The goodness of fit is 1.02 after applying a weighting scheme of $w = 1/[\sigma^2(F_o^2) + (0.028P)^2]$."[15]

"$P6_522$ (with left-handed screw axes), the enantiomeric space group of $P6_122$ (with right-handed screw axes), was also evaluated and the atomic positions", displacement parameters, and selected interatomic distances are provided in **Table 2.8-2.10**.[15] "The least squares refinement of this model converged with a R_1 of 0.073, $\Delta\rho_{max}$ of 3.84 e Å^{-3}, and $\Delta\rho_{min}$ of −6.22 e Å^{-3}(which are all similar to the results from the $P6_122$ model). For this model, evidence of a single enantiomer is also absent with a Flack x parameter is 0.6(3) and a Hooft y parameter of 0.6(3). The R_{int}

Table 2.8. Atomic Positions and Equivalent Isotropic Displacement Parameters for Hexagonal $P6_522$ Model[15]

Atom	Wyckoff site	x	y	z	Occ.[a]	U_{eq} (Å^2)[b]
Yb	12c	0.66553 (16)	0.66496 (17)	0.00016 (4)	1	0.0085 (2)
Pd1	6b	0.9981 (3)	0.0019 (3)	1/12	1	0.0083 (6)
Pd2	6b	0.3352 (3)	0.6648 (3)	1/12	1	0.0084 (8)
Pd3	6b	0.6672 (2)	0.3328 (2)	1/12	1	0.0072 (8)
Ga1	6a	0.1214 (4)	0	0	1	0.0100 (10)
Ga2	12c	0.3319 (4)	0.7932 (4)	0.00043 (14)	1	0.0106 (6)
Ga3	12c	0.6682 (5)	0.9982 (5)	0.05692 (8)	1	0.0093 (5)
Ga4	12c	0.3334 (4)	0.3367 (5)	0.05677 (9)	1	0.0088 (5)
Ga5	12c	0.9990 (5)	0.6649 (5)	0.06027 (10)	1	0.0097 (5)

[a] Occupancy
[b] U_{eq} is defined as one-third of the trace of the orthogonalized U^{ij} tensor.

Table 2.9. Anisotropic Atomic Displacement Parameters (Å^2) for Hexagonal $P6_522$ Model[15]

Atom	U^{11}	U^{22}	U^{33}	U^{12}	U^{13}	U^{23}
Yb	0.0065 (6)	0.0094 (6)	0.0087 (3)	0.0034 (5)	0.0002 (5)	−0.0002 (7)
Pd1	0.0078 (9)	0.0078 (9)	0.0100 (17)	0.0042 (12)	0.0019 (12)	0.0019 (12)
Pd2	0.0086 (12)	0.0086 (12)	0.008 (2)	0.0045 (13)	−0.0007 (12)	−0.0007 (12)
Pd3	0.0077 (11)	0.0077 (11)	0.0072 (19)	0.0047 (13)	−0.0015 (12)	−0.0015 (12)
Ga1	0.0098 (16)	0.012 (2)	0.009 (2)	0.0061 (10)	0.0026 (12)	0.005 (2)
Ga2	0.0089 (11)	0.0128 (16)	0.0110 (13)	0.0063 (13)	−0.0037 (17)	−0.0026 (16)
Ga3	0.0095 (16)	0.0097 (16)	0.0096 (11)	0.0054 (15)	0.0012 (17)	0.000 (2)
Ga4	0.0055 (15)	0.0074 (16)	0.0119 (12)	0.0021 (13)	0.0013 (17)	−0.0012 (16)
Ga5	0.0047 (14)	0.0059 (16)	0.0173 (11)	0.0018 (14)	0.001 (2)	0.0001 (17)

Table 2.10. Selected Interatomic Distances (Å) for Hexagonal $P6_522$ Model[15]

Yb-Ga1	3.112 (3)	Pd1-Ga1 (x2)	2.557 (2)
Yb-Ga2	3.117 (3)	Pd1-Ga3 (x2)	2.607 (4)
Yb-Ga2	3.142 (3)	Pd1-Ga4 (x2)	2.659 (3)
Yb-Ga3	2.999 (3)	Pd1-Ga5 (x2)	2.649 (4)
Yb-Ga3	3.021 (3)		
Yb-Ga3	3.133 (3)	Pd2-Ga2 (x4)	2.562 (4)
Yb-Ga4	2.986 (3)	Pd2-Ga3 (x2)	2.644 (3)
Yb-Ga4	3.002 (3)	Pd2-Ga4 (x2)	2.602 (4)
Yb-Ga4	3.128 (3)	Pd2-Ga5 (x2)	2.641 (4)
Yb-Ga5	3.049 (3)		
Yb-Ga5	3.062 (3)	Pd3-Ga2 (x4)	2.577 (4)
Yb-Pd1	3.470 (3)	Pd3-Ga3 (x2)	2.658 (4)
Yb-Pd1	3.4798 (15)	Pd3-Ga4 (x2)	2.664 (4)
Yb-Pd2	3.455 (3)	Pd3-Ga5 (x2)	2.610 (3)
Yb-Pd2	3.4718 (16)		
Yb-Pd3	3.470 (3)		
Yb-Pd3	3.472 (3)		

value is 0.371 (just as high as the $P6_122$ model) and the goodness of fit is 1.00 after applying a weighting scheme of $w = 1/[\sigma^2(F_o^2) + (0.0274P)^2]$."[15]

"A monoclinic $C2/c$ (No. 15) model used previously to solve the crystal structure of 2-9-3 phase of three ternary germanides ($Tb_2Pt_9Ge_3$, $Dy_2Pt_9Ge_3$, and $Ho_2Pt_9Ge_3$),[11] was also evaluated even though the stoichiometry differs from the 2-3-9 phase. Based on the suggested systematic reflection conditions (hkl: $h + k = 2n$, $h00$: $h = 2n$, $0k0$: $k = 2n$, $00l$: $l = 2n$, $hk0$: $h + k = 2n$, $h0l$: $h = 2n$, $h0l$: $l = 2n$, $h0l$: $h + l = 2n$, $0kl$: $k = 2n$, h-hl: $l = 2n$), both $C2/c$ and Cc (Space Group No. 9) had the high figures of merit within the $2/m$ Laue class. Modeling the data in the non-centrosymmetric space group Cc would lead to the observation of a missing inversion center. Our best $C2/c$ model using a monoclinic unit cell ($a \approx 13.2$ Å, $b \approx 7.6$ Å, $c \approx 10.5$ Å, $\beta \approx 114.9$ °, and $V = 952$ Å^3) has the atomic coordinates", displacement parameters, and selected interatomic distances provided in **Tables 2.11-2.13**.[15] "The least squares refinement [of the data

collected] converged with a R_1 of 0.053, $\Delta\rho_{max}$ of 14.79 e Å^{-3}, and $\Delta\rho_{min}$ of -4.33 e Å^{-3}. The R_{int}

value is 0.081 (similar to the *Cmcm* model) and the goodness of fit is 1.35. The weighting

scheme was not adjusted from the default starting value of $w = 1/[\sigma^2(F_o^2) + (0.1P)^2]$ because the

model still contained a significant unaccounted for electron density of 14.79 e Å^{-3} located 1.57 Å

from two equivalent gallium atoms (Ga3) and 1.61 Å from a third gallium atom (Ga5). Attempts

to resolve this residual electron density with translational disorder did not achieve better results

(i.e., significantly poorer fitting model to data and still left with unresolved electron density)."[15]

Table 2.11. Atomic Positions and Equivalent Isotropic Displacement Parameters for Monoclinic *C2/c* Model[15]

Atom	Wyckoff site	x	y	z	Occ.[a]	U_{eq} (Å^2)[b]
Yb	8*f*	0.16753 (5)	0.41646 (9)	0.25043 (6)	1	0.0088 (3)
Pd1	8*f*	0.08408 (9)	0.25316 (13)	0.49996 (11)	1	0.0076 (4)
Pd2	4*c*	1/4	1/4	0	1	0.0079 (4)
Ga1	8*f*	0.10752 (15)	0.0853 (2)	0.0691 (2)	1	0.0101 (4)
Ga2	8*f*	0.22449 (14)	0.0849 (2)	0.42038 (19)	1	0.0089 (5)
Ga3	8*f*	0.39591 (14)	0.3145 (2)	0.25102 (18)	1	0.0103 (4)
Ga4	8*f*	0.44285 (14)	0.0812 (2)	0.07935 (18)	1	0.0092 (5)
Ga5	4*e*	0	0.1249 (3)	1/4	1	0.0109 (5)

[a] Occupancy
[b] U_{eq} is defined as one-third of the trace of the orthogonalized U^{ij} tensor.

Table 2.12. Anisotropic Atomic Displacement Parameters (Å^2) for Monoclinic *C2/c* Model[15]

Atom	U^{11}	U^{22}	U^{33}	U^{12}	U^{13}	U^{23}
Yb	0.0046 (4)	0.0107 (4)	0.0092 (4)	−0.0007 (2)	0.0012 (3)	0.0000 (2)
Pd1	0.0044 (7)	0.0096 (6)	0.0081 (7)	−0.0005 (4)	0.0017 (5)	−0.0003 (4)
Pd2	0.0031 (8)	0.0097 (8)	0.0089 (8)	−0.0005 (6)	0.0005 (7)	−0.0002 (5)
Ga1	0.0056 (10)	0.0093 (9)	0.0163 (9)	0.0001 (6)	0.0055 (8)	0.0006 (6)
Ga2	0.0043 (9)	0.0094 (9)	0.0120 (9)	0.0004 (6)	0.0024 (8)	−0.0002 (6)
Ga3	0.0065 (9)	0.0132 (9)	0.0093 (8)	−0.0003 (6)	0.0013 (7)	−0.0009 (6)
Ga4	0.0051 (10)	0.0107 (9)	0.0113 (9)	−0.0003 (6)	0.0031 (8)	−0.0004 (6)
Ga5	0.0062 (12)	0.0151 (11)	0.0092 (11)	0.000	0.0010 (9)	0.000

Table 2.13.   Selected Interatomic Distances (Å) for Monoclinic $C2/c$ Model[15]

Yb-Ga1	3.049 (2)	Pd1-Ga1	2.645 (2)
Yb-Ga1	3.050 (2)	Pd1-Ga1	2.654 (2)
Yb-Ga2	2.9928 (19)	Pd1-Ga2	2.609 (2)
Yb-Ga2	3.0021 (18)	Pd1-Ga2	2.6547 (17)
Yb-Ga2	3.128 (2)	Pd1-Ga3	2.561 (2)
Yb-Ga3	3.1070 (19)	Pd1-Ga4	2.604 (5)
Yb-Ga3	3.1364 (18)	Pd1-Ga4	2.655 (2)
Yb-Ga4	3.0083 (18)	Pd1-Ga5	2.5674 (15)
Yb-Ga4	3.0139 (19)		
Yb-Ga4	3.1336 (19)	Pd2-Ga1 (x2)	2.6009 (17)
Yb-Ga5	3.1273 (19)	Pd2-Ga2 (x2)	2.6546 (17)
		Pd2-Ga3 (x2)	2.5684 (18)
Yb-Pd1 (x2)	3.4593 (13)	Pd2-Ga4 (x2)	2.6502 (17)
Yb-Pd1	3.4662 (14)		
Yb-Pd1	3.4783 (14)		
Yb-Pd2	3.4710 (8)		
Yb-Pd2	3.4738 (8)		

"Unpublished results by Bobev *et al.* suggests that $Yb_2M_3Ga_9$ (M = Rh, Ir) crystallizes in hexagonal $P6_3cm$ (No. 185).[24] No suitable models have been developed using this space group. This space group was also tried unsuccessfully by Niermann *et al.*[14] in their single crystal refinement of $Ho_2Rh_3Al_9$ and $Er_2Ir_3Al_9$."[15]

2.4   Conclusions

"Of the four suggested models [using orthorhombic, hexagonal, and monoclinic unit cells for the crystal structure of $Yb_2Pd_3Ga_9$], the orthorhombic *Cmcm* model with [translational] disorder appears to be the best fit of the data. Niermann *et al.* stated for $Ho_2Rh_3Al_9$ and $Er_2Ir_3Al_9$ compounds 'that both structure determinations and refinements were not straightforward'[14] and this is also true for solving the structure of $Yb_2Pd_3Ga_9$."[15]

2.5 References

(1) Buschinger, B.; Geibel, C.; Weiden, M.; Dietrich, C.; Cordier, G.; Olesch, G.; Kohler, J.; Steglich, F. *J. Alloy Compd.* **1997**, *260*, 44-49.

(2) Gladyshevskii, R. E.; Cenzual, K.; Parthe, E. *Z. Kristall.* **1993**, *203*, 113-114.

(3) Tougait, O.; Noel, H. *J. Alloy Compd.* **2006**, *417*, 1-6.

(4) Troc, R.; Tougait, O.; Noel, H. *Intermetallics* **2007**, *15*, 1091-1095.

(5) Grin, Y. N.; Rogl, P. *Izv. Akad. Nauk SSSR, Neorg. Mater.* **1989**, *25*, 593-596.

(6) Grin, Y. N.; Rogl, P. *Inorg. Mater.* **1989**, *25*, 514-517.

(7) Sichevych, O.; Schnelle, W.; Prots, Y.; Burkhardt, U.; Grin, Y. *Z. Naturforsch. B* **2006**, *61*, 904-911.

(8) Schluter, M.; Jeitschko, W. *Z. Anorg. Allg. Chem.* **2000**, *626*, 2217-2222.

(9) Dung, N. D.; Matsuda, T. D.; Haga, Y.; Ikeda, S.; Yamamoto, E.; Endo, T.; Settai, R.; Harima, H.; Onuki, Y. *J. Phys. Soc. Jpn.* **2008**, *77*, 064708.

(10) Grin, Y. N.; Gladyshevskii, R. E.; Sichevich, O. M.; Zavodnik, V. E.; Yarmolyuk, Y. P.; Rozhdestvenskaya, I. V. *Kristallografiya* **1984**, *29*, 893-898.

(11) Prots, Y.; Borrmann, H.; Schnelle, W.; Jeitschko, W. *Z. Anorg. Allg. Chem.* **2005**, *631*, 1218-1226.

(12) Giedigkeit, R. Dissertation, Technischen Universität Dresden, 2007.

(13) Giedigkeit, R.; Schnelle, W.; Grin, Y.; Kniep, R. In *Collected Abstracts of VIIth European Conference on Solid State Chemistry* Madrid, 1999, p P136.

(14) Niermann, J.; Fehrmann, B.; Wolff, M. W.; Jeitschko, W. *J. Solid State Chem.* **2004**, *177*, 2600-2609.

(15) Phelan, W. A.; Menard, M. C.; Kangas, M. J.; McCandless, G. T.; Drake, B. L.; Chan, J. Y. *Chem. Mater.* **2012**, *24*, 409-420.

(16) Otwinowski, Z.; Minor, W. In *Methods in Enzymology*; Carter Jr., C. W., Sweet, R. M., Eds.; Academic Press Inc.: New York, 1997; Vol. 276, Macromolecular Crystallography, Part A, p 307-326.

(17)   Altomare, A.; Burla, M. C.; Camalli, M.; Cascarano, G. L.; Giacovazzo, C.; Guagliardi, A.; Moliterni, A. G. G.; Polidori, G.; Spagna, R. *J. Appl. Crystallogr.* **1999**, *32*, 115-119.

(18)   Sheldrick, G. M. *Acta Crystallogr. Sect. A* **2008**, *64*, 112-122.

(19)   Spek, A. L. *J. Appl. Crystallogr.* **2003**, *36*, 7-13.

(20)   Karle, I. L.; Dragonette, K. S.; Brenner, S. A. *Acta Crystallogr.* **1965**, *19*, 713-716.

(21)   Marsh, R. E. *Acta Crystallogr. Sect. B-Struct. Commun.* **1995**, *51*, 897-907.

(22)   Flack, H. D. *Acta Crystallogr. Sect. A* **1983**, *39*, 876-881.

(23)   Hooft, R. W. W.; Straver, L. H.; Spek, A. L. *J. Appl. Crystallogr.* **2008**, *41*, 96-103.

(24)   Christianson, A. D.; Lawrence, J. M.; Lobos, A. M.; Aligia, A. A.; Bauer, E. D.; Moreno, N. O.; Booth, C. H.; Goremychkin, E. A.; Sarrao, J. L.; Thompson, J. D.; Batista, C. D.; Trouw, F. R.; Hehlen, M. P. *Phys. Rev. B* **2005**, *72*, 081102.

CHAPTER 3 [†]

**IRON AND COBALT ARSENIDES: EFFECTS OF CHEMICAL PRESSURE VIA
DOPING AND A CASE OF MASKED IDENTITY BY POLYMORPHISM**

3.1   Introduction

Single crystal X-ray diffraction studies of the iron arsenide superconductors provides a

better understanding of structural details that influence superconductivity in transition metal

pnictides.[1]   Previous structural determinations of related pnictides have shown that structural

parameters, such as tetrahedral As–Fe–As bond angles approaching the ideal (109.5°),[2,3] offset

distances near 1.38 Å between a plane of Fe atoms and the pnictogen atoms,[4,5] and reduced

orthorhombic lattice distortion,[6] will impact the superconducting temperature.[1]   Unlike $CaFe_2As_2$

of the $ThCr_2Si_2$ structure type, where Fe is only in a 4-coordinate, tetrahedral, and divalent

environment, the relatively new 1-4-3 phase, $CaFe_4As_3$,[7-9] also has Fe in a square pyramidal, 5-

coordinate local environment with +1 oxidation state.[1]   The $FeAs_5$ square pyramids link multiple

$FeAs_4$ tetrahedra into a 3-dimensional architecture as shown in **Figure 3.1**.   For comparison, a

structural representation of $CaFe_2As_2$ is also provided (**Figure 3.2**.).

To manipulate the structural and physical properties of potential superconducting phases,

chemical doping[10-16] and hydrostatic pressure[17-21] have been used to suppress antiferromagnetic

order and promote superconductivity.[1]   Due to the similarities in structural and physical

properties between $CaFe_4As_3$ and the layered iron pnictides (1-2-2 phase), these two methods of

manipulation could also affect properties of a 3-dimensional phase.[1]   To test the effects of

chemical doping, single crystals of $CaFe_4As_3$, $Ca_{1-x}Yb_xFe_4As_3$, $Ca(Fe_{1-x}Co_x)_4As_3$,

----
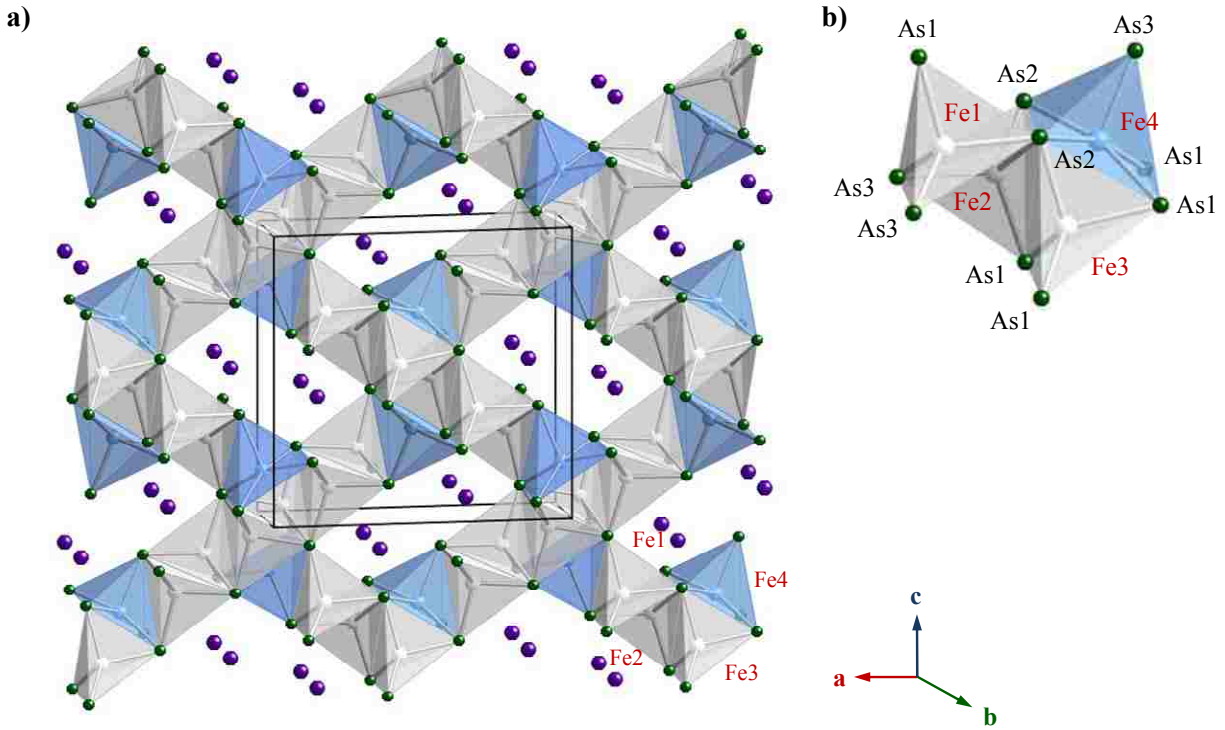
Figure 3.1.   (a) Crystal structure of undoped $CaFe_4As_3$ with Ca, Fe^{2+} (or Fe^+), and As atoms represented by purple, light gray (or blue), and green colored spheres. (b) A section of the structure showing that "Fe4 is five-fold coordinated, while [Fe1, Fe2, and Fe3] sites are fourfold coordinated with neighboring As sites."[1]

$Ca(Fe_{1-x}Cu_x)_4As_3$, and $CaFe_4(As_{1-x}P_x)_3$ were grown using a Sn flux growth method[8] and their respective properties were measured.[1]

It was hypothesized that each dopant would have distinct effects on the physical properties of undoped and doped $CaFe_4As_3$. For ambient pressure studies, the partial substitutions are carried out with $CaFe_4As_3$ in four different ways: 1) non-magnetic Yb^{2+} on the Ca^{2+} site, 2) non-magnetic P^{3-} doping on the As^{3-} sites, 3) magnetic Co^{2+} doping on the Fe^{2+} sites, and 4) non-magnetic Cu^+ doping on the Fe^+ site.[1] Based on the measurements carried out at by physics collaborators at Rice University, each dopant has a distinct effect on the physical
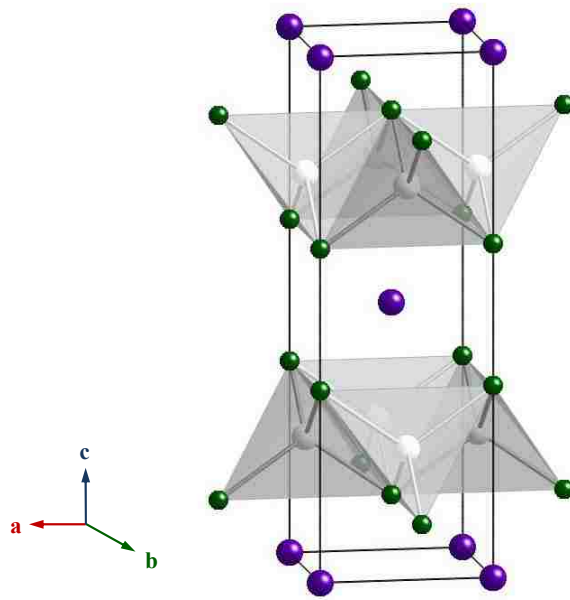
Figure 3.2.   Crystal structure of $CaFe_2As_2$ with Ca, Fe, and As atoms represented by purple, light gray, and green colored spheres, respectively.

properties. Detailed physical property analyses as well as electrical resistivity results are described in a recent publication.[1]

Magnetic transition temperatures will be briefly discussed in the context of providing conclusive proof of doping in samples where significant structural changes are not observed and doping concentration (or mixed site occupancy) cannot be conclusively refined. Difficulty has been previously reported by Kanatzidis *et al.*[22] regarding the difficulty to dope several different elements (such as Li, Na, K, Mg, Sr, La, Eu, Yb, P, Sb, Zn, Co, In, Nb, and Ni) into the various $CaFe_4As_3$ atomic sites. Therefore, caution was exercised until enough evidence of partial chemical substitution was obtained. With chemical doping on transition metal atomic site, the effect on the magnetic sublattice is very dependent on whether charge carriers and/or disorder are being incorporated. Due to ionic size of Yb and P, chemical pressure is anticipated with doping.[1]
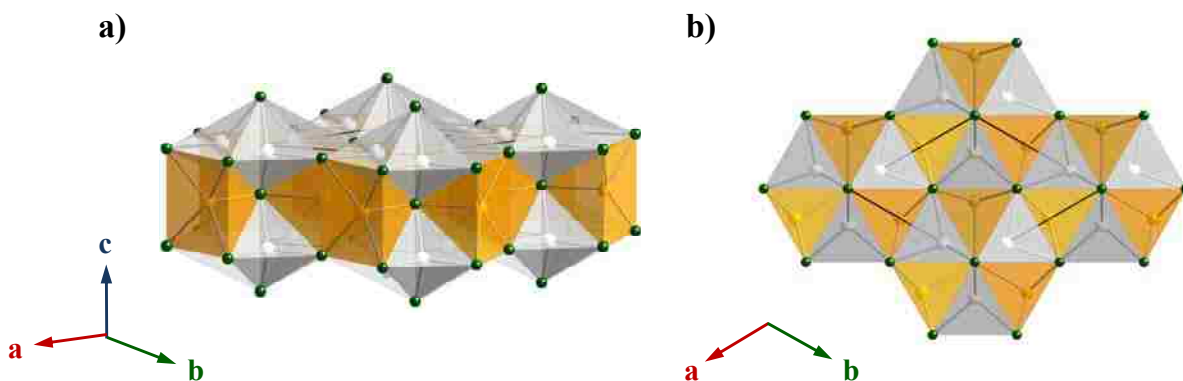
Figure 3.3. The crystal structure of FeCrAs with Fe, Cr, and As atoms represented by light gray, orange, and green colored spheres is shown with (a) *c*-axis in the vertical direction and (b) *c*-axis perpendicular to the page.

Also, there was interest in the arsenides in collaboration with another research group at LSU. We investigated undoped FeCrAs (**Figure 3.3**) and $CaFe_2As_2$ (**Figure 3.2**). With these collaborators, we have also published results in a paper exclusively devoted to the undoped $CaFe_4As_3$.[23] In an attempt to tune the properties of the 1-2-2 and 1-4-3 compounds through complete substitution (instead of doping), the growth of a new Ba-Co-As analogue of $CaFe_2As_2$ and $CaFe_4As_3$ was attempted. The former proved to be successful and conforms to the layered $ThCr_2Si_2$ structure-type. Unfortunately, the latter resulted in a different compound that was difficult to identify solely by single crystal X-ray diffraction. The difficulty turned out to be a case of masked identity by polymorphism. A clue to the true identity of this compound was found in a paper on high temperature X-ray diffraction experiments reported by Selte and Kjekshus.[24] A comparison of experimental and calculated powder X-ray diffraction confirmed this clue. Ultimately, after a series of unit cell transformations, the single crystal structure was determined. A high temperature polymorph of CoAs was grown and its structure matches with the hexagonal NiAs structure type ($P6_3/mmc$),[25] instead of the expected orthorhombic MnP structure type (*Pnma*).[26] Both these structure-types are shown in **Figures 3.4a and 3.4b**,

respectively. The difference between the transition metal point group symmetry within the two

structure-types is illustrated in **Figure 3.5**.
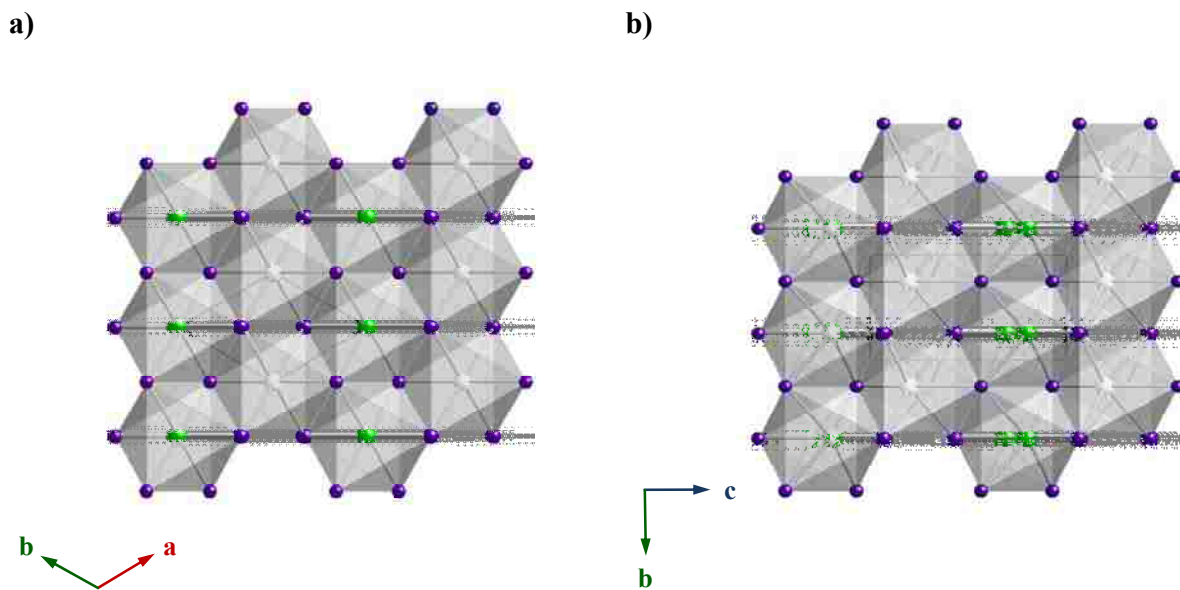
Figure 3.4.   The crystal structures shown are (a) hexagonal NiAs structure type ($P6_3/mmc$) and (b) orthorhombic MnP structure-type ($Pnma$). Transition metal and pnictogen atoms represented by green and purple colored spheres.
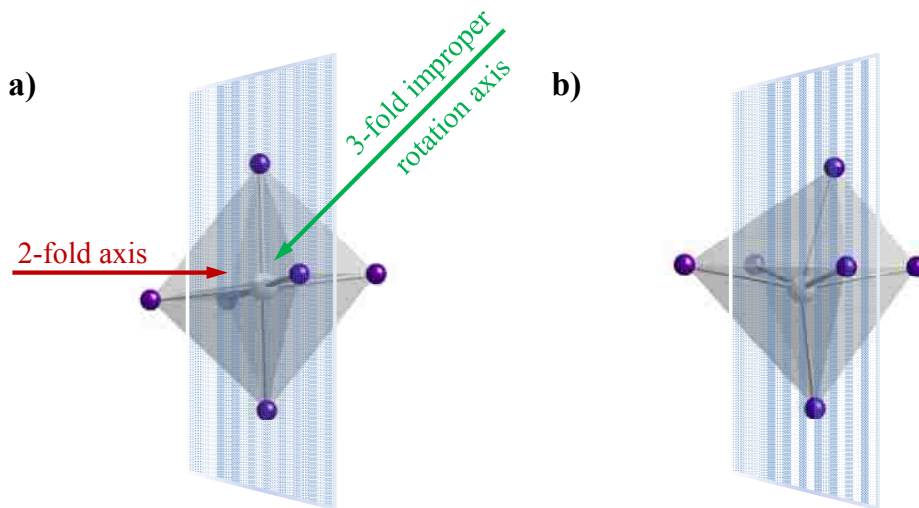
Figure 3.5.   Representation of transition metal polyhedral within (a) hexagonal NiAs structure type and (b) orthorhombic MnP structure type with D_{3d} and C_s point group symmetry, respectively.

3.2 Experimental Details

3.2.1. Yb, Co, Cu, or P Doped CaFe$_4$As$_3$

"Room temperature single-crystal X-ray diffraction experiments were performed" on undoped and doped CaFe$_4$As$_3$ samples (Ca$_{1-x}$Yb$_x$Fe$_4$As$_3$, Ca(Fe$_{1-x}$Co$_x$)$_4$As$_3$, Ca(Fe$_{1-x}$Cu$_x$)$_4$As$_3$, and CaFe$_4$(As$_{1-x}$P$_x$)$_3$) using "a Nonius KappaCCD X-ray diffractometer with Mo Kα radiation source (λ = 0.71073 Å) and a graphite monochromator" to solve the crystal structure."[1] "Single crystals with a low crystal mosaicity (~0.4°) were selected from each sample batch and mounted on the tips of thin glass fibers with epoxy. Data were collected at a lower symmetry (monoclinic, 2/m) than the previously reported crystal system (orthorhombic), and intensities were recorded at a crystal-to-detector distance of 30 mm, between a 2θ angle of 5° and 60°. All of the data collections had the same list of suggested systematic reflection conditions (h00: h = 2n, 0k0: k = 2n, 00l: l = 2n, hk0: h = 2n, 0kl: k + l = 2n, hh0: h = 2n), lattice type (Primitive), and Laue symmetry (mmm). Structure determinations were made using WINGX[27] with SIR97[28] and SHELXL-97.[29] PLATON[30] was used to check for missed symmetry (ADDSYM option). The best models of the diffraction data are refined with orthorhombic space group $Pnma$ (no. 62)."[1]

"Chemical analysis was performed at LSU on an FEI Quanta 200 scanning electron microscope (SEM) with an energy-dispersive X-ray (EDX) spectrometer. The measurements were carried out on the same single crystals used for the physical property measurements, and the doping concentration of each element was determined. Each crystal was scanned at four areas per crystal for 50 seconds per area, with an accelerating voltage of 20 kV and a beam-to-sample distance of 15 mm. The average composition was normalized with the Ca site."[1]

3.2.2. High Temperature Polymorph of CoAs

Single crystals of CoAs were synthesized by collaborators at LSU Physics using the flux method. A similar strategy as provided in **Section 3.2.1.** was used to collect single crystal X-ray

diffraction data on crystals with mosaicity between 0.5° and 0.6°. Our best models of the X-ray diffraction data are refined with the hexagonal space group $P6_3/mmc$ (no. 194).[1]

3.3 Results and Discussion

3.3.1 Preliminary Evaluation of All Samples

Prior to single crystal measurements, room-temperature powder X-ray diffraction experiments were conducted at Rice University on a Rigaku D/Max diffractometer to determine the phase purity of the undoped and doped $CaFe_4As_3$ samples ($Ca_{1-x}Yb_xFe_4As_3$, $Ca(Fe_{1-x}Co_x)_4As_3$, $Ca(Fe_{1-x}Cu_x)_4As_3$, and $CaFe_4(As_{1-x}P_x)_3$). It is important to note that Sn flux diffraction peaks were not present in the X-ray diffraction powder patterns.[1]

3.3.2 $CaFe_4(As_{1-x}P_x)_3$ and $Ca_{1-x}Yb_xFe_4As_3$

With both $CaFe_4(As_{1-x}P_x)_3$ and $Ca_{1-x}Yb_xFe_4As_3$ samples, the lattice parameters and unit cell volume obtained from single-crystal X-ray diffraction data are not statistically different than the undoped $CaFe_4As_3$ (**Table 3.1**). This is not surprising due to the size similarities of the cations (Yb^{2+}, 1.08 Å; Ca^{2+} 1.06 Å)[31] and the anions (As^{3-}, 2.22 Å; P^{3-}, 2.12 Å)[32] substituted.[1]

Table 3.1. Lattice Parameters and Unit Cell Volume for $CaFe_4(As_{1-x}P_x)_3$ and $Ca_{1-x}Yb_xFe_4As_3$[1]

Dopant		P			Yb
x (nominal)	0	0.05	0.1	0.25	0.2
x (EDX)	0	Crystal 1	Crystal 2	Crystal 3	0.17
a (Å)	11.919 (3)	11.917 (3)	11.915 (5)	11.911 (2)	11.910 (2)
b (Å)	3.749 (1)	3.748 (1)	3.746 (2)	3.746 (1)	3.748 (1)
c (Å)	11.624 (3)	11.622 (4)	11.619 (5)	11.617 (2)	11.617 (3)
V (Å^3)	519.3 (2)	519.1 (3)	518.6 (4)	518.3 (2)	518.6 (2)

Quantification of the actual P concentration in the P-doped crystal samples with three different nominal concentrations (x = 0.05, 0.1, or 0.25) were not achieved by elemental analysis (EDX) and assumed that the amount is below the instruments level of detection (less the 5-10%). The opposite is true for the Yb-doped sample. Its concentration, x, was ~0.17 and close to the targeted nominal Yb concentration (x = 0.2).[1]

Evidence of P-doping can be found in the reported magnetic transition temperatures.[1] With an applied magnetic field of 0.1 T along the b axis, the $CaFe_4(As_{1-x}P_x)_3$ sample with the highest nominal concentration (x = 0.25) has its first magnetic transition at ~83 K (Néel temperature, T_N). This transition temperature is lower than observed for $CaFe_4As_3$ (T_N ~88 K). The P-doped sample also has a higher second magnetic transition temperature, T_2, (~26 K) than the undoped sample (~33 K). These differences in magnetic transition temperatures are due to small amount of P substitution on the As atomic sites.[1]

With a Yb doping concentration x of ~0.17, there was very little change with T_N in comparison to the undoped sample. However, a significant difference was detected with T_2 which was increased from ~26 K to ~38 K with Yb-doping.[1]

3.3.3 $Ca(Fe_{1-x}Co_x)_4As_3$ and $Ca(Fe_{1-x}Cu_x)_4As_3$

Co-doping was carried out in six different targeted concentrations. Based on elemental analysis, measurable quantities were observed and actual concentrations (x = 0.05, 0.07, 0.1, 0.16, 0.2, 0.32) ranged from statistically equivalent to or less than half the nominal concentration (x = 0.05, 0.1, 0.2, 0.3, 0.4, 0.6). Unfortunately, the amount of Cu-doping could not be quantified as its actual concentration fell below the level of detection by EDS (less than 5-10%).[1]

Lattice parameters and unit cell volume decrease for the $Ca(Fe_{1-x}Co_x)_4As_3$ series of compounds as a function of increased Co concentration x (**Table 3.2 - 3.3**). The largest lattice reduction occurs in the size of the *ac*-plane with statistically negligible change along the *b*-axis.

For the one $Ca(Fe_{1-x}Cu_x)_4As_3$ sample, no significant dimensional changes are measured in the lattice parameters and unit cell volume (**Table 3.3**).[1]

Table 3.2. Lattice Parameters and Unit Cell Volume for $Ca(Fe_{1-x}Co_x)_4As_3$ $0 \leq x(\text{nominal}) \leq 0.3$[1]

Dopant		Co			
x (nominal)	0	0.05	0.1	0.2	0.3
x (EDX)	0	0.05	0.07	0.1	0.16
a (Å)	11.919 (3)	11.917 (2)	11.914 (4)	11.907 (2)	11.902 (2)
b (Å)	3.749 (1)	3.750 (1)	3.749 (1)	3.748 (1)	3.748 (1)
c (Å)	11.624 (3)	11.618 (2)	11.611 (4)	11.600 (2)	11.587 (3)
V (Å^3)	519.3 (2)	519.1(2)	518.6(2)	517.6(2)	516.9(1)

Table 3.3. Lattice Parameters and Unit Cell Volume for $Ca(Fe_{1-x}Co_x)_4As_3$ $0.4 \leq x(\text{nominal}) \leq 0.6$ and $Ca(Fe_{1-x}Cu_x)_4As_3$[1]

Dopant	Co		Cu
x (nominal)	0.4	0.6	0.25
x (EDX)	0.2	0.32	(see text)
a (Å)	11.897 (2)	11.878 (2)	11.919 (3)
b (Å)	3.747 (1)	3.745 (1)	3.751 (1)
c (Å)	11.571 (3)	11.533 (2)	11.623 (3)
V (Å^3)	515.8 (1)	513.0 (2)	519.6 (2)

With three unique 4-coordinate tetrahedral (Fe^{2+}) and only one unique 5-coordinate square pyramidal (Fe^+) atomic site, it is of interest to determine whether there would site preference for Co- and Cu-doping in $CaFe_4As_3$. Preference was noted by Kanatzidis *et al.* in a recent publication for which they concluded that Cr is not randomly distributed on all the Fe sites. Instead, Cr-doping occurs at the Fe^+ sites.[22] For the Cu-doped series, there is greater bond

length decrease with the Fe-As bonds involving the 4-coordinate sites (Fe1, Fe2, and Fe3) than

the 5-coordinate site (Fe4) as shown in **Table 3.4** and **Figure 3.6**. This appears to be evidence of

site preference when doping with Co. Due to insufficient bond length changes with Cu-doping, a

similar evaluation is inconclusive.[1]

Magnetic transition temperatures are markedly altered in reported measurements for the

crystals of $Ca(Fe_{1-x}Co_x)_4As_3$.[1] The first transition, T_N, is reduced down to ~65 K when the actual

doping concentration $x = 0.32$ and the second transition, T_2, is suppressed below 2 K for all the

samples with $x \geq 0.1$. This report[1] also provides evidence of Cu-doping with the change in the

second magnetic transition temperature. This change is a significant increase in T_2 from ~26 K

to ~40 K with Cu-doping. The insignificant change in T_N may be due to the doping only on the

Fe^+ sites with Cu^+. This scenario of doping doesn't add charge carriers to the magnetic

sublattice.[1]

Table 3.4. Fe-As Bond Lengths d in $Ca(Co_{1-x}Fe_x)_4As_3$ ($x = 0$ and 0.32) and $\Delta d = d(x = 0.32) - d(x = 0)$[1]

Bond	Bond length d (Å)		Δd (Å)
	$x = 0$	$x = 0.32$	
Fe1—As1	2.3854(8)	2.3681(11)	-0.0173(19)
Fe1—As2	2.4191(9)	2.3932(11)	-0.0259(20)
Fe1—As3 (x2)	2.4139(6)	2.4030(7)	-0.0109(13)
Fe2—As1	2.4434 (8)	2.4206 (10)	-0.0228 (18)
Fe2—As2 (x2)	2.4677(6)	2.4410(7)	-0.0267(13)
Fe2—As3	2.4359(8)	2.4049(10)	-0.0310(18)
Fe3—As1 (x2)	2.4343(6)	2.3882(10)	-0.0461(16)
Fe3—As1	2.4245(9)	2.3961(7)	-0.0284(16)
Fe3—As2	2.3920(8)	2.3619(11)	-0.0301(19)
Fe4—As1 (x2)	2.6122(6)	2.6169(7)	0.0047(13)
Fe4—As2 (x2)	2.5787(6)	2.5790(7)	0.0003(13)
Fe4—As3	2.4328(8)	2.4141(11)	-0.0187(19)
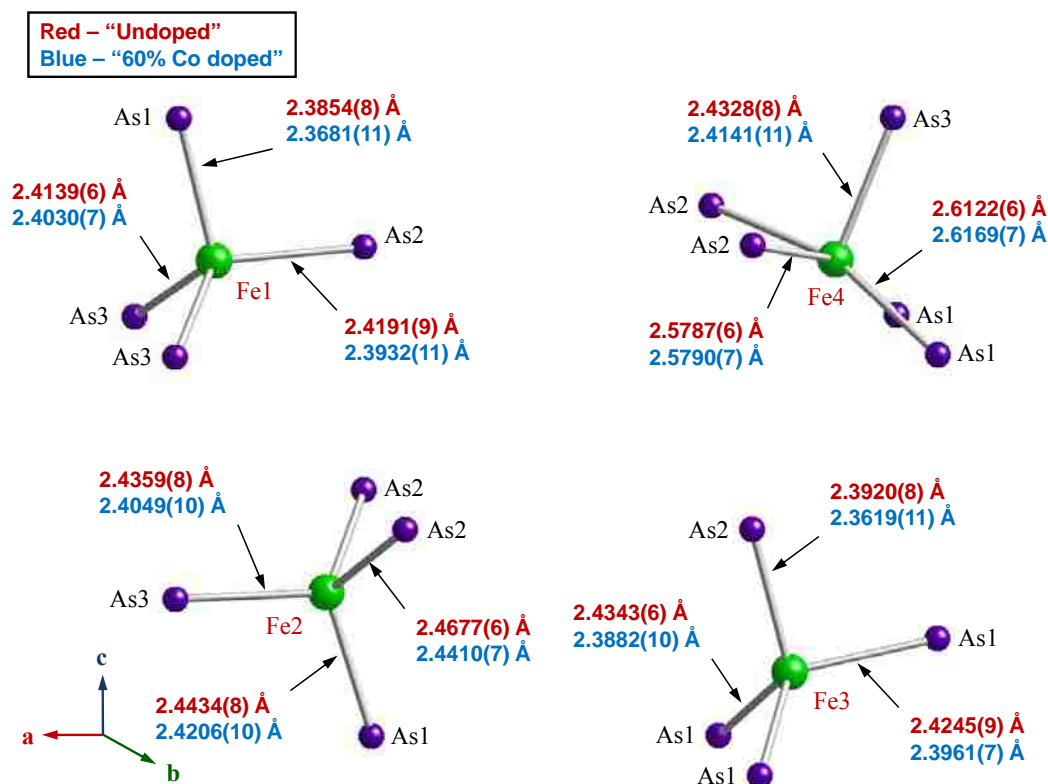
Figure 3.6. The four Fe coordination environments within the structure of $CaFe_4As_3$ with bond lengths. Fe(4) is five-fold coordinated, while Fe(1-3) sites are four-fold coordinated with neighboring As sites.

3.3.4 Identification of an Unexpected High Temperature Polymorph (CoAs)

The structure determination of CoAs went neither as planned (due to an incorrect assumption as to its identity prior to any X-ray experiments) nor as could be predicted (since the solved structure would not have been expected at first even if we had known the crystal's true identity). To clarify this statement, this binary's story shall be unfolded below.

In the targeted synthesis of $BaCo_2As_2$ using Sn flux, two products formed that could be visually separated by crystal morphology. One of the two products was easily identified by single crystal X-ray diffraction as the desired $BaCo_2As_2$ compound. The other product was

speculated as possibly a new Ba-Co-As phase and assumed to be isostructural to $CaFe_4As_3$ based on its flat blade crystal morphology.

This assumption was based on the crystal growth of $CaFe_2As_2$ that also contained blade-shaped $CaFe_4As_3$ crystals as a secondary phase. However, single crystal X-ray diffraction experiments did not support this proposition with the measured orthorhombic unit cell parameters of $a \approx 7.06$ Å, $b \approx 10.50$ Å, and $c \approx 12.51$ Å. Also, there were indicators during the structure refinement of possibly higher hexagonal symmetry, which can occur when the c/a ratio is approximately equal to the square root of three. After a thorough frame by frame analysis of the individual diffraction images, it became evident that the crystal structure determination might be hampered by crystal twinning (see **Figure 3.7** for evidence of non-merohedral twinning).
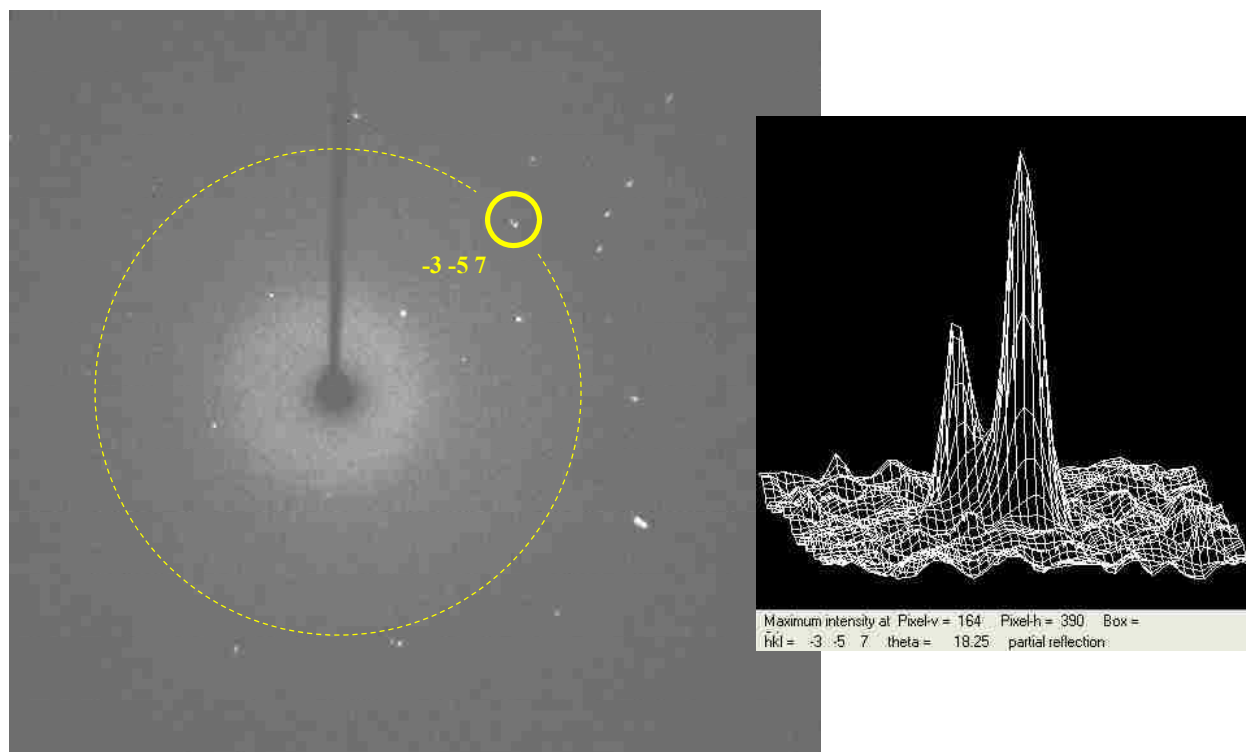
Figure 3.7. Diffraction image (left) taken during a data collection with the first batch of CoAs crystals which shows clear signs of non-merohedral twinning with significant peak splitting. A profile image (right) shows that both peaks have significant intensities above the background.

38

Targeting growth of $BaCo_4As_3$, a second batch of blade-shaped crystals proved to be better quality (mosaic spread less than 1°) and single crystal X-ray diffraction data was collected on a crystal with a mosaicity of 0.482(3)°. However, the preliminary lattice parameters ($a = 3.57$ Å, $b = 5.25$ Å, and $c = 6.24$ Å) did not match the expected values for $BaCo_4As_3$ and were half the volume measured in the first batch of crystals.

A powder X-ray diffraction pattern on this second batch was then obtained and compared to all the known unaries, binaries, ternaries, and quaternaries that contain the elements Ba, Co, As, and Sn in the Joint Committee on Powder Diffraction Standards (JCPDS) powder database. Unfortunately, there were no powder diffraction pattern matches found in this database. Although the powder pattern was different for CoAs, the unit cell parameters determined from the single crystal data were close to the values previously reported for this binary phase.

A paper by Selte and Kjekshus[24] noted that the b and c lattice dimensions converge at high temperature (1248 ± 20 K). This convergence coincides with a structural transition from an orthorhombic to a hexagonal structure. An overlay of the experimental X-ray powder pattern with the calculated powder patterns was generated from crystallographic information files exported from ICSD (reference code no. 043399 for MnP[26] and 031062 for NiAs).[25] The experimental powder diffraction pattern matches with the hexagonal NiAs structure type ($P6_3/mmc$) better than the orthorhombic MnP structure type ($Pnma$) as shown in **Figure 3.8**. Therefore, it was concluded that the high temperature hexagonal polymorph of CoAs was stabilized via flux methods.

The raw data could not be processed and scaled directly into a hexagonal crystal system. Therefore, modeling of the data had to begin using an orthorhombic space group. The pathway from orthorhombic (starting with the space group with the highest figure of merit) to hexagonal with each transformation matrix needed for each space group change is the following:

1. Work on model in space group, $P2_1mn$ (No. 31), $R_1 = 0.07$

2. Apply transformation matrix (1 0 0, 0 -1 0, 0 0 -1)

3. Work on model in space group, $Pmmn$ (No. 59), $R_1 = 0.07$

4. Apply transformation matrix (1 0 0, 0 0 1, 0 -1 0)

5. Work on model in space group, $Cmcm$ (No. 63), $R_1 = 0.038$

6. Apply transformation matrix (1 0 0, -0.5 -0.5 0, 0 0 -1)

7. Finally, solve structure in space group, $P6_3/mmc$ (No. 194), $R_1 = 0.041$
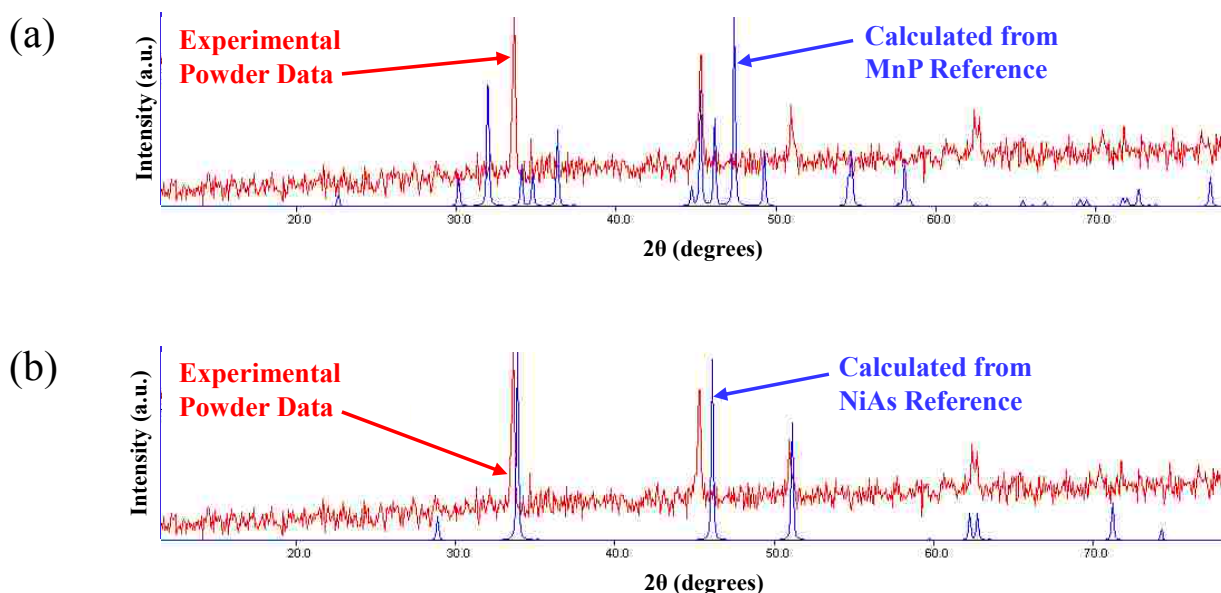
Figure 3.8.   Identification of structure type by overlaying experimental CoAs powder X-ray diffraction data (shown in red) with calculated powder patterns (shown in blue) of either using (a) MnP, ICSD ref. code no. 043399, or (b) NiAs, ICSD ref. code no. 031062.

Elemental analysis was performed by Galbraith Laboratory afterwards. This analysis confirmed this binary identification as a 1-1 phase.

40

3.4   Conclusions

In the cases of P-, Yb- and Cu-doping, the unit cell dimensions remain statistically the same as the undoped $CaFe_4As_3$ sample. Of these three doping strategies, only Yb-doping could be quantified by elemental analysis (EDX) where the actual concentration ($x = 0.17$) was close to the nominal concentration ($x = 0.2$). Significant changes in magnetic transition temperatures were observed in all the P-, Yb- and Cu-doped samples (Yb-doping: T_2 increases from ~26 K to ~38 K; Cu-doping: T_2 increases from ~26 K to ~40 K; P-doping: T_2 increases from ~26 K to ~33 K and T_N decreases from ~88 K to ~83 K).[1]

The $Ca(Fe_{1-x}Co_x)_4As_3$ series demonstrate a small but significant decrease in lattice parameters and unit cell volume that correlates with increasing Co concentration. Elemental analysis could be used to confirm all the actual Co concentrations ($x = 0.05, 0.07, 0.1, 0.16, 0.2, 0.32$). The first magnetic transition temperature, T_N, is ~65 K when $x = 0.32$ and the second magnetic transition temperature, T_2, is suppressed below 2 K when $x \geq 0.1$.[1]

High T_c has been correlated with tetrahedral As–Fe–As bond angles approaching the ideal (109.5°),[2,3] and offset distances near 1.38 Å between a plane of Fe atoms and the pnictogen atoms.[4,5] For the undoped sample, the three $FeAs_4$ tetrahedra are distorted away from the ideal with a significant range of bond angles (Fe1: 98.84(3) – 113.26(2)°, Fe2: 93.64(3) – 116.38(2)°, Fe3: 100.09(3) – 115.03(2)°). Also, only 1 of the 3 unique As atoms is close to the targeted offset distance from the plane of Fe atoms (closest offset for As1 ≈ 1.581 Å, As2 ≈ 1.507 Å, As3 ≈ 1.398 Å). Structurally, Co doping by far has the largest impact on parameters associated with superconductivity as well as the first two magnetic transition temperatures. The range of the tetrahedral As–Fe–As bond angles were reduced (Fe1: 100.19(4) – 112.00(3)°, Fe2: 95.38(4) – 115.61(3)°, Fe3: 102.38(4) – 113.78(3)°) and the As atoms are closer to the targeted offset

distance from the plane of Fe atoms (closest offset for As1 ≈ 1.518 Å, As2 ≈ 1.446 Å, As3 ≈ 1.389 Å).[1]

Single crystal and powder X-ray diffraction methods were used to determine the structure of CoAs which was confirmed by elemental analysis. The stabilization of a high temperature polymorph of CoAs was an unexpected result in exploratory flux-growth synthesis of a Ba-Co-As phase. Further synthetic experiments are needed to see if Ba played a role in stabilizing the hexagonal NiAs structure type ($P6_3/mmc$) of CoAs. If Ba is a key component to obtain the NiAs structure-type, it could also help stabilizing high temperature polymorphs of other transition metal pnictides.

3.5   References

(1)   Zhao, L. L.; Kim, S. K.; McCandless, G. T.; Torikachvili, M. S.; Canfield, P. C.; Chan, J. Y.; Morosan, E. *Phys. Rev. B* **2011**, *84*, 104444.

(2)   Lee, C. H.; Iyo, A.; Eisaki, H.; Kito, H.; Fernandez-Diaz, M. T.; Ito, T.; Kihou, K.; Matsuhata, H.; Braden, M.; Yamada, K. *J. Phys. Soc. Jpn.* **2008**, *77*, 083704.

(3)   Zhao, J.; Huang, Q.; de la Cruz, C.; Li, S. L.; Lynn, J. W.; Chen, Y.; Green, M. A.; Chen, G. F.; Li, G.; Li, Z.; Luo, J. L.; Wang, N. L.; Dai, P. C. *Nat. Mater.* **2008**, *7*, 953-959.

(4)   Mizuguchi, Y.; Hara, Y.; Deguchi, K.; Tsuda, S.; Yamaguchi, T.; Takeda, K.; Kotegawa, H.; Tou, H.; Takano, Y. *Supercond. Sci. Technol.* **2010**, *23*, 054013.

(5)   Okabe, H.; Takeshita, N.; Horigane, K.; Muranaka, T.; Akimitsu, J. *Phys. Rev. B* **2010**, *81*, 205119

(6)   Nandi, S.; Kim, M. G.; Kreyssig, A.; Fernandes, R. M.; Pratt, D. K.; Thaler, A.; Ni, N.; Bud'ko, S. L.; Canfield, P. C.; Schmalian, J.; McQueeney, R. J.; Goldman, A. I. *Phys. Rev. Lett.* **2010**, *104*, 057006.

(7)   Todorov, I.; Chung, D. Y.; Malliakas, C. D.; Li, Q. A.; Bakas, T.; Douvalis, A.; Trimarchi, G.; Gray, K.; Mitchell, J. F.; Freeman, A. J.; Kanatzidis, M. G. *J. Am. Chem. Soc.* **2009**, *131*, 5405–5407.

(8)   Zhao, L. L.; Yi, T. H.; Fettinger, J. C.; Kauzlarich, S. M.; Morosan, E. *Phys. Rev. B* **2009**, *80*, 020404.

(9)   Yi, T. H.; Dioguardi, A. P.; Klavins, P.; Curro, N. J.; Zhao, L. L.; Morosan, E.; Kauzlarich, S. M. *Eur. J. Inorg. Chem.* **2011**, 3920-3925.

(10)   Ren, Z. A.; Yang, J.; Lu, W.; Yi, W.; Shen, X. L.; Li, Z. C.; Che, G. C.; Dong, X. L.; Sun, L. L.; Zhou, F.; Zhao, Z. X. *Europhys. Lett.* **2008**, *82*, 57002.

(11)   Cheng, P.; Fang, L.; Yang, H.; Zhu, X.; Mu, G.; Luo, H.; Wang, Z.; Wen, H. *Sci. China Ser. G-Phys. Mech. Astron.* **2008**, *51*, 719-722.

(12)   Canfield, P. C.; Bud'ko, S. L. In *Annual Review of Condensed Matter Physics, Vol 1*; Langer, J. S., Ed.; Annual Reviews: Palo Alto, 2010; Vol. 1, p 27-50.

(13)   Rotter, M.; Pangerl, M.; Tegel, M.; Johrendt, D. *Angew. Chem.-Int. Edit.* **2008**, *47*, 7949-7952.

(14)   Ni, N.; Tillman, M. E.; Yan, J. Q.; Kracher, A.; Hannahs, S. T.; Bud'ko, S. L.; Canfield, P. C. *Phys. Rev. B* **2008**, *78*, 214515.

(15)   Jiang, S.; Xing, H.; Xuan, G. F.; Wang, C.; Ren, Z.; Feng, C. M.; Dai, J. H.; Xu, Z. A.; Cao, G. H. *J. Phys.-Condes. Matter* **2009**, *21*, 382203.

(16)   Chen, X. H.; Wu, T.; Wu, G.; Liu, R. H.; Chen, H.; Fang, D. F. *Nature* **2008**, *453*, 761-762.

(17)   Takahashi, H.; Igawa, K.; Arii, K.; Kamihara, Y.; Hirano, M.; Hosono, H. *Nature* **2008**, *453*, 376-378.

(18)   Alireza, P. L.; Ko, Y. T. C.; Gillett, J.; Petrone, C. M.; Cole, J. M.; Lonzarich, G. G.; Sebastian, S. E. *J. Phys.-Condes. Matter* **2009**, *21*, 012208.

(19)   Colombier, E.; Bud'ko, S. L.; Ni, N.; Canfield, P. C. *Phys. Rev. B* **2009**, *79*, 224518.

(20)   Ishikawa, F.; Eguchi, N.; Kodama, M.; Fujimaki, K.; Einaga, M.; Ohmura, A.; Nakayama, A.; Mitsuda, A.; Yamada, Y. *Phys. Rev. B* **2009**, *79*, 172506.

(21)   Fukazawa, H.; Takeshita, N.; Yamazaki, T.; Kondo, K.; Hirayama, K.; Kohori, Y.; Miyazawa, K.; Kito, H.; Eisaki, H.; Iyo, A. *J. Phys. Soc. Jpn.* **2008**, *77*, 105004.

(22)   Todorov, I.; Chung, D. Y.; Claus, H.; Gray, K. E.; Li, Q. A.; Schleuter, J.; Bakas, T.; Douvalis, A. P.; Gutmann, M.; Kanatzidis, M. G. *Chem. Mater.* **2010**, *22*, 4996-5002.

(23)   Karki, A. B.; McCandless, G. T.; Stadler, S.; Xiong, Y. M.; Li, J.; Chan, J. Y.; Jin, R. *Phys. Rev. B* **2011**, *84*, 054412.

(24)   Selte, K.; Kjekshus, A. *Acta Chem. Scand.* **1973**, *27*, 3195-3206.

(25)   Aminoff, G. *Z. Kristall.* **1923**, *58*, 203-219.

(26)   Rundqvist, S. *Acta Chem. Scand.* **1962**, *16*, 287-292.

(27)   Farrugia, L. J. *J. Appl. Crystallogr.* **1999**, *32*, 837-838.

(28)   Altomare, A.; Burla, M. C.; Camalli, M.; Cascarano, G. L.; Giacovazzo, C.; Guagliardi, A.; Moliterni, A. G. G.; Polidori, G.; Spagna, R. *J. Appl. Crystallogr.* **1999**, *32*, 115-119.

(29)   Sheldrick, G. M. *Acta Crystallogr. Sect. A* **2008**, *64*, 112-122.

(30)   Spek, A. L. *J. Appl. Crystallogr.* **2003**, *36*, 7-13.

(31)   Shannon, R. D. *Acta Crystallogr. Sect. A* **1976**, *32*, 751-767.

(32)   Pearson, R. G. *Inorg. Chem.* **1991**, *30*, 2856-2858.

Sr$_3$Ru$_2$O$_7$: SPACE GROUP DETERMINATION, CYCLING TEMPERATURE DEPENDENCE STUDY, AND CHEMICAL DOPING EFFECT WITH MANGANESE

4.1 Introduction

The strontium ruthenate members, Sr$_{n+1}$Ru$_n$O$_{3n+1}$ (n = 1, 2, 3, …∞), of the Ruddlesden-Popper series[1,2] are multi-faceted in the range of magnetic properties reported.[3] For instance, the first member of this series, Sr$_2$RuO$_4$ (n = 1), is superconducting[4] while the next member, Sr$_3$Ru$_2$O$_7$ (n = 2), is paramagnetic with short range antiferromagnetic (AFM) correlations.[3,5] Also, Sr$_4$Ru$_3$O$_{10}$ (n = 3) and SrRuO$_3$ (n = ∞) are both known to be ferromagnetic (FM) metals.[3,6,7] In previous bulk[8,9] and surface[10-12] studies, it has been shown the magnetic properties of Sr$_2$RuO$_4$ (undoped and Ca-doped) are highly correlated to the lattice distortions in their structures.[3] This correlation is also confirmed by theoretical calculations for which there is a competition between FM (due to RuO$_6$ octahedral rotation) and AFM (due to RuO$_6$ octahedral tilt).[3,13] These unique correlations need further analysis to elucidate the underlying mechanism for the properties found with the Ruddlesden-Popper series.[3] Due to the wide range of properties in this series and the correlations determined by others,[4,6,7,13,14] the strontium ruthenates may serve an excellent model to study.[3]

Sr$_3$Ru$_2$O$_7$ has significantly different properties than the other members of its series. Based on ambient pressure magnetic susceptibility[5,14] and neutron scattering measurements,[15]

$Sr_3Ru_2O_7$ has only short-range AFM-type magnetic ordering below $\sim$ 20 K.[3] When the pressure is increased (using hydrostatic or uniaxial pressure)[14,16] or a magnetic field is applied, a ferromagnetically ordered state is induced and a metamagnetic transition occurs.[3,17] Based on these reports, $Sr_3Ru_2O_7$ is a highly correlated compound for which the structure can be manipulated in order to influence the competition between magnetic interactions (AFM vs. FM). The metal-insulator transition for $Sr_3Ru_2O_7$ can be easily affected with chemical pressure by doping the Ru site with small amounts of Mn.[3,18,19]

Recent X-ray diffraction studies were conducted on single crystals to provide structural insight to a series of compounds. This investigation began with determining the most appropriate space group for the ruthenium end-member, $Sr_3Ru_2O_7$. Although the structure of this compound has been published by other research groups, $Sr_3Ru_2O_7$ has, so far, been modeled in three different space groups including *I4/mmm* (tetragonal, No. 139),[20-22] *Pban* (orthorhombic, No. 50),[5] and *Bbcb* (orthorhombic, No. 68).[23-26]

Another part of this study is to evaluate the temperature dependence of the unit cell lattice parameters. It was reported by Shaked and co-workers[24] in a neutron powder diffraction study that there was a noticeable increase in the ratio of the lattice parameter *c* divided by the average of lattice parameters *a* and *b* after each successive thermal cycle. Their conclusion from this observation was that strain within the crystal lattice was being relieved each time that the sample was cooled and subsequently warmed. The authors explain that strain is geometrically predicted (using a rearranged form of the Goldschmidt tolerance factor[27] and oxygen radii, R_O, of 0.41 Å) in perovskite-like $A_3M_2O_7$ compounds when the transition metal radii, R_M, is greater than $0.71R_A - 0.41$ (where R_A = alkaline/rare earth metal radii). For the compound $Sr_3Ru_2O_7$ using radii distances of 0.62 Å (Ru^{4+}) and 1.44 Å (Sr^{2+}), there should be slight compression which may be the cause (or part of the cause) of the RuO_6 octahedral rotation.

The influence of chemical substitution (or doping) of Mn on the Ru atomic site of $Sr_3Ru_2O_7$ was evaluated.[19] Single crystal X-ray diffraction data was collected and the structure modeled for seven Mn-doping levels in the $Sr_3(Ru_{1-x}Mn_x)_2O_7$ series (x = 0.07, 0.09, 0.17, 0.20, 0.24, 0.33, 0.73).[19] During this investigation, it was determined that two of the Mn-doped sample are a mixture of two phases, Mn-doped $Sr_3Ru_2O_7$ and Mn-doped $Sr_4Ru_3O_{10}$. Single crystal and powder X-ray diffraction results support the co-existence of the n = 2 (containing bi-layers of corner-sharing RuO_6 octahedra) and the n = 3 (containing tri-layers of corner-sharing RuO_6 octahedra) structures of the Ruddlesden-Popper series, $Sr_{n+1}Ru_nO_{3n+1}$, within some of the batches of crystals.

4.2   Experimental Details

"Single crystals of $Sr_3Ru_2O_7$ were grown using the floating-zone technique to produce high-quality crystals. A detailed description[15] of the growth procedure of $Sr_3Ru_2O_7$ single crystals can be found in our previous publication."[3] $Sr_3(Ru_{1-x}Mn_x)_2O_7$ ($0 \leq x \leq 0.7$) crystals were also grown by this method. "To avoid oxygen deficiency, 10 atm of oxygen gas pressure was applied during the growth."[19] "The crystal structure and Mn concentration (x) were determined by single-crystal X-ray refinement."[19]

Single crystals, ranging in sizes from $0.02 \times 0.05 \times 0.07$ mm^3 to $0.03 \times 0.10 \times 0.12$ mm^3, of $Sr_3Ru_2O_7$ and the $Sr_3(Ru_{1-x}Mn_x)_2O_7$ series were mounted on thin glass fibers with epoxy. "After the epoxy had hardened, [a light coat of] vacuum grease was applied" around the interface of the single crystal and the glass fiber to alleviate the concern that the epoxy might become brittle during the 90 K data collections.[3] All single crystal X-ray diffraction data collections were "conducted on a Nonius KappaCCD X-ray diffractometer [equipped] with a Mo Kα radiation source (λ = 0.71073 Å), a graphite monochromator, and an Oxford Cryosystems 700 series cryostream controller."[3] Data was collected at "a lower symmetry (monoclinic, 2/m)" than

47

the previously reported crystal systems (orthorhombic and tetragonal).[3]   Initial space group

determination and preliminary models were done "using the maXus software package with

SIR97[28] and SHELXL-97[29] software.   Final refinement was completed using WinGX[30] and

SHELXL-97.   Missing symmetry was checked using the 'ADDSYM' test in the PLATON[31]

program."[3]

For the thermal cycle experiments, diffraction images were collected "at three different

temperatures (298 K, 200 K, and 90 K) after allowing approximately 30 min for the temperature

of the crystal (under a cryostream) to stabilize"[3] after cooling or warming at a rate of 5 K/minute.

A single thermal cycle is defined and was carried out in the "following manner: 1) collect data at

298 K, 2) cool to 200 K, 3) collect data at 200 K, 4) cool to 90 K, 5) collect data at 90 K, 6)

warm to 200 K, 7) collect data at 200 K, and 8) warm to 298 K."[3]   After a single thermal cycle

was completed, the next cycle was started immediately.   This experiment consisted of three

successive thermal cycles producing a total of thirteen data sets to evaluate.[3]

Powder X-ray diffraction was performed on a Bruker D8 Advance powder diffractometer

equipped with Cu Kα radiation source (λ = 1.54184 Å) with a germanium incident beam

monochromator.   The sample was prepared by grinding single crystals (which were previously

grown in the same batch) to a fine powder in a mortar and pestle.   Intensities were recorded over

a 2θ angle range of 5° to 80°.

4.3   Results and Discussion

4.3.1   Space Group Determination of $Sr_3Ru_2O_7$ at Room Temperature

From single crystal X-ray diffraction experiment, $Sr_3Ru_2O_7$ was determined to crystallize

in the tetragonal space group "$I4/mmm$ (No. 139) [consisting of six occupied Wyckoff sites:] Sr1

($4/mmm$), Sr2 ($4mm$), Ru ($4mm$), O1 ($4/mmm$), O2 ($4mm$), and O3 (m)."[3]   The structure (**Figure

4.1a**) contains a bi-layer of corner sharing RuO_6 octahedra separated by a van der Waals gap.

Strontium atoms are located equal distances from both the inner apical (O1) and the outer apical (O2) oxygens to form a SrO halite layer along the *a-b* plane.[3] During the refinement, it was observed that the anisotropic atomic displacement parameter, U^{22}, for the equatorial oxygens (O3) was elongated in the *a-b* plane.[3] The ellipsoids representing the O3 atomic displacement parameters looked more prolated, or football-shaped, instead of an ideal sphere.[3] This observation was also noted in previous structure determinations of this compound and was resolved using a split occupancy method in their respective *I4*/*mmm* models.[5,23] The incorporation of this method into my model involved changing the Wyckoff position for O3 from 8*g* to 16*n* and refining a new *y* coordinate for the atomic position, which moves the equatorial oxygens away from the mirror plane. This split occupancy method doubles the number of symmetrically equivalent O3 positions (increase due to reflection of equivalent sites with the mirror plane), "decreases the occupancy of O3 position to 50%", and significantly reduces the U^{22} parameter (~75% reduction for X-ray diffraction data collected at 298 K).[3] The room temperature split occupancy O3 position refines to 0.23(2) Å away from the previous position on the mirror plane.[3] This corresponds to a RuO_6 octahedral rotation angle, Φ (**Figure 4.1b**), of 6.7(6)° and agrees with the findings of others from neutron powder diffraction experiments conducted at the same temperature.[5,23,25]

"However, [investigators] using neutron powder diffraction" fitted their data with models using either *Pban* (orthorhombic, No. 50)[5] or *Bbcb* (orthorhombic, No. 68)[23,25] space group.[3] The presence of weak superlattice reflections was cited as justification to redefine the unit cell by essentially rotating the unit cell by 45 degrees around the *c*-axis and expanding the lattice parameters *a* and *b* by a multiple of the square root of 2.[3] This unit cell conversion can be performed with the following transformation matrix: (1 -1 0, 1 1 0, 0 0 1).
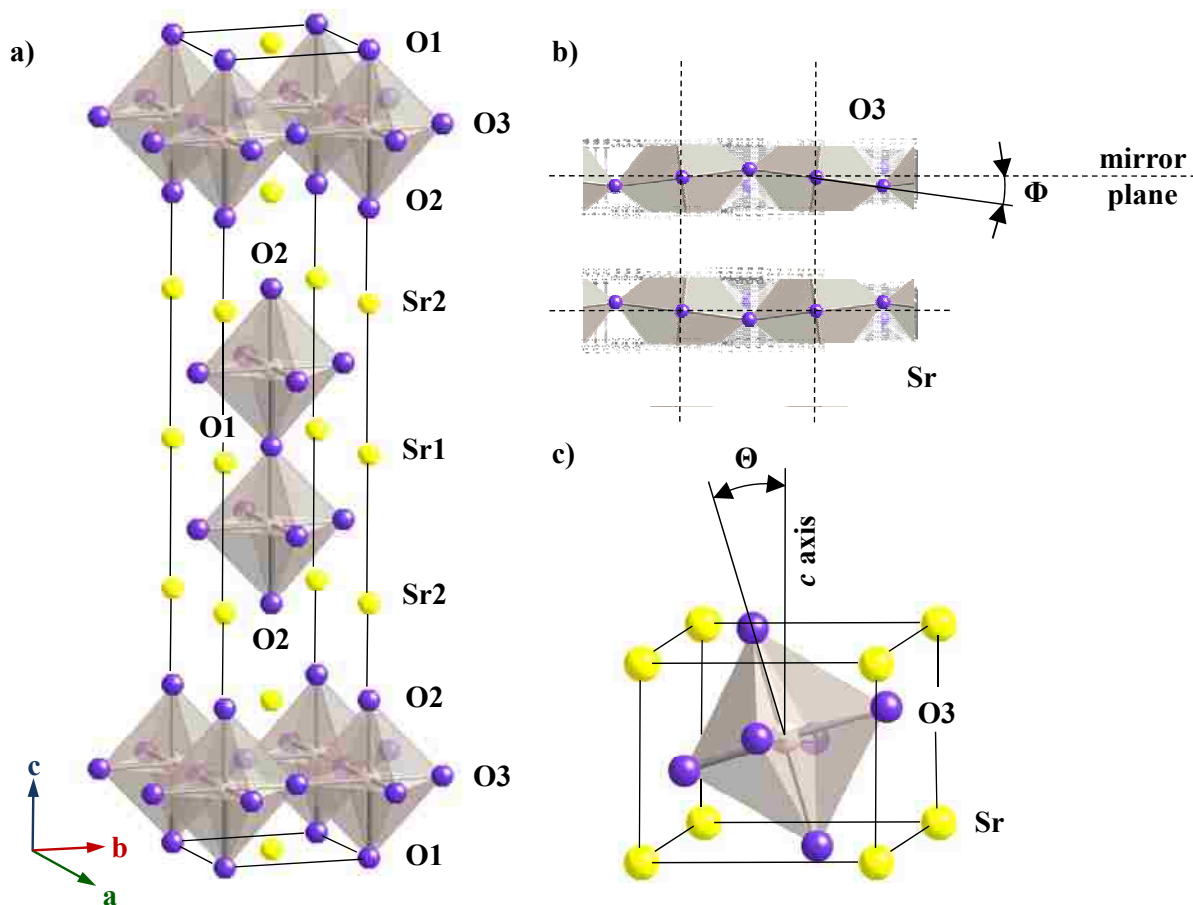
Figure 4.1. "(a) Unit cell representation of $Sr_3Ru_2O_7$ using tetragonal space group $I4/mmm$. The Ru atoms are located in the center of each octahedron. (b) Top view of the RuO_6 octahedra showing the rotation angle (Φ) in the ab plane (note: the dashed lines represent the location of mirror planes). (c) View of a RuO_6 octahedron showing a tilt angle (Θ). For the bulk, $\Theta = 0$ (see text)."[3]

In an effort to find the reflections that would warrant changing the tetragonal model to an orthorhombic model, three different $Sr_3Ru_2O_7$ single crystals of similar size were evaluated with longer (overnight) data collections. These weak reflections were not found, and led to the conclusion that the single crystal X-ray diffraction data was best modeled in the tetragonal space group $I4/mmm$ with the octahedral rotation refined with the split occupancy method.[3] No evidence could be obtained from the data to correlate how each layer of RuO_6 octahedra would rotate relative to each other within the bilayer. Room temperature $I4/mmm$ model of a $Sr_3Ru_2O_7$

50

single crystal with a mosaicity of 0.427(6)° resulted in a R_1 of 0.03 (demonstrating good agreement between the model and diffraction data), reasonable atomic displacement parameters (i.e., within an order of magnitude), and "low final difference map (less than 2 e$Å^{-3}$)."[3]

4.3.2 Cycling Temperature Dependence Study of $Sr_3Ru_2O_7$

Thermal cycle experiments with $Sr_3Ru_2O_7$ showed that unit cell size exhibits temperature dependence similar to a previous report (**Tables 4.1 - 4.3**).[24] When the temperature is lowered from 298 K to 90 K in the first cycle, the *a* lattice parameter decreased from 3.8897(10) Å to 3.8716(10) Å and the *c* lattice parameter increased from 20.732(6) Å to 20.798(8) Å. Examination of the Ru-O1 (inner apical oxygen) bond length reveals that interatomic bond distance becomes longer and changes from 2.0195(11) Å at room temperature to 2.0263 (10) Å at 90 K.[3] Over this temperature range, neither the "Ru-O2 (outer apical oxygen) nor the Ru-O3 (equatorial oxygen)" bond lengths change significantly.[3] Using Shannon's effective ionic radii[32] for six coordinate Ru^{4+} (0.620 Å) and O^{2-} (1.40 Å), the Ru-O bond lengths are expected to be around 2.02 Å at room temperature. Ru-O1 and Ru-O2 bond distances are in statistical agreement (i.e., within 3σ) of this prediction while Ru-O3 bond distance is slightly shorter than expected. There is also an indication of a small amount of buckling within the RuO_6 octahedra. A bond angle of 89.39(19)° is observed for O1-Ru-O3 while the O2-Ru-O3 is 90.61(19)°. As the temperature decreases from room temperature to 90 K, the buckling becomes smaller as the difference in the O1-Ru-O3 and O2-Ru-O3 bond angles become less. Octahedral rotation angle, Φ, of the equatorial oxygens, O3, is illustrated in **Figure 4.1b** looking down the *c*-axis (*i.e.*, top-view). The rotational angle of the RuO_6 octahedra increases (but not greater than 3σ) from "6.7(6)° at room temperature to 7.5(3)° at 200 K and 8.1(2)° at 90 K".[3]

It was observed in a thermal cycling experiment using neutron powder diffraction that the ratio of the lattice parameter *c* divided by the average of lattice parameters *a* and *b* increased

51

Table 4.1.   Crystallographic Parameters of $Sr_3Ru_2O_7$ (T = 298, 200, and 90 K)[3]

Crystal data

Temperature (K)	298	200	90
Crystal System	Tetragonal	Tetragonal	Tetragonal
Space group	*I4/mmm*	*I4/mmm*	*I4/mmm* (No. 139)
a (Å)	3.8897(10)	3.8800(15)	3.8716(10)
c (Å)	20.732(6)	20.767(7)	20.798(8)
V (Å^3)	313.66(15)	312.7(2)	311.75(15)
Z	2	2	2
2θ range (°)	7.8-54.8	7.8-54.8	7.8-54.6
μ (mm^{-1})	30.03	30.14	30.22

Data collection

Total reflections	363	360	345
Unique reflections	142	142	140
Reflections $I>2\sigma(I)$	139	139	138
[a]R_{int}	0.036	0.061	0.032
h	-5→5	-4→5	-5→5
k	-3→3	-4→5	-3→3
l	-26→23	-24→26	-24→26

Refinement

Reflections	142	142	140
Parameters	21	21	21
[b]$R_1[F^2>2\sigma(F^2)]$	0.029	0.034	0.032
[c]$wR_2(F^2)$	0.088	0.091	0.080
[d]S	1.31	1.25	1.24
$\Delta\rho_{max}$ (eÅ^{-3})	1.60	1.93	2.21
$\Delta\rho_{min}$ (eÅ^{-3})	-1.08	-1.74	-1.69

[a]$R_{int} = \Sigma \mid F_o^2 - F_o^2 \text{ (mean)} \mid / \Sigma [F_o^2]$

[b]$R_1 = \Sigma \mid\mid F_o \mid - \mid F_c \mid\mid / \Sigma \mid F_o \mid$

[c]$wR_2 = [\Sigma [w(F_o^2 - F_c^2)^2] / \Sigma [w(F_o^2)^2]]^{1/2}$ where $w = 1 / [\sigma^2(F_o^2) + (0.0495P)^2 + 0.6876P]$
for 298 K model, $w = 1 / [\sigma^2(F_o^2) + (0.0573P)^2 + 0.0000P]$ for 200 K model, and $w = 1 / [\sigma^2(F_o^2) + (0.0525P)^2 + 0.0172P]$ for 90 K model

[d]$S = [\Sigma [w(F_o^2 - F_c^2)^2] / (n - p)]^{1/2}$

Table 4.2. Atomic Positions and Equivalent Isotropic Displacement Parameters of $Sr_3Ru_2O_7$[3]

Atom	Wyckoff site	x	y	z	Occ.[a]	U_{eq} (Å^2)[b]
T = 298 K						
Sr1	2b	1/2	1/2	0	1	0.0071(6)
Sr2	4e	1/2	1/2	0.18626(9)	1	0.0070(6)
Ru1	4e	0	0	0.09741(5)	1	0.0034(6)
O1	2a	0	0	0	1	0.013(3)
O2	4e	0	0	0.1958(5)	1	0.013(2)
O3	16n	1/2	0.059(5)	0.0964(3)	0.5	0.013(5)
T = 200 K						
Sr1	2b	1/2	1/2	0	1	0.0050(6)
Sr2	4e	1/2	1/2	0.18634(8)	1	0.0049(6)
Ru1	4e	0	0	0.09740(5)	1	0.0023(6)
O1	2a	0	0	0	1	0.008(3)
O2	4e	0	0	0.1963(5)	1	0.0092(18)
O3	16n	1/2	0.066(3)	0.0967(2)	0.5	0.010(3)
T = 90 K						
Sr1	2b	1/2	1/2	0	1	0.0030(5)
Sr2	4e	1/2	1/2	0.18659(8)	1	0.0032(5)
Ru1	4e	0	0	0.09743(5)	1	0.0017(5)
O1	2a	0	0	0	1	0.005(2)
O2	4e	0	0	0.1958(5)	1	0.0062(16)
O3	16n	1/2	0.0707(18)	0.0969(2)	0.5	0.008(3)

[a] Occupancy
[b] U_{eq} is defined as one-third of the trace of the orthogonalized U^{ij} tensor.

during successive of thermal cycles.[24] These results were interpreted as strain in the material being relieved after each cycle.[3] To see if this behavior was reproducible, we carried out a similar experiment on our single crystals. All thirteen data sets were collected as described in experimental section and modeled in the tetragonal space group $I4/mmm$ with lattice parameters

Table 4.3.   Selected Interatomic Distances (Å) and Angles (°) of $Sr_3Ru_2O_7$[3]

Temperature (K)	298	200	90
Sr1-O1	2.75065(14)	2.7436(2)	2.73792(14)
Sr1-O3 (×4)	2.635(15)	2.621(7)	2.613(6)
Sr2-O2	2.7578(8)	2.7513(9)	2.7446(7)
Sr2-O3 (×4)	2.534(15)	2.512(8)	2.498(6)
Ru1-O1	2.0195(11)	2.0227(11)	2.0263(10)
Ru1-O2	2.040(10)	2.053(11)	2.046(9)
Ru1-O3 (×4)	1.958(3)	1.9566(13)	1.9553(10)
[a]Rotation angle	6.7(6)	7.5(3)	8.1(2)

[a] This value represents the rotational angle (Φ) for the RuO_6 octahedra. For a view of the rotational angles along the *ab*-plane, please see **Figure 4.1b**.

a ≈ 3.9 Å and c ≈ 20.8 Å. The refinement of this series of data collection was good with R_1 factors ranging from 3 to 4% and a Goodness of Fit (*S*) between 1.22 and 1.34.[3]

Because Shaked *et al.* used an enlarged orthorhombic unit cell, the lattice parameters *a* and *b* from these experiments were transformed by multiplying by the square root of 2 for direct comparison. **Figure 4.2a** shows the ratio *c/a* for thirteen data collections made during three back-to-back thermal cycles. An evaluation of the *c/a* ratio reveals that there is a significant difference between the three different temperatures (298 K, 200 K, and 90 K). However, analysis of the *c/a* ratio reveals that this ratio does not statistically change each time the cycle returns back to the same temperature for re-measurement. For instance, the *c/a* ratios are essentially the same for all of the 90 K data collections. Therefore, our single crystal X-ray diffraction data does not show significant difference from one thermal cycle to the next. A comparison of the room temperature X-ray diffraction results to previously published neutron powder diffraction results (**Figure 4.2b**).[24] Shaked and co-workers' *c/a* ratios are within the
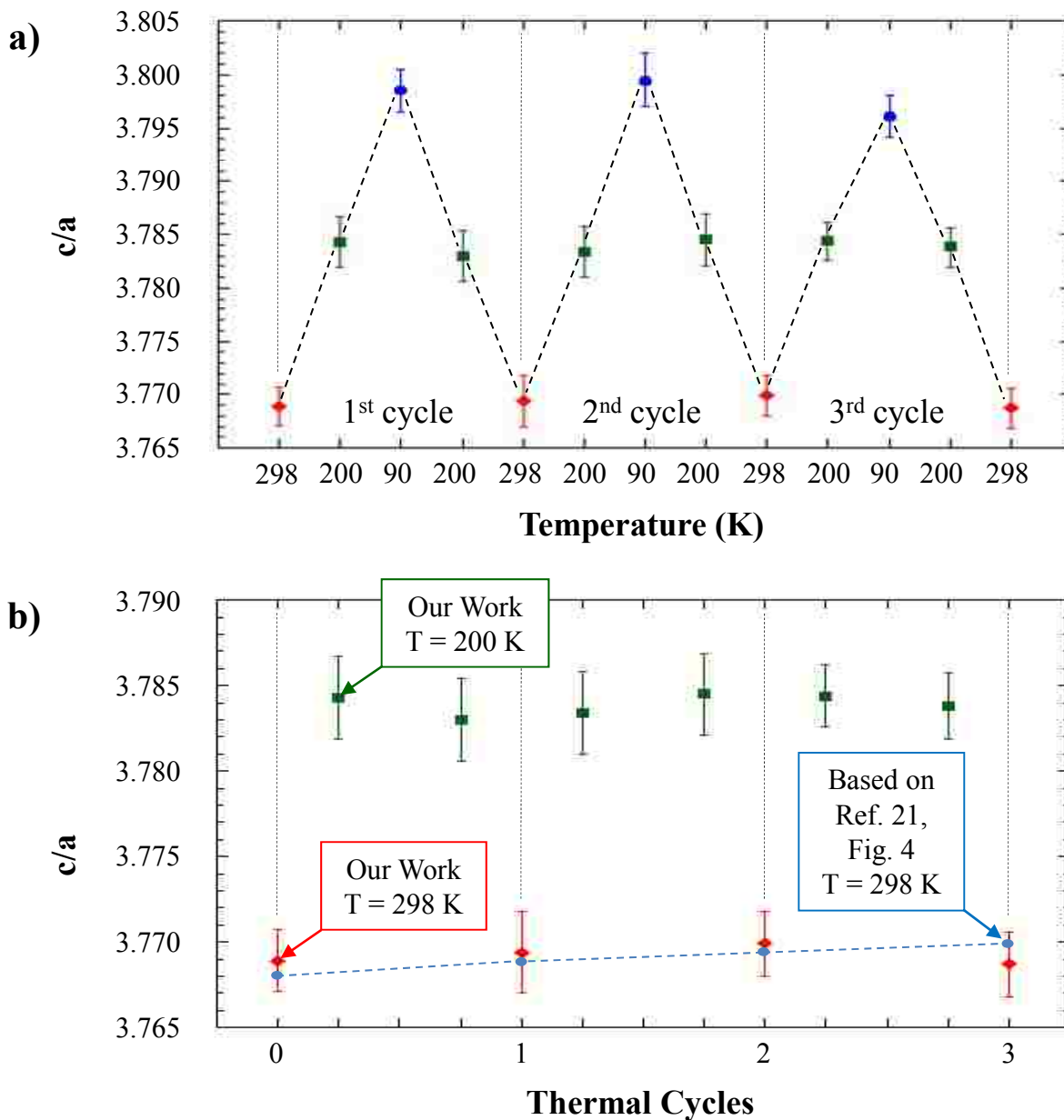
Figure 4.2. "(a) Temperature dependence of the cell parameter ratio c/a, from X-ray single-crystal diffraction data, in three thermal cycles. For comparison to previously reported c/a thermal-cycle data based on an orthorhombic unit cell, the tetragonal cell parameters a and b have been converted by multiplying by √2. The ratios are shown as filled red diamonds for 298 K, filled green squares for 200 K, and filled blue circles for 90 K. The diagonal dashed lines connecting the points are for guiding the eye only. The vertical dashed lines are used to separate three cycles. (b) Cell parameter ratio c/a versus thermal cycles at 298 K filled diamonds and 200 K filled squares. For comparison, previously reported c/a ratios from powder neutron diffraction see Ref. 21 are plotted filled circles connected with a dashed line. In both a) and b), the vertical dashed lines are used to separate three cycles."[3]

error bars of these measurements. However, it cannot be concluded that strain is being relieved through successive thermal cycles by evaluating the c/a ratios because the c/a ratios are not significantly changing.[3]

4.3.3   Mn-doping Effect on the Structure of $Sr_3Ru_2O_7$

The influence of chemical substitution on the $Sr_3Ru_2O_7$ structure was evaluated at six Mn-doping levels. Listed in **Tables 4.4 – 4.9** is the single crystal X-ray diffraction data collected at room temperature for the $Sr_3(Ru_{1-x}Mn_x)_2O_7$ series (x = 0.07, 0.09, 0.17, 0.20, 0.24, 0.33, 0.73). Diffraction data was also collected at 90 K (**Tables 4.10 – 4.15**) for each Mn concentration, x. For comparison purposes, room temperature lattice cell parameters, unit cell volume, and M-O (where M represents the Mn/Ru atomic site) bond lengths from papers published by Gallon *et al*. (x = 0.5)[33] and Mitchell *et al*. (x = 1)[34] are also included in the plots shown in **Figure 4.3**. It can be observed in **Figure 4.3a** that the lattice parameter c decreases at a more than the lattice a parameter for this series as the Mn concentration, x, is increased. Therefore, the compression on the c-axis has a larger influence than the contraction in the a-b plane on the steady decline in the unit cell volume (in **Figure 4.3b**).   In agreement with the trend observed with the lattice parameters, the apical M-O bonds in the direction of the c-axis are also getting shorter in a larger amount than the equatorial M-O bonds in the a-b plane.

As shown in **Figure 4.4a**, the bonds between the transition metal and the outer apical oxygens, O2, are longer than the bonds between the transition metal and the inner apical oxygens, O1, at the ruthenium end member (M-O1 bond length $\approx$ 2.02 Å and M-O2 bond length $\approx$ 2.04 Å for $Sr_3Ru_2O_7$). However, with increased doping with Mn, the M-O2 bond length becomes shorter than the M-O1 bond length at Mn concentrations above 50%. For $Sr_3Mn_2O_7$, Mitchell *et al*. reported that M-O1 bond length $\approx$ 1.95 Å and M-O2 bond length $\approx$ 1.91 Å. The

Table 4.4.   Crystallographic Parameters of $Sr_3(Ru_{1-x}Mn_x)_2O_7$ (T = 298 K)

Crystal data

x(refined)	0.066(8)	0.09(1)	0.17(1)	0.20(1)
Crystal system	Tetragonal	Tetragonal	Tetragonal	Tetragonal
Space group	*I4/mmm*	*I4/mmm*	*I4/mmm*	*I4/mmm*
a (Å)	3.8951(5)	3.898(2)	3.911(1)	3.916(1)
c (Å)	20.660(4)	20.603(5)	20.456(6)	20.366(7)
V (Å^3)	313.45(8)	313.1(3)	312.9(2)	312.3(2)
Mosaicity (°)	0.453(3)	0.474(4)	0.534(6)	0.503(5)
Z	2	2	2	2
2θ range (°)	8.0-59.8	7.9-60.0	8.0-59.9	8.0-60.0
μ (mm^{-1})	30.01	30.03	29.99	30.01
Size (mm^3)	0.05×0.07×0.10	0.02×0.08×0.08	0.02×0.06×0.08	0.01×0.08×0.08

Data collection

Total reflections	482	857	466	461
Unique reflections	177	177	176	176
Reflections $I>2\sigma(I)$	175	171	161	160
[b]R_{int}	0.017	0.079	0.062	0.033
h	-5→5	-5→5	-5→5	-5→5
k	-3→3	-5→5	-3→3	-3→3
l	-28→28	-28→27	-28→27	-28→24

Refinement

Reflections	177	177	176	176
Parameters	22	22	20	20
[c]$R_1[F^2>2\sigma(F^2)]$	0.027	0.027	0.048	0.036
[d]$wR_2(F^2)$	0.057	0.068	0.109	0.093
[e]S	1.27	1.19	1.18	1.22
$\Delta\rho_{max}$ (eÅ^{-3})	1.12	1.19	2.96	3.50
$\Delta\rho_{min}$ (eÅ^{-3})	-2.90	-1.83	-4.63	-2.61

[a]$R_{int} = \Sigma \mid F_o^2 - F_o^2 \text{ (mean)} \mid / \Sigma [F_o^2]$

[b]$R_1 = \Sigma \mid\mid F_o \mid - \mid F_c \mid\mid / \Sigma \mid F_o \mid$

[c]$wR_2 = [\Sigma [w(F_o^2 - F_c^2)^2] / \Sigma [w(F_o^2)^2]]^{1/2}$ where $w = 1 / [\sigma^2(F_o^2) + (0.0389P)^2 + 0.0000P]$ for $Sr_3(Ru_{0.93}Mn_{0.07})_2O_7$, $w = 1 / [\sigma^2(F_o^2) + (0.0338P)^2 + 1.0651P]$ for $Sr_3(Ru_{0.91}Mn_{0.09})_2O_7$, $w = 1 / [\sigma^2(F_o^2) + (0.0692P)^2 + 0.0000P]$ for $Sr_3(Ru_{0.83}Mn_{0.17})_2O_7$, $w = 1 / [\sigma^2(F_o^2) + (0.0582P)^2 + 0.6662P]$ for $Sr_3(Ru_{0.80}Mn_{0.20})_2O_7$

[d]$S = [\Sigma [w(F_o^2 - F_c^2)^2] / (n - p)]^{1/2}$

Table 4.5.   Crystallographic Parameters of $Sr_3(Ru_{1-x}Mn_x)_2O_7$ (T = 298 K)

Crystal data

x(refined)	0.242(8)	0.33(1)	0.73(2)
Crystal system	Tetragonal	Tetragonal	Tetragonal
Space group	*I4/mmm*	*I4/mmm*	*I4/mmm*
a (Å)	3.917(1)	3.914(2)	3.893(2)
c (Å)	20.315(5)	20.271(7)	20.096(6)
V (Å^3)	311.6(2)	310.5(2)	304.9(2)
Mosaicity (°)	0.436(4)	0.410(5)	0.794(6)
Z	2	2	2
2θ range (°)	8.0-59.6	8.0-59.7	8.1-59.9
μ (mm^{-1})	30.03	30.07	30.31
Size (mm^3)	0.01×0.05×0.07	0.01×0.01×0.13	0.02×0.10×0.12

Data collection

Total reflections	452	476	1402
Unique reflections	175	175	173
Reflections $I>2\sigma(I)$	150	159	166
[a]R_{int}	0.033	0.0473	0.1222
h	-5→5	-5→5	-5→5
k	-3→3	-3→3	-5→4
l	-24→28	-27→28	-28→28

Refinement

Reflections	175	175	173
Parameters	20	20	20
[b]$R_1[F^2>2\sigma(F^2)]$	0.026	0.0347	0.054
[c]$wR_2(F^2)$	0.063	0.1052	0.141
[d]S	1.09	1.156	1.12
$\Delta\rho_{max}$ (eÅ^{-3})	1.39	2.121	4.17
$\Delta\rho_{min}$ (eÅ^{-3})	-1.89	-1.438	-2.26

[a]$R_{int} = \Sigma \mid F_o^2 - F_o^2 \text{ (mean) } \mid / \Sigma [F_o^2]$

[b]$R_1 = \Sigma \mid\mid F_o \mid - \mid F_c \mid\mid / \Sigma \mid F_o \mid$

[c]$wR_2 = [\Sigma [w(F_o^2 - F_c^2)^2] / \Sigma [w(F_o^2)^2]]^{1/2}$ where $w = 1 / [\sigma^2(F_o^2) + (0.0391P)^2 + 0.0000P]$ for $Sr_3(Ru_{0.76}Mn_{0.24})_2O_7$, $w = 1 / [\sigma^2(F_o^2) + (0.0687P)^2 + 0.0000P]$ for $Sr_3(Ru_{0.67}Mn_{0.33})_2O_7$, $w = 1 / [\sigma^2(F_o^2) + (0.1136P)^2 + 0.0000P]$ for $Sr_3(Ru_{0.27}Mn_{0.73})_2O_7$

[d]$S = [\Sigma [w(F_o^2 - F_c^2)^2] / (n - p)]^{1/2}$

Table 4.6. Atomic Positions and Equivalent Isotropic Displacement Parameters of $Sr_3(Ru_{1-x}Mn_x)_2O_7$ (T = 298 K)

Atom	Wyckoff site	x	y	z	Occ.[a]	U_{eq} (Å²)[b]
$Sr_3(Ru_{0.93}Mn_{0.07})_2O_7$						
Sr1	2b	1/2	1/2	0	1	0.0094(3)
Sr2	4e	1/2	1/2	0.18593(4)	1	0.0089(3)
Mn1	4e	0	0	0.09739(3)	0.059(6)	0.0046(3)
Ru1	4e	0	0	0.09739(3)	0.941(6)	0.0046(3)
O1	2a	0	0	0	1	0.013(1)
O2	4e	0	0	0.1955(3)	1	0.0110(9)
O3	16n	1/2	0.056(2)	0.0966(2)	0.5	0.014(2)
$Sr_3(Ru_{0.91}Mn_{0.09})_2O_7$						
Sr1	2b	1/2	1/2	0	1	0.0090(4)
Sr2	4e	1/2	1/2	0.18561(5)	1	0.0083(4)
Mn1	4e	0	0	0.09736(3)	0.09(1)	0.0038(4)
Ru1	4e	0	0	0.09736(3)	0.91(1)	0.0038(4)
O1	2a	0	0	0	1	0.012(2)
O2	4e	0	0	0.1954(3)	1	0.011(1)
O3	16n	1/2	0.050(6)	0.0965(2)	0.5	0.013(4)
$Sr_3(Ru_{0.83}Mn_{0.17})_2O_7$						
Sr1	2b	1/2	1/2	0	1	0.0086(6)
Sr2	4e	1/2	1/2	0.18507(8)	1	0.0080(5)
Mn1	4e	0	0	0.09741(6)	0.17(1)	0.0040(6)
Ru1	4e	0	0	0.09741(6)	0.83(1)	0.0040(6)
O1	2a	0	0	0	1	0.012(3)
O2	4e	0	0	0.1960(5)	1	0.011(2)
O3	8g	1/2	0	0.0969(3)	1	0.019(2)
$Sr_3(Ru_{0.80}Mn_{0.20})_2O_7$						
Sr1	2b	1/2	1/2	0	1	0.0090(5)
Sr2	4e	1/2	1/2	0.18486(7)	1	0.0084(5)
Mn1	4e	0	0	0.09747(5)	0.20(1)	0.0039(5)
Ru1	4e	0	0	0.09747(5)	0.80(1)	0.0039(5)
O1	2a	0	0	0	1	0.014(3)
O2	4e	0	0	0.1955(4)	1	0.011(2)
O3	8g	1/2	0	0.0965(3)	1	0.016(1)

[a]Occupancy

[b]U_{eq} is defined as one-third of the trace of the orthogonalized U^{ij} tensor.

Table 4.7. Atomic Positions and Equivalent Isotropic Displacement Parameters of $Sr_3(Ru_{1-x}Mn_x)_2O_7$ (T = 298 K)

Atom	Wyckoff site	x	y	z	Occ.[a]	U_{eq} (Å²)[b]
$Sr_3(Ru_{0.76}Mn_{0.24})_2O_7$						
Sr1	2b	1/2	1/2	0	1	0.0110(4)
Sr2	4e	1/2	1/2	0.18456(5)	1	0.0104(3)
Mn1	4e	0	0	0.09745(4)	0.242(8)	0.0061(3)
Ru1	4e	0	0	0.09745(4)	0.758(8)	0.0061(3)
O1	2a	0	0	0	1	0.014(2)
O2	4e	0	0	0.1953(3)	1	0.015(2)
O3	8g	1/2	0	0.0966(2)	1	0.017(1)
$Sr_3(Ru_{0.67}Mn_{0.33})_2O_7$						
Sr1	2b	1/2	1/2	0	1	0.0110(6)
Sr2	4e	1/2	1/2	0.18428(8)	1	0.0098(5)
Mn1	4e	0	0	0.09730(7)	0.33(1)	0.0054(5)
Ru1	4e	0	0	0.09730(7)	0.67(1)	0.0054(5)
O1	2a	0	0	0	1	0.013(3)
O2	4e	0	0	0.1953(5)	1	0.012(2)
O3	8g	1/2	0	0.0967(3)	1	0.013(2)
$Sr_3(Ru_{0.27}Mn_{0.73})_2O_7$						
Sr1	2b	1/2	1/2	0	1	0.0112(7)
Sr2	4e	1/2	1/2	0.18345(6)	1	0.0100(6)
Mn1	4e	0	0	0.09717(9)	0.73(2)	0.0036(9)
Ru1	4e	0	0	0.09717(9)	0.27(2)	0.0036(9)
O1	2a	0	0	0	1	0.011(3)
O2	4e	0	0	0.1935(6)	1	0.011(2)
O3	8g	1/2	0	0.0961(3)	1	0.008(1)

[a]Occupancy
[b]U_{eq} is defined as one-third of the trace of the orthogonalized U^{ij} tensor.

Table 4.8. Selected Interatomic Distances (Å) and Angles (°) of $Sr_3(Ru_{1-x}Mn_x)_2O_7$ at T = 298 K

x(refined)	0.066(8)	0.09(1)	0.17(1)	0.20(1)
Distances				
Sr1-O1	2.7543(4)	2.7563(3)	2.7650(1)	2.7690(7)
Sr1-O3 (×4)	2.640(5)	2.65(2)	2.784(5)	2.774(5)
Sr2-O2	2.450(6)	2.452(7)	2.43(1)	2.437(9)
Sr2-O2	2.7613(5)	2.7637(6)	2.7745(9)	2.777(1)
Sr2-O3 (×4)	2.530(6)	2.54(2)	2.661(5)	2.659(4)
Ru1-O1	2.0120(7)	2.0059(7)	1.993(1)	1.985(1)
Ru1-O2	2.026(5)	2.020(7)	2.02(1)	1.997(9)
Ru1-O3 (×4)	1.9598(9)	1.959(2)	1.9554(1)	1.9580(5)
Angles				
O1-Ru1-O3 (×4)	89.49(9)	89.5(1)	89.7(2)	89.4(2)
O2-Ru1-O3 (×4)	90.51(9)	90.5(1)	90.3(2)	90.6(2)
Rotation				
[a]RuO_6 octahedra	6.4(2)	5.7(7)	n/a	n/a

[a] This value represents the rotational angle (Φ) for the RuO_6 octahedra. For a view of the rotational angles along the *ab*-plane, please see **Figure 4.1b**.

M-O3 bond lengths (in **Figure 4.4b**) show little variability (between 1.95 Å to 1.96 Å) until the Mn-concentration, *x*, is greater than 0.73 in this series.

While the oxidation state of ruthenium is +4 for the ruthenium end-member, $Sr_3Ru_2O_7$, and the oxidation state of manganese is +4 for the manganese end-member, $Sr_3Mn_2O_7$, it is not clear in the literature what happens to the oxidation states in between the two end-members. Sikora *et al*. reported[35] the oxidation states for a 50% Mn-doped sample (*i.e.*, Sr_3MnRuO_7) using

Table 4.9. Selected Interatomic Distances (Å) and Angles (°) of $Sr_3(Ru_{1-x}Mn_x)_2O_7$ at T = 298 K

x(refined)	0.242(8)	0.33(1)	0.73(2)
Distances			
Sr1-O1	2.7697(1)	2.7676(2)	2.7542(2)
Sr1-O3 (×4)	2.772(3)	2.769(5)	2.742(4)
Sr2-O2	2.440(7)	2.44(1)	2.47(1)
Sr2-O2	2.7784(6)	2.7766(9)	2.7615(9)
Sr2-O3 (×4)	2.651(3)	2.643(5)	2.622(4)
Ru1-O1	1.9797(8)	1.972(1)	1.953(2)
Ru1-O2	1.989(7)	1.99(1)	1.94(1)
Ru1-O3 (×4)	1.9586(1)	1.9571(2)	1.9476(2)
Angles			
O1-Ru1-O3 (×4)	89.5(1)	89.6(2)	89.4(2)
O2-Ru1-O3 (×4)	90.5(1)	90.4(2)	90.6(2)
Rotation			
[a]RuO_6 octahedra	n/a	n/a	n/a

[a] This value represents the rotational angle (Φ) for the RuO_6 octahedra. For a view of the rotational angles along the *ab*-plane, please see **Figure 4.1b**.

X-ray Absorption Near Edge Structure (XANES) and the following oxidation state standards: Mn_2O_3 (for Mn^{3+}), $MnO_{1.9}$ (for Mn^{4+}), La_2NiRuO_6 (for Ru^{4+}), and Ba_2LaRuO_6 (for Ru^{5+}). Based on the fits of the data, the average oxidation states of each transition metal was determined to be $Mn^{3.42(5)+}$ and $Ru^{4.6(2)+}$. This suggests that not only is there a mixture of Mn^{3+} and Mn^{4+}, but also a mixture of Ru^{4+} and Ru^{5+}.

Table 4.10. Crystallographic Parameters of $Sr_3(Ru_{1-x}Mn_x)_2O_7$ (T = 90 K)[a]

x(refined)	0.066(8)	0.08(1)	0.16(2)	0.20(1)
Crystal system	Tetragonal	Tetragonal	Tetragonal	Tetragonal
Space group	$I4/mmm$	$I4/mmm$	$I4/mmm$	$I4/mmm$
a (Å)	3.8778(5)	3.883(4)	3.899(2)	3.905(1)
c (Å)	20.733(4)	20.658(1)	20.476(7)	20.365(8)
V (Å^3)	311.77(8)	311.5(3)	311.2(2)	310.5(2)
Mosaicity (°)	0.460(3)	0.593(3)	0.738(7)	0.536(5)
Z	2	2	2	2
2θ range (°)	7.8-60.2	7.9-60.0	8.0-60.0	8.0-59.7
μ (mm^{-1})	30.17	30.19	30.14	30.179
Size (mm^3)	0.05×0.07×0.10	0.02×0.08×0.08	0.02×0.06×0.08	0.01×0.08×0.08
Data collection				
Total reflections	480	1678	461	439
Unique reflections	177	177	176	175
Reflections $I>2\sigma(I)$	177	171	155	155
[b]R_{int}	0.021	0.103	0.054	0.033
h	-5→5	-5→5	-5→5	-5→5
k	-3→3	-5→5	-3→3	-3→3
l	-28→28	-26→28	-25→28	-24→28
Refinement				
Reflections	177	177	176	175
Parameters	22	22	22	20
[c]$R_1[F^2>2\sigma(F^2)]$	0.025	0.032	0.041	0.033
[d]$wR_2(F^2)$	0.058	0.092	0.114	0.071
[e]S	1.27	1.26	1.13	1.10
$\Delta\rho_{max}$ (eÅ^{-3})	1.24	1.62	2.17	2.59
$\Delta\rho_{min}$ (eÅ^{-3})	-2.14	-1.75	-3.69	-2.56

[a]T = 91 K for $Sr_3(Ru_{0.93}Mn_{0.07})_2O_7$

[b]$R_{int} = \Sigma \mid F_o^2 - F_o^2 \text{ (mean)} \mid / \Sigma [F_o^2]$

[c]$R_1 = \Sigma \mid\mid F_o \mid - \mid F_c \mid\mid / \Sigma \mid F_o \mid$

[d]$wR_2 = [\Sigma [w(F_o^2 - F_c^2)^2] / \Sigma [w(F_o^2)^2]]^{1/2}$ where $w = 1 / [\sigma^2(F_o^2) + (0.0365P)^2 + 0.4462P]$ for $Sr_3(Ru_{0.93}Mn_{0.07})_2O_7$, $w = 1 / [\sigma^2(F_o^2) + (0.0535P)^2 + 0.7793P]$ for $Sr_3(Ru_{0.92}Mn_{0.08})_2O_7$, $w = 1 / [\sigma^2(F_o^2) + (0.0790P)^2 + 0.0000P]$ for $Sr_3(Ru_{0.84}Mn_{0.16})_2O_7$, $w = 1 / [\sigma^2(F_o^2) + (0.0477P)^2 + 0.0000P]$ for $Sr_3(Ru_{0.80}Mn_{0.20})_2O_7$

[e]$S = [\Sigma [w(F_o^2 - F_c^2)^2] / (n - p)]^{1/2}$

Table 4.11.   Crystallographic Parameters of $Sr_3(Ru_{1-x}Mn_x)_2O_7$ (T = 90 K)[a]

x(refined)	0.25(1)	0.331(9)	0.68(2)
Crystal system	Tetragonal	Tetragonal	Tetragonal
Space group	*I4/mmm*	*I4/mmm*	*I4/mmm*
a (Å)	3.908(1)	3.904(1)	3.889(1)
c (Å)	20.291(5)	20.252(6)	20.064(6)
V (Å^3)	309.9(1)	308.7(2)	303.5(2)
Mosaicity (°)	0.473(3)	0.573(5)	0.950(5)
Z	2	2	2
2θ range (°)	8.0-59.6	8.0-59.9	8.1-60.0
μ (mm^{-1})	30.21	30.26	30.49
Size (mm^3)	0.01×0.05×0.07	0.01×0.01×0.13	0.02×0.10×0.12
Data collection			
Total reflections	477	438	472
Unique reflections	175	175	174
Reflections $I>2\sigma(I)$	153	164	166
[b]R_{int}	0.031	0.0371	0.0544
h	-5→5	-5→5	-5→5
k	-3→3	-3→3	-3→3
l	-28→28	-22→28	-28→28
Refinement			
Reflections	175	175	174
Parameters	20	20	20
[c]$R_1[F^2>2\sigma(F^2)]$	0.024	0.031	0.048
[d]$wR_2(F^2)$	0.059	0.088	0.143
[e]S	1.17	1.22	1.17
$\Delta\rho_{max}$ (eÅ^{-3})	2.01	2.00	2.32
$\Delta\rho_{min}$ (eÅ^{-3})	-1.51	-1.40	-2.01

[a]T = 92 K for $Sr_3(Ru_{0.75}Mn_{0.25})_2O_7$

[b]$R_{int} = \Sigma \, | \, F_o^2 - F_o^2 \text{ (mean)} \, | \, / \, \Sigma \, [\, F_o^2 \,]$

[c]$R_1 = \Sigma \, | \, | \, F_o \, | - | \, F_c \, | \, | \, / \, \Sigma \, | \, F_o \, |$

[d]$wR_2 = [\, \Sigma \, [\, w(\, F_o^2 - F_c^2 \,)^2 \,] \, / \, \Sigma \, [\, w(\, F_o^2 \,)^2 \,] \,]^{1/2}$ where $w = 1 \, / \, [\, \sigma^2(F_o^2) + (0.0272P)^2 + 2.4491P \,]$ for $Sr_3(Ru_{0.75}Mn_{0.25})_2O_7$, $w = 1 \, / \, [\, \sigma^2(F_o^2) + (0.0568P)^2 + 0.3702P \,]$ for $Sr_3(Ru_{0.67}Mn_{0.33})_2O_7$, $w = 1 \, / \, [\, \sigma^2(F_o^2) + (0.1093P)^2 + 0.0000P \,]$ for $Sr_3(Ru_{0.32}Mn_{0.68})_2O_7$

[e]$S = [\, \Sigma \, [\, w(\, F_o^2 - F_c^2 \,)^2 \,] \, / \, (n-p) \,]^{1/2}$

Table 4.12. Atomic Positions and Equivalent Isotropic Displacement Parameters of $Sr_3(Ru_{1-x}Mn_x)_2O_7$ (T = 90 K)[a]

Atom	Wyckoff site	x	y	z	Occ.[b]	U_{eq} (Å^2)[c]
$Sr_3(Ru_{0.93}Mn_{0.07})_2O_7$						
Sr1	2b	1/2	1/2	0	1	0.0047(3)
Sr2	4e	1/2	1/2	0.18635(4)	1	0.0046(3)
Mn1	4e	0	0	0.09740(3)	0.066(8)	0.0023(3)
Ru1	4e	0	0	0.09740(3)	0.934(8)	0.0023(3)
O1	2a	0	0	0	1	0.007(1)
O2	4e	0	0	0.1954(3)	1	0.0074(9)
O3	16n	1/2	0.066(1)	0.0966(1)	0.5	0.008(1)
$Sr_3(Ru_{0.92}Mn_{0.08})_2O_7$						
Sr1	2b	1/2	1/2	0	1	0.0053(5)
Sr2	4e	1/2	1/2	0.18607(6)	1	0.0053(4)
Mn1	4e	0	0	0.09733(5)	0.08(1)	0.0034(5)
Ru1	4e	0	0	0.09733(5)	0.92(1)	0.0034(5)
O1	2a	0	0	0	1	0.008(2)
O2	4e	0	0	0.1950(5)	1	0.008(2)
O3	16n	1/2	0.064(2)	0.0966(3)	0.5	0.008(2)
$Sr_3(Ru_{0.84}Mn_{0.16})_2O_7$						
Sr1	2b	1/2	1/2	0	1	0.0059(6)
Sr2	4e	1/2	1/2	0.18508(8)	1	0.0054(6)
Mn1	4e	0	0	0.09726(6)	0.16(2)	0.0036(6)
Ru1	4e	0	0	0.09726(6)	0.84(2)	0.0036(6)
O1	2a	0	0	0	1	0.010(3)
O2	4e	0	0	0.1951(6)	1	0.011(2)
O3	16n	1/2	0.051(6)	0.0965(4)	0.5	0.006(5)
$Sr_3(Ru_{0.80}Mn_{0.20})_2O_7$						
Sr1	2b	1/2	1/2	0	1	0.0045(4)
Sr2	4e	1/2	1/2	0.18493(6)	1	0.0042(4)
Mn1	4e	0	0	0.09746(4)	0.20(1)	0.0019(4)
Ru1	4e	0	0	0.09746(4)	0.80(1)	0.0019(4)
O1	2a	0	0	0	1	0.006(2)
O2	4e	0	0	0.1950(4)	1	0.009(2)
O3	8g	1/2	0	0.0960(2)	1	0.013(1)

[a]T = 91 K for $Sr_3(Ru_{0.93}Mn_{0.07})_2O_7$

[b]Occupancy

[c]U_{eq} is defined as one-third of the trace of the orthogonalized U^{ij} tensor.

Table 4.13. Atomic Positions and Equivalent Isotropic Displacement Parameters of $Sr_3(Ru_{1-x}Mn_x)_2O_7$ (T = 90 K)[a]

Atom	Wyckoff site	x	y	z	Occ.[b]	U_{eq} (Å^2)[c]
$Sr_3(Ru_{0.75}Mn_{0.25})_2O_7$						
Sr1	2b	1/2	1/2	0	1	0.0064(4)
Sr2	4e	1/2	1/2	0.18449(5)	1	0.0061(3)
Mn1	4e	0	0	0.09741(4)	0.25(1)	0.0038(4)
Ru1	4e	0	0	0.09741(4)	0.75(1)	0.0038(4)
O1	2a	0	0	0	1	0.010(2)
O2	4e	0	0	0.1953(3)	1	0.011(2)
O3	8g	1/2	0	0.0965(2)	1	0.010(1)
$Sr_3(Ru_{0.67}Mn_{0.33})_2O_7$						
Sr1	2b	1/2	1/2	0	1	0.0060(5)
Sr2	4e	1/2	1/2	0.18423(6)	1	0.0049(4)
Mn1	4e	0	0	0.09739(6)	0.331(9)	0.0028(5)
Ru1	4e	0	0	0.09739(6)	0.669(9)	0.0028(5)
O1	2a	0	0	0	1	0.008(2)
O2	4e	0	0	0.1958(4)	1	0.007(2)
O3	8g	1/2	0	0.0965(3)	1	0.009(1)
$Sr_3(Ru_{0.32}Mn_{0.68})_2O_7$						
Sr1	2b	1/2	1/2	0	1	0.0067(7)
Sr2	4e	1/2	1/2	0.18340(7)	1	0.0062(6)
Mn1	4e	0	0	0.09705(9)	0.68(2)	0.0030(9)
Ru1	4e	0	0	0.09705(9)	0.32(2)	0.0030(9)
O1	2a	0	0	0	1	0.007(3)
O2	4e	0	0	0.1942(7)	1	0.007(2)
O3	8g	1/2	0	0.0959(3)	1	0.006(1)

[a]T = 92 K for $Sr_3(Ru_{0.75}Mn_{0.25})_2O_7$

[b]Occupancy

[c]U_{eq} is defined as one-third of the trace of the orthogonalized U^{ij} tensor.

Table 4.14. Selected Interatomic Distances (Å) and Angles (°) of $Sr_3(Ru_{1-x}Mn_x)_2O_7$ at T = 90 K[a]

x(refined)	0.066(8)	0.08(1)	0.16(2)	0.20(1)
Distances				
Sr1-O1	2.7420(4)	2.7457(3)	2.7570(2)	2.7612(7)
Sr1-O3 (×4)	2.615(4)	2.617(7)	2.641(17)	2.762(3)
Sr2-O2	2.453(6)	2.458(9)	2.45(1)	2.444(8)
Sr2-O2	2.7484(5)	2.7518(7)	2.7646(9)	2.7688(9)
Sr2-O3 (×4)	2.509(4)	2.508(7)	2.52(2)	2.664(3)
Ru1-O1	2.0193(7)	2.011(1)	1.992(1)	1.985(1)
Ru1-O2	2.031(6)	2.017(9)	2.00(1)	1.987(8)
Ru1-O3 (×4)	1.9559(7)	1.957(1)	1.960(2)	1.9527(5)
Angles				
O1-Ru1-O3 (×4)	89.51(9)	89.5(2)	89.6(3)	89.1(2)
O2-Ru1-O3 (×4)	90.49(9)	90.5(2)	90.4(3)	90.9(2)
Rotation				
[b]RuO_6 octahedra	7.5(2)	7.3(3)	5.8(7)	n/a

[a]T = 91 K for $Sr_3(Ru_{0.93}Mn_{0.07})_2O_7$

[b]This value represents the rotational angle (Φ) for the RuO_6 octahedra. For a view of the rotational angles along the *ab*-plane, please see **Figure 4.1b**.

Hossain *et al*. examined[36] a 10% Mn-doped $Sr_3Ru_2O_7$ sample using X-ray Absorption Spectroscopy (XAS). A comparison of the sample's spectra was made to the following oxidation standards: MnO (for Mn^{2+}), $LaMnO_3$ (for Mn^{3+}), and $Sr_3Mn_2O_7$ (for Mn^{4+}). XAS data shows good agreement with the Mn^{3+} standard, demonstrating that Mn in low concentration is only in the +3 oxidation state. Unfortunately, no evaluation of the Ru oxidation state was conducted in this study. More recently, Guo *et al*. explored the Ru oxidation state changes in

Table 4.15. Selected Interatomic Distances (Å) and Angles (°) of $Sr_3(Ru_{1-x}Mn_x)_2O_7$ at T = 90 K[a]

x(refined)	0.25(1)	0.331(9)	0.68(2)
Distances			
Sr1-O1	2.7633(7)	2.7606(7)	2.7499(1)
Sr1-O3 (×4)	2.766(3)	2.762(4)	2.736(4)
Sr2-O2	2.440(7)	2.429(9)	2.46(1)
Sr2-O2	2.7719(9)	2.771(1)	2.758(1)
Sr2-O3 (×4)	2.647(3)	2.640(4)	2.620(4)
Ru1-O1	1.977(1)	1.972(1)	1.947(2)
Ru1-O2	1.985(7)	1.994(8)	1.95(1)
Ru1-O3 (×4)	1.9540(5)	1.9521(5)	1.9446(1)
Angles			
O1-Ru1-O3 (×4)	89.5(1)	89.5(2)	89.3(2)
O2-Ru1-O3 (×4)	90.5(1)	90.5(2)	90.7(2)
Rotation			
[b]RuO_6 octahedra	n/a	n/a	n/a

[a]T = 92 K for $Sr_3(Ru_{0.75}Mn_{0.25})_2O_7$

[b]This value represents the rotational angle (Φ) for the RuO_6 octahedra. For a view of the rotational angles along the *ab*-plane, please see **Figure 4.1b**.

10% and 20% Mn-doped $Sr_3Ru_2O_7$ samples relative to the ruthenium end-member, $Sr_3Ru_2O_7$, using X-ray Photoelectron Spectroscopy (XPS) on single bilayer surfaces cleaved from single crystals. Their studies show that low concentrations of "Mn-doping do not change the Ru oxidation state".[3] The Mn oxidation state could not be evaluated due to the low intensity of the Mn XPS signal.[37]
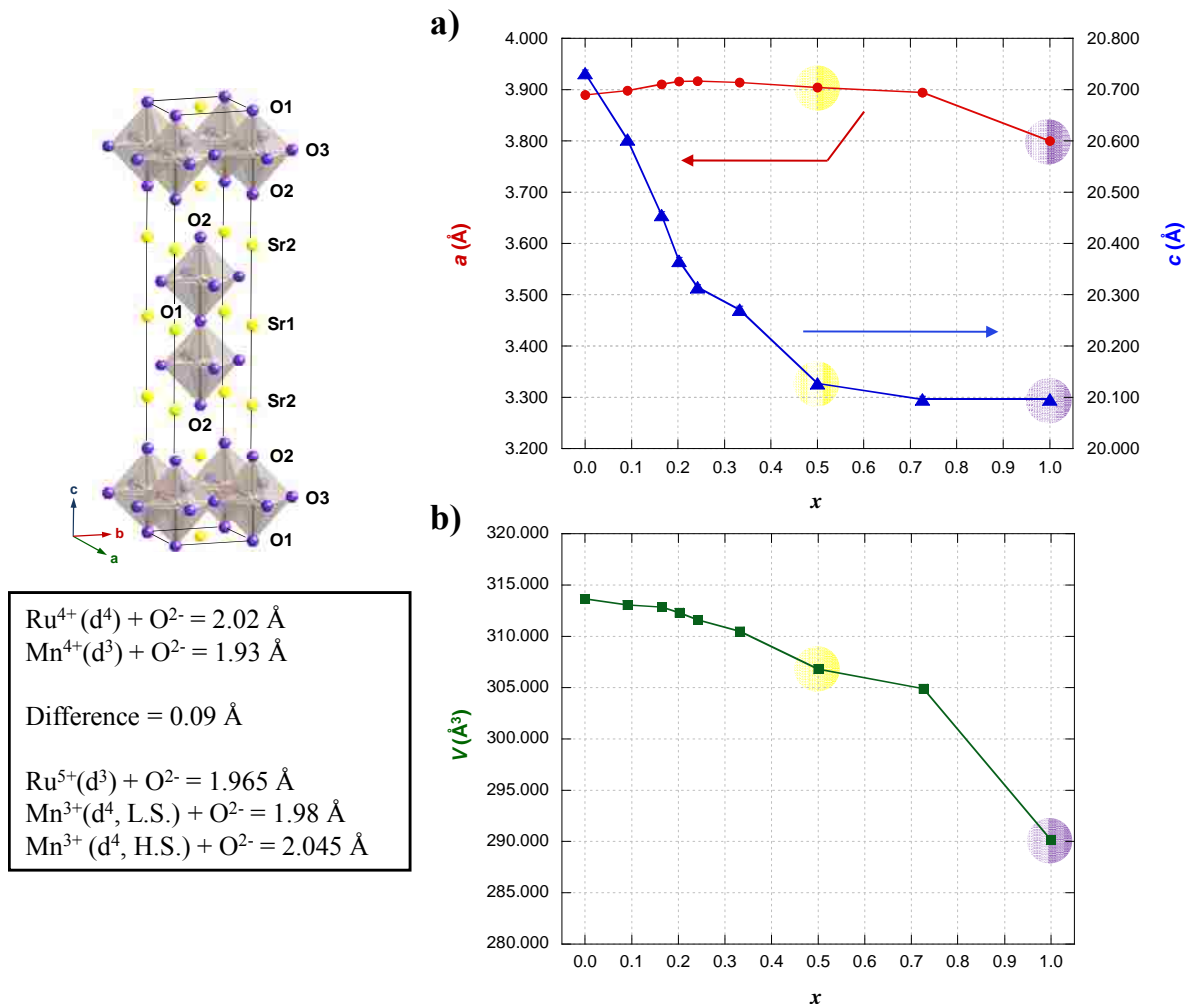
Figure 4.3. (a) Lattice parameter a, solid red circles, and c, solid blue triangles, (b) unit cell volume V, solid green squares, for the $Sr_3(Ru_{1-x}Mn_x)_2O_7$ series at room temperature as a function of refined value of x. Crystallographic data highlighted in yellow is from Reference 32 and in purple is from Reference 33.

Evaluating bond lengths determined by single crystal X-ray diffraction generally represents a good method of elucidating oxidation states. Using Shannon's effective ionic radii[32] for a six coordinate transition metal to oxygen bond, the possible bond lengths are the following:

Ru^{5+} (0.565 Å) + O^{2-} (1.40 Å) = 1.965 Å Mn^{3+}, L.S. (0.58 Å) + O^{2-} (1.40 Å) = 1.98 Å

Ru^{4+} (0.620 Å) + O^{2-} (1.40 Å) = 2.02 Å Mn^{3+}, H.S. (0.65 Å) + O^{2-} (1.40 Å) = 2.05 Å

Mn^{4+} (0.530 Å) + O^{2-} (1.40 Å) = 1.93 Å

a)   b)

O2 (outer apical)

O3   Ru1

O3   O3   O3 (equatorial)

O3

O1 (inner apical)

O3   Ru1

O3   O3

O3

O2
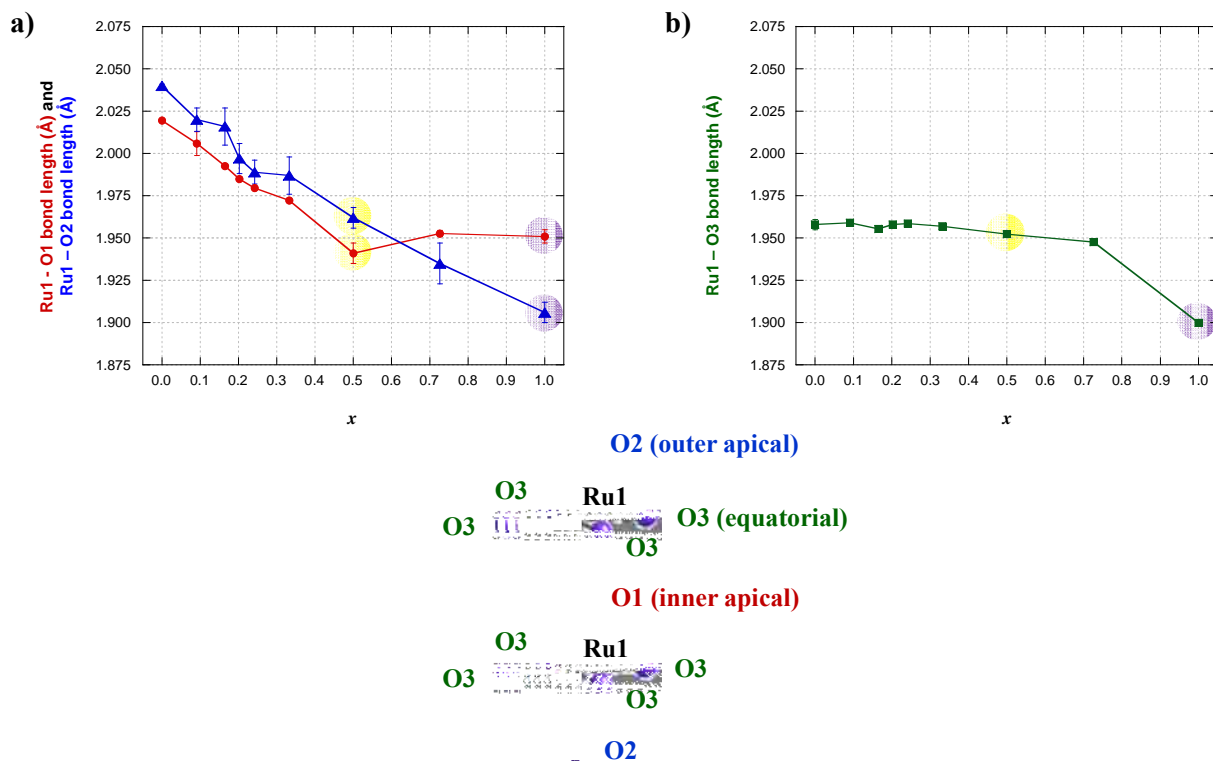
Figure 4.4.   As a function of refined value of *x* are the octahedral bond lengths (a) Ru1-O1, solid red circles; Ru1-O2, solid blue triangles; and (c) Ru1-O3, solid green squares. The three different oxygens are the inner apical (O1), the outer apical (O2) and the equatorial (O3) oxygens. Crystallographic data highlighted in yellow is from Reference 32 and in purple is from Reference 33.

The average of the six M-O bond lengths is approximately 1.91 Å for $Sr_3Mn_2O_7$ based on the data reported by Mitchell *et al.*[34] This agrees with the predicted with Mn^{4+} oxidation state. For $Sr_3Ru_2O_7$, the average Ru to apical oxygen bonds is about 2.03 Å in length and suggests a Ru^{4+} oxidation state. However, the Ru to equatorial oxygen bonds are shorter than anticipated for Ru^{4+} with a length around 1.96 Å. This indicates that the RuO_6 octahedra are distorted with a contraction in the *a-b* plane for the ruthenium end-member. For Sr_3MnRuO_7, the average M–O bonds is close to 1.95 Å.[33] In the XANES results (Szczerba *et al.*),[35] it can be inferred from the average oxidation states, $Mn^{3.42(5)+}$ and $Ru^{4.6(2)+}$, that the ratio of Mn^{3+} / Mn^{4+} is 0.58 / 0.42, the

ratio of Ru^{5+} / Ru^{4+} is 0.60 / 0.40, and calculated M-O bond length should be 1.99 Å (assuming Mn^{3+} is high spin) and 1.97 Å (assuming Mn^{3+} is low spin). This suggests that Mn^{3+} is low spin for this complex. However, it does not support, nor contradict, the mixed oxidation results of both transition metals (Mn and Ru). Bond lengths calculated using Mn^{4+} and Ru^{4+} result in 1.98 Å. Therefore, the transition metal oxidation states for this series of compounds cannot be determined conclusively by analysis of the bond lengths.[19]

In light of all the structural and physical properties, it becomes clear that the variation of electronic and magnetic properties is intimately connected with the change of the local structure of $Sr_3(Ru_{1-x}Mn_x)_2O_7$, even though the global structure symmetry remains unchanged. Due to the partial replacement of Ru by Mn with a smaller ionic radius, the unit cell becomes smaller and (Ru/Mn)O_6 becomes less distorted. This feature is reflected in both rotation angle (see **Figure 4.1a**) and ratio between axial bond lengths and equatorial bond lengths. This weakens the ferromagnetic (FM) interaction, according to the theoretical calculations for the single-layered ruthenate $Ca_{2-x}Sr_xRuO_4$,[13] and leads to long-range antiferromagnetic (AFM) ordering. When the Mn doping concentration, x, is greater than 0.16, the (Ru/Mn)O_6 octahedra are no longer rotated (see **Figure 4.1a**).[19] This gives rise to competitive AFM and FM interactions and the system can no longer form long-range magnetic ordering. On the other hand, the increase of the metal-insulator transition temperature, T_{MIT}, with x is not surprising, as $3d$-Mn is more localized than $4d$-Ru.

4.3.4   Phase Purity Determined by Single and Powder X-ray Diffraction (3-2-7 vs. 4-3-10)

While screening the batches of Mn-doped $Sr_3Ru_2O_7$ for well diffracting single crystals, two of the batches (when the refined 3-2-7 phase of Mn-concentration, x, is 0.20 and 0.24) had crystals with the same a and b lattice parameters (~3.9 Å) as expected for the 3-2-7 phase at room temperature. However, there were some crystals that had a noticeably longer c-axis of

~28.3 Å (which is 8 Å longer). A literature review showed that the larger unit cell matched for the 4-3-10 phase[38] (**Figure 4.5**) of the Ruddlesden-Popper series, $Sr_{n+1}Ru_nO_{3n+1}$ (n = 1, 2, 3, … ∞).[1,2] In both of the Mn-concentrations (x = 0.20 and 0.24), the occupancy of transition metal, M, atomic sites had a higher Mn % for the two outer corner-sharing MO_6 octahedral layers than the inner layer.

Ruddlesden-Popper series, $Sr_{n+1}Ru_nO_{3n+1}$ (n = 1, 2, 3, … ∞)

Bi-layer

Tri-layer

$Sr_3(Ru_{0.80}Mn_{0.20})_2O_7$
a = 3.9159(10) Å
c = 20.366(7) Å
n = 2

$Sr_4(Ru_{0.79}Mn_{0.21})_3O_{10}$
a = 3.9097(10) Å
c = 28.288(4) Å
n = 3
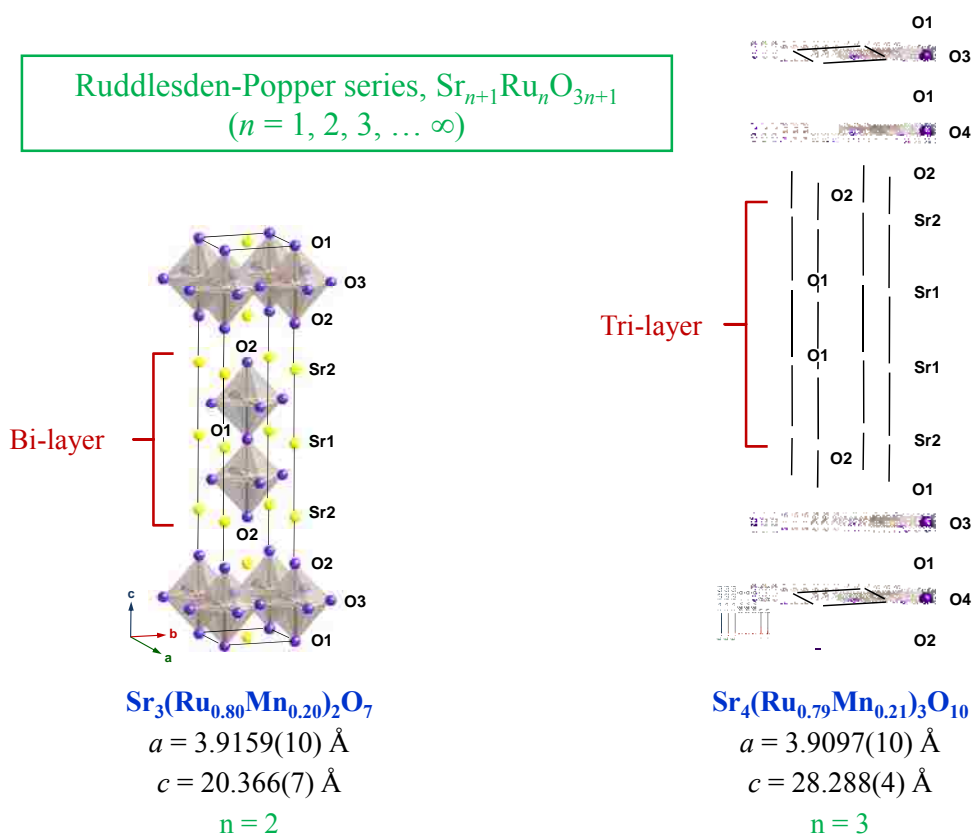
Figure 4.5.   A side by side comparison of two members, n = 2 (left) and n = 3 (right), of the Ruddlesden-Popper series which appeared in two of the Mn doped batches of crystals.

When the 3-2-7 phase concentration of Mn was x = 0.20, the refined Mn occupancy for the 4-3-10 phase was ~24% for the outer layers and ~17% for the inner layer (obtained from refinement of $Sr_4(Ru_{0.79}Mn_{0.21})_3O_{10}$ single crystal). When the 3-2-7 phase concentration of Mn

72
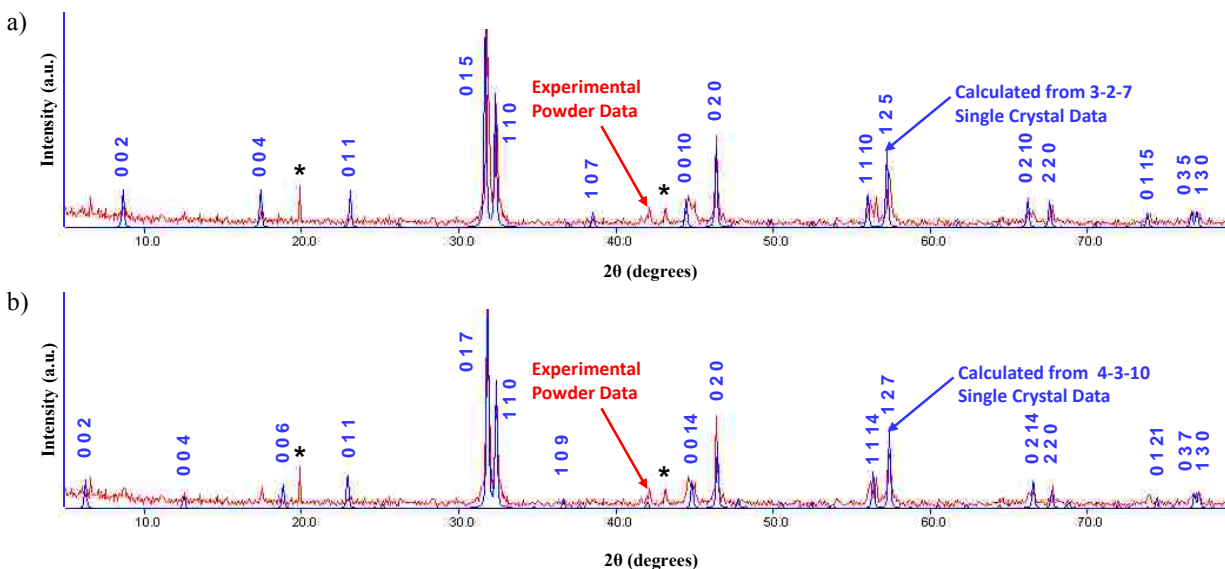
Figure 4.6. Overlay of experimental powder X-ray diffraction data (shown in red) and calculated powder pattern (shown in blue with indexed peaks) based on (a) $Sr_3(Mn_{0.20}Ru_{0.80})_2O_7$, the 3-2-7 phase, and (b) $Sr_4(Mn_{0.21}Ru_{0.79})_3O_{10}$, the 4-3-10 phase, single X-ray diffraction data.

was $x = 0.24$, the refined Mn occupancy for the 4-3-10 phase was ~31% for the outer layers and ~27% for the inner layer (obtained from refinement of $Sr_4(Ru_{0.70}Mn_{0.30})_3O_{10}$ single crystal).

Investigations using X-ray powder diffraction of ground up single crystals reveal similarities between the two phases (**Figure 4.6**). The splitting of the diffraction peaks can be seen and segregated (by indexing) between the two phases (**Figure 4.7**). In the split peaks, the peak with higher 2θ corresponds to the unit cell with the longer c-axis (*i.e.*, 4-3-10 phase) and the peak with lower 2θ corresponds to the unit cell with the shorter c-axis (*i.e.*, 3-2-7 phase).

4.4 Conclusions

In summary, we performed an investigation of both the bulk structure of $Sr_3Ru_2O_7$ single crystals. Our single-crystal X-ray diffraction data is best modeled as a tetragonal structure (*I4/mmm*) with a maximum RuO_6 octahedral rotation of ~ 7° at room temperature and split

73
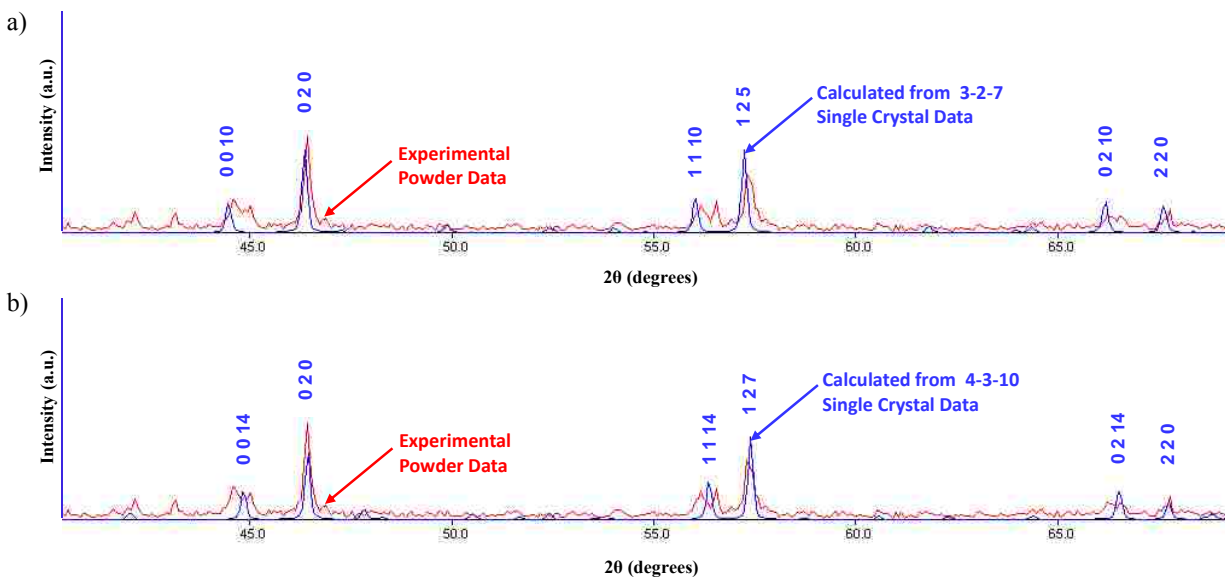
Figure 4.7. A close-up of **Figure 4.6** in the 2θ range of 40-70 degrees showing an overlay of experimental powder X-ray diffraction data (shown in red) and calculated powder pattern (shown in blue with indexed peaks) based on (a) $Sr_3(Mn_{0.20}Ru_{0.80})_2O_7$, the 3-2-7 phase, and (b) $Sr_4(Mn_{0.21}Ru_{0.79})_3O_{10}$, the 4-3-10 phase, single X-ray diffraction data.

occupancy of the equatorial oxygens, O3. Through three thermal cycles between 298 and 90 K, there were no significant changes in the structure of $Sr_3Ru_2O_7$.

Structural studies on a range of different Mn doping concentrations ($0 \leq x \leq 0.7$) show how small amounts of doping and structural distortions (such as octahedral rotation) can influence the physical properties exhibited by the material. These distortions disappear as a function of Mn doping from the undoped $Sr_3Ru_2O_7$ to $Sr_3(Ru_{1-x}Mn_x)_2O_7$ when $x \geq 0.2$.

Finally, it was observed that two different phases (3-2-7 and 4-3-10 phase) of the Ruddlesden-Popper series can crystallize in the same batch of crystals and appear to be very structurally similar when analyzed by powder X-ray diffraction. Although one phase, 3-2-7, contains a bilayer of corner-sharing octahedra and the other, 4-3-10, contains trilayers of corner-sharing octahedra, it is only by close examination of certain hkl reflections in the powder

74

diffraction pattern can the two phases be distinguished. Single crystal X-ray diffraction provides definitive evidence (proof of phase identity) that some of the crystal batches were not phase pure and needed to be re-grown.

4.5   References

(1)   Ruddlesden, S. N.; Popper, P. *Acta Crystallogr.* **1957**, *10*, 538-540.

(2)   Ruddlesden, S. N.; Popper, P. *Acta Crystallogr.* **1958**, *11*, 54-55.

(3)   Hu, B. A.; McCandless, G. T.; Menard, M.; Nascimento, V. B.; Chan, J. Y.; Plummer, E. W.; Jin, R. *Phys. Rev. B* **2010**, *81*, 184104.

(4)   Maeno, Y.; Hashimoto, H.; Yoshida, K.; Nishizaki, S.; Fujita, T.; Bednorz, J. G.; Lichtenberg, F. *Nature* **1994**, *372*, 532-534.

(5)   Huang, Q.; Lynn, J. W.; Erwin, R. W.; Jarupatrakorn, J.; Cava, R. J. *Phys. Rev. B* **1998**, *58*, 8515-8521.

(6)   Cao, G.; Schlottmann, P. *Mod. Phys. Lett. B* **2008**, *22*, 1785-1813.

(7)   Fobes, D.; Yu, M. H.; Zhou, M.; Hooper, J.; O'Connor, C. J.; Rosario, M.; Mao, Z. Q. *Phys. Rev. B* **2007**, *75*, 094429.

(8)   Nakatsuji, S.; Maeno, Y. *Phys. Rev. B* **2000**, *62*, 6458-6466.

(9)   Friedt, O.; Braden, M.; Andre, G.; Adelmann, P.; Nakatsuji, S.; Maeno, Y. *Phys. Rev. B* **2001**, *63*, 174432.

(10)   Matzdorf, R.; Fang, Z.; Ismail; Zhang, J. D.; Kimura, T.; Tokura, Y.; Terakura, K.; Plummer, E. W. *Science* **2000**, *289*, 746-748.

(11)   Moore, R. G.; Zhang, J. D.; Nascimento, V. B.; Jin, R.; Guo, J. D.; Wang, G. T.; Fang, Z.; Mandrus, D.; Plummer, E. W. *Science* **2007**, *318*, 615-619.

(12)   Moore, R. G.; Nascimento, V. B.; Zhang, J. D.; Rundgren, J.; Jin, R.; Mandrus, D.; Plummer, E. W. *Phys. Rev. Lett.* **2008**, *100*, 066102.

(13)   Fang, Z.; Terakura, K. *Phys. Rev. B* **2001**, *64*, 020509.

(14)   Ikeda, S.; Maeno, Y.; Nakatsuji, S.; Kosaka, M.; Uwatoko, Y. *Phys. Rev. B* **2000**, *62*, R6089-R6092.

(15)   Stone, M. B.; Lumsden, M. D.; Jin, R.; Sales, B. C.; Mandrus, D.; Nagler, S. E.; Qiu, Y. *Phys. Rev. B* **2006**, *73*, 174426.

(16)   Ikeda, S.-I.; Shirakawa, N.; Yanagisawa, T.; Yoshida, Y.; Koikegami, S.; Koike, S.; Kosaka, M.; Uwatoko, Y. *J. Phys. Soc. Jpn.* **2004**, *73*, 1322-1325.

(17)   Perry, R. S.; Galvin, L. M.; Grigera, S. A.; Capogna, L.; Schofield, A. J.; Mackenzie, A. P.; Chiao, M.; Julian, S. R.; Ikeda, S. I.; Nakatsuji, S.; Maeno, Y.; Pfleiderer, C. *Phys. Rev. Lett.* **2001**, *86*, 2661-2664.

(18)   Mathieu, R.; Asamitsu, A.; Kaneko, Y.; He, J. P.; Yu, X. Z.; Kumai, R.; Onose, Y.; Takeshita, N.; Arima, T.; Takagi, H.; Tokura, Y. *Phys. Rev. B* **2005**, *72*, 092404.

(19)   Hu, B.; McCandless, G. T.; Garlea, V. O.; Stadler, S.; Xiong, Y.; Chan, J. Y.; Plummer, E. W.; Jin, R. *Phys. Rev. B* **2011**, *84*, 174411.

(20)   Müller-Buschbaum, H.; Wilkens, J. *Z. Anorg. Allg. Chem.* **1990**, *591*, 161-166.

(21)   Sharma, I. B.; Singh, D. *Proc. Indian Acad. Sci.-Chem. Sci.* **1996**, *108*, 415-420.

(22)   Li, R. K.; Greaves, C. *Phys. Rev. B* **2000**, *62*, 3811-3815.

(23)   Shaked, H.; Jorgensen, J. D.; Chmaissem, O.; Ikeda, S.; Maeno, Y. *J. Solid State Chem.* **2000**, *154*, 361-367.

(24)   Shaked, H.; Jorgensen, J. D.; Short, S.; Chmaissem, O.; Ikeda, S. I.; Maeno, Y. *Phys. Rev. B* **2000**, *62*, 8725-8730.

(25)   Kiyanagi, R.; Tsuda, K.; Aso, N.; Kimura, H.; Noda, Y.; Yoshida, Y.; Ikeda, S. I.; Uwatoko, Y. *J. Phys. Soc. Jpn.* **2004**, *73*, 639-642.

(26)   Iwata, K.; Yoshida, Y.; Kosaka, M.; Katano, S. *J. Phys. Soc. Jpn.* **2008**, *77*, 104716.

(27)   Goldschmidt, V. M. *Naturwissenschaften* **1926**, *14*, 477-485.

(28)   Altomare, A.; Burla, M. C.; Camalli, M.; Cascarano, G. L.; Giacovazzo, C.; Guagliardi, A.; Moliterni, A. G. G.; Polidori, G.; Spagna, R. *J. Appl. Crystallogr.* **1999**, *32*, 115-119.

(29)   Sheldrick, G. M. *Acta Crystallogr. Sect. A* **2008**, *64*, 112-122.

(30)   Farrugia, L. J. *J. Appl. Crystallogr.* **1999**, *32*, 837-838.

(31)   Spek, A. L. *J. Appl. Crystallogr.* **2003**, *36*, 7-13.

(32)   Shannon, R. D. *Acta Crystallogr. Sect. A* **1976**, *32*, 751-767.

(33)   Gallon, D. J.; Battle, P. D.; Blundell, S. J.; Burley, J. C.; Coldea, A. I.; Cussen, E. J.; Rosseinsky, M. J.; Steer, C. *Chem. Mater.* **2002**, *14*, 3976-3983.

(34)   Mitchell, J. F.; Millburn, J. E.; Medarde, M.; Short, S.; Jorgensen, J. D.; Fernandez-Diaz, M. T. *J. Solid State Chem.* **1998**, *141*, 599-603.

(35)   Sikora, M.; Oates, C. J.; Szczerba, W.; Kapusta, C.; Zukrowski, J.; Zajac, D.; Borowiec, A.; Ruiz-Bustos, R.; Battle, P. D.; Rosseinsky, M. J. *J. Alloy Compd.* **2007**, *442*, 265-267.

(36)   Hossain, M. A.; Hu, Z.; Haverkort, M. W.; Burnus, T.; Chang, C. F.; Klein, S.; Denlinger, J. D.; Lin, H. J.; Chen, C. T.; Mathieu, R.; Kaneko, Y.; Tokura, Y.; Satow, S.; Yoshida, Y.; Takagi, H.; Tanaka, A.; Elfimov, I. S.; Sawatzky, G. A.; Tjeng, L. H.; Damascelli, A. *Phys. Rev. Lett.* **2008**, *101*, 016404.

(37)   Guo, H. Z.; Li, Y.; Urbina, D.; Hu, B. A.; Jin, R. Y.; Liu, T. J.; Fobes, D.; Mao, Z. Q.; Plummer, E. W.; Zhang, J. D. *Phys. Rev. B* **2010**, *81*, 155121.

(38)   Crawford, M. K.; Harlow, R. L.; Marshall, W.; Li, Z.; Cao, G.; Lindstrom, R. L.; Huang, Q.; Lynn, J. W. *Phys. Rev. B* **2002**, *65*, 214412.

STRUCTURE DETERMINATION OF 3,17-(NO$_2$)$_2$-(TPC)FeNO WITH ANALYSIS OF BONDING, CONFORMATION, AND CRYSTAL PACKING

5.1   Introduction

Corroles have an asymmetric framework similar to the more well-known and studied symmetrical porphyrin structure (see **Figure 5.1**). Although the synthesis of corroles was first published by Johnson and Kay in 1965 while trying to generate a desired precursor to vitamin B$_{12}$,[1] corroles have been overlooked until more recently.[2-9] This increased attention (starting in 1999) has been linked to the development of improved, simpler, and faster synthetic methods that may only require commercially available starting materials.[10,11]
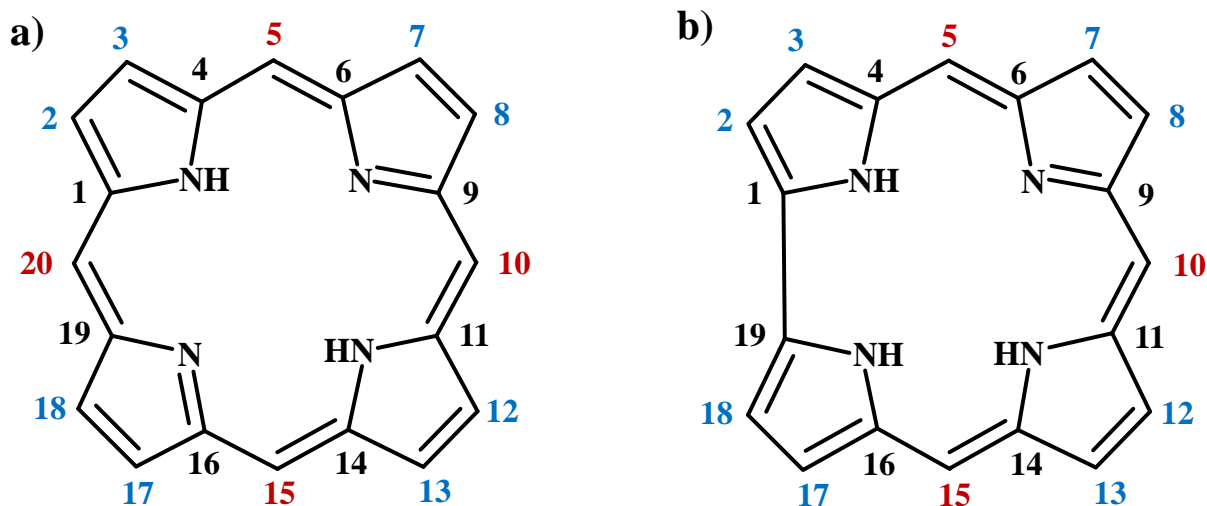
Figure 5.1.   The general molecular structure of a) porphyrin and b) corrole with typical number scheme for the peripheral carbon atoms. The numbers in red and blue denote the *meso-* and β-pyrrole positions, respectively.

Despite the similarities between corroles and porphyrins, their differences have a significant chemical impact. Corroles are trianionic as a ligand with a contracted tetrapyrrolic ring due to absence of a *meso*-carbon between two of the pyrrole rings. In contrast, porphyrin ligands are dianionic with four *meso*-carbon atoms at C5, C10, C15, and C20 positions. The corrole's asymmetric framework also causes regioselectivity when functionalizing the *meso*- and β-pyrrole positions that is not observed in porphyrin compounds.[12,13] The difference in reactivity has been shown to be due to electronic effect (not steric effect).[13] The exploration of selective substitution of corroles and metallocorroles at both the *meso*- and β-pyrrole positions is one of the primary focuses in the synthesis of these compounds.[2,12,14,15]

Recently, my collaborators at Università di Roma Tor Vergata have published nitration experiments to produce nitro derivatives of an iron triphenylcorrole (TPC).[16] Other iron triarylcorrolates were investigated to elucidate the versatility of their published synthetic methods (a two-step procedure and a one-pot synthetic approach). The goal is to evaluate how different *meso*-aryl substituents (with electron-withdrawing and electron-donating groups) would affect formation of the hypothesized reactive species, a corrole π-cation radical substrate,[16-18] as well as the synthetic yield of the reaction.[19]

The two-step procedure yields three different iron corroles – either no nitro substitution at any of β-pyrrole positions, nitro substitution only at the C3 position, or nitro substitution at both the C3 and C17 position (**Figure 5.2**). The one-pot synthetic approach proved to be more regioselective with the iron nitrosyl 3,17-dinitrocorrole as the product. Higher yields were generally achieved with electron-donating substituents on the *meso*-phenyl groups of the triarylcorroles. Higher product yields are suggested to be due to the formation and stabilization of an intermediate iron corrole π-cation radical. It is also observed that electron-withdrawing
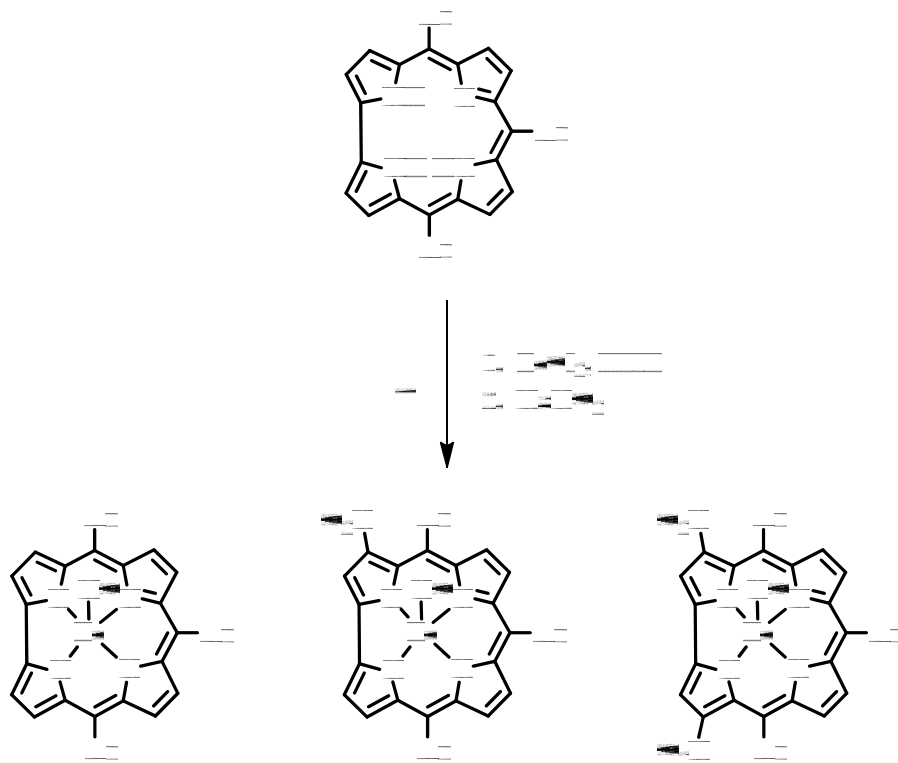
Figure 5.2.   Nitration of Triarylcorroles (Ar = aromatic phenyl group with or without substituents, which are either electron-withdrawing or electron-donating).[19]

groups seem to labilize the axial nitrosyl group. A consequence of this axial ligand lability is the possible formation of a disubstituted iron μ-oxo dimer complex.

In this chapter, the structure determination of 3,17-$(NO_2)_2$-(TPC)FeNO is thoroughly discussed with comparison to previously reported iron corroles. This analysis will also draw attention to an interesting packing relationship of Fe complexes within the unit cell with an usually short O···O distance between axial nitrosyl ligands.

5.2   Experimental Details

"Crystals [of 3,17-$(NO_2)_2$-(TPC)FeNO] were grown by slow diffusion of methanol in a concentrated dichloromethane solution. Single crystal X-ray diffraction data was collected on a Nonius KappaCCD diffractometer with Mo Kα radiation source (λ = 0.71073 Å), graphite monochromator, and Oxford Cryosystems liquid nitrogen cryostream cooler. The structure was

solved by direct methods using SIR97[20] and refined using SHELXL97.[21]   All non-hydrogen atoms were refined anisotropically for the two independent Fe corroles in the unit cell, with H atoms in idealized positions with a C—H bond length of 0.95 Å. Missing symmetry was sought using ADDSYM algorithm within the PLATON single-crystal structure validation program.[22] Crystal data: $C_{37}H_{21}FeN_7O_5$, $M_r = 699.46$ g mol^{-1}, triclinic, space group P-1, $a = 10.4813$ (15) Å, $b = 14.3141$ (15) Å, $c = 21.830$ (3) Å, $\alpha = 74.161$ (5)°, $\beta = 77.960$ (4)°, $\gamma = 80.100$ (5)°, $V = 3058.5$ (6) Å^3, $Z = 4$, $F(000) = 1432$, $D_x = 1.519$ g cm^{-3}, $\mu = 0.55$ mm^{-1}, $T = 100$ K, 35466 measured reflections, 17810 independent reflections, 9725 reflections with $I > 2\sigma(I)$, $R_{int} = 0.064$, $\theta_{max} = 30.0°$, $\theta_{min} = 2.8°$, full-matrix least-squares refinement on F^2, $R_1[F^2 > 2\sigma(F^2)] = 0.058$, $wR_2(F^2) = 0.161$, $S = 1.03$, 901 parameters, 0 restraints, $w = 1 / [\sigma^2(F_o^2) + (0.0765P)^2]$, $\Delta\rho_{max} = 0.94$ eÅ^{-3}, $\Delta\rho_{min} = -0.34$ eÅ^{-3}."[19]   Selected fractional atomic coordinates and displacement parameters are provided in **Tables 5.1 - 5.3**.

5.3   Results and Discussion

"There are two independent Fe corroles in the crystal structure (**Figure 5.3**), with almost identical basic corrole framework (in terms of bond lengths and angles, see **Tables 5.4 - 5.7**) as well as the angle of the linearity of the nitrosyl located in the axial position within the 5-coordinate square pyramid environment. The Fe—N$_{nitrosyl}$ bond lengths, 1.651 (2) Å and 1.652 (2) Å; N—O bond length for the nitrosyl ligands, 1.165 (3) Å and 1.160 (3) Å; Fe—N—O bond angles, 178.9 (2)° and 177.9 (2)°; and the average N$_{nitrosyl}$—Fe—N$_{pyrrole}$ bond angles, 103.6°, which ranges between 102.4 (1)° and 104.5 (1)°, are comparable to other previously reported crystal structures for nitrosyl iron corrole complexes.[23-26] Also, similarities can be observed in the "domed conformation" and Fe—N$_{pyrrole}$ bond length, with a minimum of 1.903 (2) Å, a maximum of 1.931 (2) Å, and an average of 1.915 Å, of this square pyramidal compound

Table 5.1. Fractional Atomic Coordinates and Equivalent Isotropic Displacement Parameters of Non-hydrogen Atoms (Fe1 Complex, Except for Phenyl Groups)

Atom	x	y	z	U_{eq} (Å^2)[a]
Fe1	0.31651 (3)	0.24868 (3)	0.127966 (17)	0.01485 (10)
O1	0.4377 (2)	0.08123 (14)	0.20679 (10)	0.0321 (5)
O2	0.6207 (2)	0.58295 (16)	0.15555 (11)	0.0385 (6)
O3	0.7526 (2)	0.46244 (16)	0.12703 (10)	0.0354 (5)
O4	−0.1981 (2)	0.3778 (2)	0.30099 (13)	0.0600 (8)
O5	−0.1047 (3)	0.25430 (19)	0.36253 (13)	0.0746 (10)
N1	0.3967 (2)	0.35498 (15)	0.13463 (10)	0.0166 (5)
N2	0.4227 (2)	0.25948 (15)	0.04426 (10)	0.0161 (5)
N3	0.1804 (2)	0.19665 (15)	0.10456 (10)	0.0176 (5)
N4	0.1820 (2)	0.30105 (15)	0.18727 (10)	0.0167 (5)
N5	0.3883 (2)	0.15105 (16)	0.17430 (10)	0.0184 (5)
N6	0.6417 (2)	0.50469 (19)	0.14047 (11)	0.0268 (6)
N7	−0.1033 (2)	0.32007 (19)	0.31402 (12)	0.0292 (6)
C1	0.3375 (3)	0.39952 (19)	0.18309 (12)	0.0193 (6)
C2	0.4185 (3)	0.46488 (19)	0.18845 (13)	0.0231 (6)
C3	0.5304 (3)	0.45507 (19)	0.14358 (13)	0.0202 (6)
C4	0.5183 (2)	0.38671 (18)	0.10799 (12)	0.0173 (5)
C5	0.5905 (2)	0.35777 (18)	0.05306 (12)	0.0175 (5)
C6	0.5401 (2)	0.29941 (18)	0.02270 (12)	0.0172 (5)
C7	0.5991 (3)	0.2792 (2)	−0.03876 (13)	0.0227 (6)
C8	0.5190 (3)	0.22581 (19)	−0.05304 (13)	0.0220 (6)
C9	0.4099 (2)	0.21212 (19)	−0.00132 (12)	0.0182 (5)
C10	0.3046 (2)	0.16025 (18)	0.00340 (12)	0.0170 (5)
C11	0.1970 (2)	0.15202 (18)	0.05420 (12)	0.0179 (5)
C12	0.0856 (3)	0.10225 (19)	0.06100 (13)	0.0214 (6)
C13	0.0029 (3)	0.11606 (19)	0.11532 (13)	0.0214 (6)
C14	0.0608 (2)	0.17535 (19)	0.14300 (12)	0.0183 (6)
C15	0.0017 (2)	0.21029 (18)	0.19770 (12)	0.0174 (5)
C16	0.0606 (2)	0.27312 (18)	0.21894 (12)	0.0183 (6)
C17	0.0188 (3)	0.3272 (2)	0.26719 (13)	0.0215 (6)
C18	0.1114 (3)	0.3853 (2)	0.26464 (13)	0.0265 (7)
C19	0.2133 (3)	0.36766 (19)	0.21396 (13)	0.0197 (6)

[a]U_{eq} is defined as one-third of the trace of the orthogonalized U^{ij} tensor.

Table 5.2. Fractional Atomic Coordinates and Equivalent Isotropic Displacement Parameters of Non-hydrogen Atoms (Fe2 Complex, Except for Phenyl Groups)

Atom	x	y	z	U_{eq} (Å^2)[a]
Fe2	0.32239 (3)	0.25232 (3)	0.627951 (17)	0.01609 (10)
O6	0.4579 (2)	0.08777 (15)	0.70186 (10)	0.0368 (5)
O7	0.6919 (2)	0.53944 (19)	0.65790 (11)	0.0496 (7)
O8	0.68319 (19)	0.56139 (14)	0.55658 (10)	0.0320 (5)
O9	−0.1462 (2)	0.39734 (16)	0.83075 (11)	0.0446 (6)
O10	−0.0872 (2)	0.24147 (15)	0.86054 (10)	0.0367 (5)
N8	0.4102 (2)	0.35512 (15)	0.63301 (10)	0.0173 (5)
N9	0.4195 (2)	0.26277 (15)	0.54210 (10)	0.0173 (5)
N10	0.1814 (2)	0.20072 (15)	0.60895 (10)	0.0178 (5)
N11	0.1957 (2)	0.30618 (15)	0.68991 (10)	0.0185 (5)
N12	0.4000 (2)	0.15478 (16)	0.67164 (10)	0.0190 (5)
N13	0.6489 (2)	0.52234 (18)	0.61559 (12)	0.0288 (6)
N14	−0.0727 (2)	0.32346 (18)	0.82502 (11)	0.0263 (5)
C38	0.3603 (2)	0.39928 (19)	0.68287 (12)	0.0181 (5)
C39	0.4444 (3)	0.4644 (2)	0.68441 (13)	0.0225 (6)
C40	0.5471 (2)	0.45867 (19)	0.63324 (13)	0.0195 (6)
C41	0.5267 (2)	0.38982 (18)	0.60043 (12)	0.0184 (6)
C42	0.5941 (2)	0.35842 (18)	0.54587 (12)	0.0178 (5)
C43	0.5403 (2)	0.29871 (18)	0.51835 (12)	0.0190 (6)
C44	0.5980 (3)	0.26928 (19)	0.45957 (13)	0.0232 (6)
C45	0.5126 (3)	0.2181 (2)	0.44730 (13)	0.0233 (6)
C46	0.4027 (3)	0.21183 (19)	0.49930 (12)	0.0199 (6)
C47	0.2932 (3)	0.16273 (19)	0.50627 (12)	0.0188 (6)
C48	0.1891 (2)	0.15820 (18)	0.55850 (13)	0.0185 (6)
C49	0.0721 (3)	0.11329 (19)	0.56695 (14)	0.0233 (6)
C50	−0.0049 (3)	0.12786 (19)	0.62257 (13)	0.0216 (6)
C51	0.0626 (2)	0.18210 (18)	0.64949 (13)	0.0192 (6)
C52	0.0097 (2)	0.21870 (19)	0.70454 (12)	0.0184 (6)
C53	0.0752 (2)	0.27955 (19)	0.72425 (12)	0.0192 (6)
C54	0.0419 (3)	0.33206 (19)	0.77384 (13)	0.0202 (6)
C55	0.1385 (3)	0.38863 (19)	0.76937 (13)	0.0223 (6)

[a] U_{eq} is defined as one-third of the trace of the orthogonalized U^{ij} tensor.

Table 5.3. Fractional Atomic Coordinates and Equivalent Isotropic Displacement Parameters of Non-hydrogen Atoms (Phenyl Rings of Both Complexes)

Atom	x	y	z	U_{eq} (Å^2)[a]
C20	0.7204 (2)	0.39018 (19)	0.01978 (12)	0.0176 (5)
C21	0.8308 (3)	0.3204 (2)	0.01568 (14)	0.0269 (7)
C22	0.9509 (3)	0.3487 (2)	−0.01884 (15)	0.0318 (7)
C23	0.9616 (3)	0.4451 (2)	−0.05019 (14)	0.0316 (7)
C24	0.8526 (3)	0.5150 (2)	−0.04539 (14)	0.0321 (7)
C25	0.7323 (3)	0.4877 (2)	−0.00995 (13)	0.0242 (6)
C26	0.3040 (3)	0.11243 (19)	−0.04960 (12)	0.0195 (6)
C27	0.2738 (3)	0.1683 (2)	−0.10853 (13)	0.0243 (6)
C28	0.2673 (3)	0.1230 (2)	−0.15659 (14)	0.0285 (7)
C29	0.2931 (3)	0.0223 (2)	−0.14625 (14)	0.0261 (6)
C30	0.3249 (3)	−0.0326 (2)	−0.08787 (15)	0.0325 (7)
C31	0.3300 (3)	0.0110 (2)	−0.03913 (14)	0.0294 (7)
C32	−0.1289 (2)	0.18005 (19)	0.23241 (12)	0.0181 (5)
C33	−0.2434 (3)	0.2290 (2)	0.21159 (15)	0.0331 (8)
C34	−0.3651 (3)	0.2019 (2)	0.24504 (15)	0.0337 (7)
C35	−0.3730 (3)	0.1235 (2)	0.29775 (13)	0.0253 (6)
C36	−0.2602 (3)	0.0727 (2)	0.31743 (15)	0.0379 (8)
C37	−0.1378 (3)	0.1020 (2)	0.28583 (15)	0.0389 (8)
C56	0.2358 (3)	0.36932 (19)	0.71662 (13)	0.0195 (6)
C57	0.7284 (2)	0.38478 (19)	0.51451 (13)	0.0185 (6)
C58	0.8317 (3)	0.3501 (2)	0.54878 (15)	0.0298 (7)
C59	0.9587 (3)	0.3693 (2)	0.51925 (16)	0.0331 (7)
C60	0.9829 (3)	0.4231 (2)	0.45550 (15)	0.0308 (7)
C61	0.8818 (3)	0.4575 (2)	0.42179 (15)	0.0324 (7)
C62	0.7546 (3)	0.4378 (2)	0.45068 (14)	0.0276 (7)
C63	0.2869 (3)	0.11548 (19)	0.45417 (13)	0.0211 (6)
C64	0.2587 (3)	0.1721 (2)	0.39516 (14)	0.0311 (7)
C65	0.2503 (3)	0.1275 (2)	0.34670 (15)	0.0337 (7)
C66	0.2721 (3)	0.0266 (2)	0.35749 (15)	0.0328 (7)
C67	0.3014 (4)	−0.0297 (2)	0.41588 (16)	0.0424 (9)
C68	0.3088 (3)	0.0143 (2)	0.46420 (15)	0.0374 (8)
C69	−0.1216 (2)	0.19185 (19)	0.74005 (12)	0.0186 (6)
C70	−0.2338 (3)	0.2601 (2)	0.73616 (14)	0.0288 (7)
C71	−0.3567 (3)	0.2308 (2)	0.76675 (15)	0.0332 (7)
C72	−0.3673 (3)	0.1356 (2)	0.80200 (14)	0.0288 (7)
C73	−0.2561 (3)	0.0703 (2)	0.80838 (15)	0.0328 (7)
C74	−0.1338 (3)	0.0978 (2)	0.77759 (14)	0.0301 (7)

[a] U_{eq} is defined as one-third of the trace of the orthogonalized U^{ij} tensor.
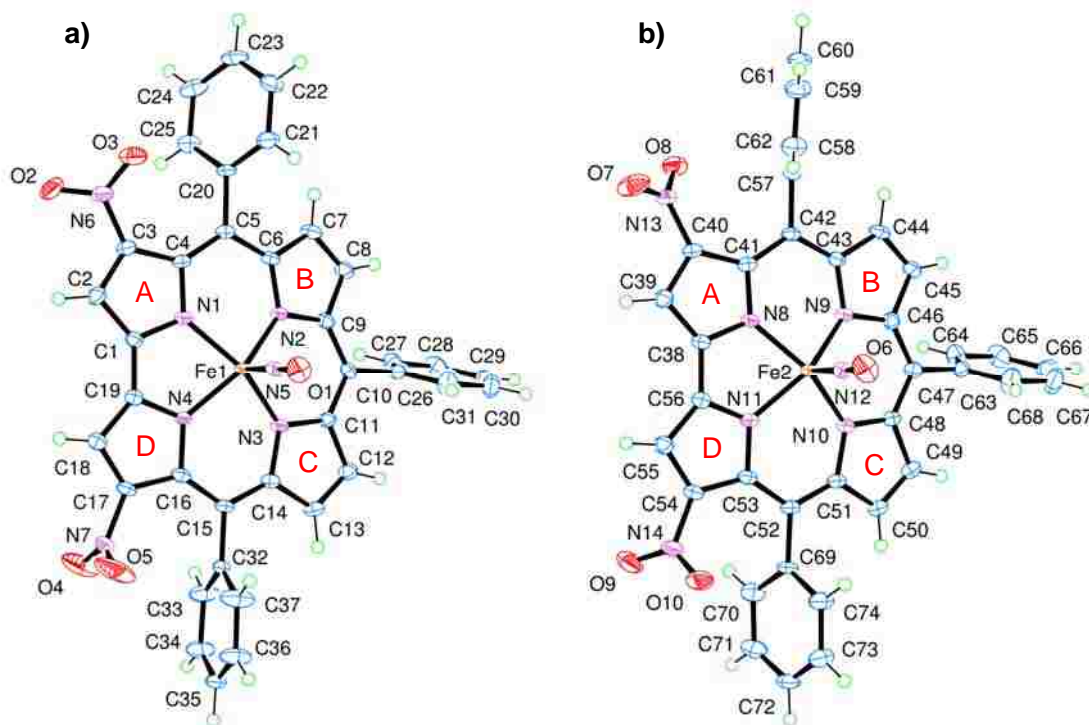
Figure 5.3. The two independent Fe corroles, a) Fe1 complex and b) Fe2 complex, in the unit cell are shown in approximately the same orientation to show how the respective substituents differ in orientation.[19]

with the crystallographic data published for other iron-metallated complexes[16,24-29] of triarylcorroles."[19]

"The planarity of the four pyrrole nitrogen atoms in the two independent molecules in the crystal structure of 3,17-$(NO_2)_2$-(TPC)FeNO are not identical (the root mean square deviation of least–squares planes for N1, N2, N3, N4 and N8, N9, N10, N11 are 0.0061 Å and 0.0243 Å, respectively). Out of these respective planes of pyrrole nitrogens, the Fe atomic sites deviate toward the axial nitrosyl ligand approximately the same distance (i.e., a deviation of 0.456 (1) Å for Fe1 and 0.444 (1) Å for Fe2). The characteristic tilt of the pyrrole subunits are also noted with the deviations of the pyrrolic nitrogen atoms which buckle on the same side as the axial

Table 5.4.   Selected Interatomic Distances (Å) Involving Fe, N, and O

Fe1—N1	1.912 (2)	Fe2—N8	1.903 (2)
Fe1—N2	1.913 (2)	Fe2—N9	1.917 (2)
Fe1—N3	1.931 (2)	Fe2—N10	1.924 (2)
Fe1—N4	1.905 (2)	Fe2—N11	1.912 (2)
Fe1—N5	1.651 (2)	Fe2—N12	1.652 (2)
N1—C1	1.367 (3)	N10—C48	1.379 (3)
N1—C4	1.384 (3)	N10—C51	1.389 (3)
N2—C6	1.385 (3)	N11—C53	1.384 (3)
N2—C9	1.386 (3)	N11—C56	1.362 (3)
N3—C11	1.383 (3)	N13—C40	1.446 (3)
N3—C14	1.387 (3)	N14—C54	1.456 (3)
N4—C16	1.383 (3)	N8—C38	1.372 (3)
N4—C19	1.359 (3)	N8—C41	1.378 (3)
N6—C3	1.448 (3)	N9—C43	1.393 (3)
N7—C17	1.462 (3)	N9—C46	1.386 (3)
O1—N5	1.165 (3)	O10—N14	1.232 (3)
O2—N6	1.224 (3)	O6—N12	1.160 (3)
O3—N6	1.231 (3)	O7—N13	1.205 (3)
O4—N7	1.208 (3)	O8—N13	1.259 (3)
O5—N7	1.209 (3)	O9—N14	1.216 (3)

Table 5.5.   Selected Interatomic Distances (Å) Involving Carbon Framework

C1—C2	1.408 (3)	C38—C56	1.431 (3)
C1—C19	1.424 (3)	C38—C39	1.400 (4)
C2—C3	1.377 (4)	C39—C40	1.389 (4)
C3—C4	1.441 (4)	C40—C41	1.432 (4)
C4—C5	1.402 (4)	C41—C42	1.397 (4)
C5—C6	1.420 (3)	C42—C57	1.494 (3)
C5—C20	1.490 (3)	C42—C43	1.414 (4)
C6—C7	1.439 (3)	C43—C44	1.440 (4)
C7—C8	1.359 (4)	C44—C45	1.357 (4)
C8—C9	1.428 (3)	C45—C46	1.435 (4)
C9—C10	1.405 (3)	C46—C47	1.407 (4)
C10—C11	1.403 (3)	C47—C48	1.400 (3)
C10—C26	1.498 (4)	C47—C63	1.491 (4)
C11—C12	1.432 (3)	C48—C49	1.437 (3)
C12—C13	1.355 (4)	C49—C50	1.357 (4)
C13—C14	1.436 (3)	C50—C51	1.435 (4)
C14—C15	1.404 (4)	C51—C52	1.411 (4)
C15—C16	1.394 (4)	C52—C53	1.396 (4)
C15—C32	1.492 (3)	C52—C69	1.489 (3)
C16—C17	1.427 (4)	C53—C54	1.433 (4)
C17—C18	1.367 (4)	C54—C55	1.374 (4)
C18—C19	1.412 (4)	C55—C56	1.425 (4)

Table 5.6.　　Selected Bond Angles (°) for Domed Conformation and Axial Ligand

C1A—C1—C2	121.11 (16)	C1—C1A—C2A	121.74 (16)
N1—Fe1—N2	87.20 (9)	N8—Fe2—N9	87.70 (9)
N1—Fe1—N3	152.10 (9)	N8—Fe2—N10	153.85 (9)
N2—Fe1—N3	92.70 (9)	N9—Fe2—N10	92.40 (9)
N4—Fe1—N1	79.95 (9)	N8—Fe2—N11	79.81 (9)
N4—Fe1—N2	151.22 (9)	N11—Fe2—N9	150.94 (9)
N4—Fe1—N3	87.11 (9)	N11—Fe2—N10	87.77 (9)
N5—Fe1—N1	104.45 (10)	N12—Fe2—N8	102.36 (10)
N5—Fe1—N2	104.44 (10)	N12—Fe2—N9	103.77 (10)
N5—Fe1—N3	102.58 (10)	N12—Fe2—N10	103.00 (10)
N5—Fe1—N4	103.67 (10)	N12—Fe2—N11	104.48 (10)
C1—N1—Fe1	116.46 (16)	C38—N8—Fe2	117.12 (16)
C4—N1—Fe1	132.58 (18)	C41—N8—Fe2	132.90 (18)
C6—N2—Fe1	126.55 (17)	C43—N9—Fe2	126.04 (18)
C9—N2—Fe1	125.71 (16)	C46—N9—Fe2	125.32 (17)
C11—N3—Fe1	125.35 (17)	C48—N10—Fe2	125.86 (17)
C14—N3—Fe1	126.13 (18)	C51—N10—Fe2	126.31 (18)
C16—N4—Fe1	132.34 (18)	C53—N11—Fe2	131.96 (18)
C19—N4—Fe1	117.40 (17)	C56—N11—Fe2	117.20 (17)
O1—N5—Fe1	178.9 (2)	O6—N12—Fe2	177.9 (2)

nitrosyl ligand and located above a fitted plane of the β-pyrrole carbons (average nitrogen atomic site deviation of 0.17 Å from the two respective least–squares planes of C2, C3, C7, C8, C12, C13, C17, C18 and C39, C40, C44, C45, C49, C50, C54, C55). Using the standard A, B, C, D labels for identification of the corrole's five-membered rings (as shown in **Figure 5.3**), a range of dihedral angles between neighboring pyrrole groups, 1.5 (2) – 14.4 (2)°, is observed in the calculations based on the refined model with the greatest occurring for both independent iron corrole between pyrrole A and B."[19]

　　"The most interesting packing relationship in the crystal structure is between the two different Fe complexes, Fe1 corrole and Fe2[i] corrole (shown in **Figure 5.4**), where the closest Fe2 corrole is located in the adjacent unit cell and related by the symmetry code: (i) −x+1, −y,

Table 5.7. Selected Bond Angles (°) Involving Corrole Framework

C1—N1—C4	109.7 (2)	C38—N8—C41	109.5 (2)
N1—C1—C2	109.7 (2)	N8—C38—C39	110.0 (2)
C3—C2—C1	105.5 (2)	C40—C39—C38	105.3 (2)
C2—C3—C4	110.1 (2)	C39—C40—C41	109.9 (2)
N1—C4—C3	104.8 (2)	N8—C41—C40	105.4 (2)
C6—N2—C9	106.7 (2)	C46—N9—C43	106.4 (2)
N2—C6—C7	109.0 (2)	N9—C43—C44	108.9 (2)
C8—C7—C6	107.3 (2)	C45—C44—C43	107.7 (2)
C7—C8—C9	107.8 (2)	C44—C45—C46	107.4 (2)
N2—C9—C8	109.2 (2)	N9—C46—C45	109.6 (2)
C11—N3—C14	106.8 (2)	C48—N10—C51	106.8 (2)
N3—C11—C12	109.4 (2)	N10—C48—C49	109.3 (2)
C13—C12—C11	107.2 (2)	C50—C49—C48	107.3 (2)
C12—C13—C14	108.0 (2)	C49—C50—C51	107.8 (2)
N3—C14—C13	108.6 (2)	N10—C51—C50	108.8 (2)
C19—N4—C16	109.2 (2)	C56—N11—C53	109.4 (2)
N4—C16—C17	105.4 (2)	N11—C53—C54	105.4 (2)
C18—C17—C16	110.2 (2)	C55—C54—C53	110.4 (2)
C17—C18—C19	105.4 (2)	C54—C55—C56	104.9 (2)
N4—C19—C18	109.8 (2)	N11—C56—C55	109.8 (2)
N1—C1—C19	112.5 (2)	N8—C38—C56	111.9 (2)
N4—C19—C1	111.8 (2)	N11—C56—C38	111.7 (2)
N1—C4—C5	119.2 (2)	N8—C41—C42	120.3 (2)
C4—C5—C6	121.7 (2)	C41—C42—C57	121.4 (2)
C4—C5—C20	123.3 (2)	C41—C42—C43	121.9 (2)
C6—C5—C20	114.9 (2)	C43—C42—C57	116.6 (2)
N2—C6—C5	126.1 (2)	N9—C43—C42	125.4 (2)
N2—C9—C10	124.5 (2)	N9—C46—C47	124.5 (2)
C11—C10—C9	124.1 (2)	C48—C47—C63	118.6 (2)
C9—C10—C26	118.6 (2)	C46—C47—C63	117.8 (2)
C11—C10—C26	117.3 (2)	C48—C47—C46	123.5 (2)
N3—C11—C10	123.8 (2)	N10—C48—C47	124.4 (2)
N3—C14—C15	126.0 (2)	N10—C51—C52	126.0 (2)
C16—C15—C14	121.7 (2)	C53—C52—C51	121.9 (2)
C14—C15—C32	118.1 (2)	C51—C52—C69	117.1 (2)
C16—C15—C32	120.1 (2)	C53—C52—C69	121.0 (2)
N4—C16—C15	120.5 (2)	N11—C53—C52	120.6 (2)
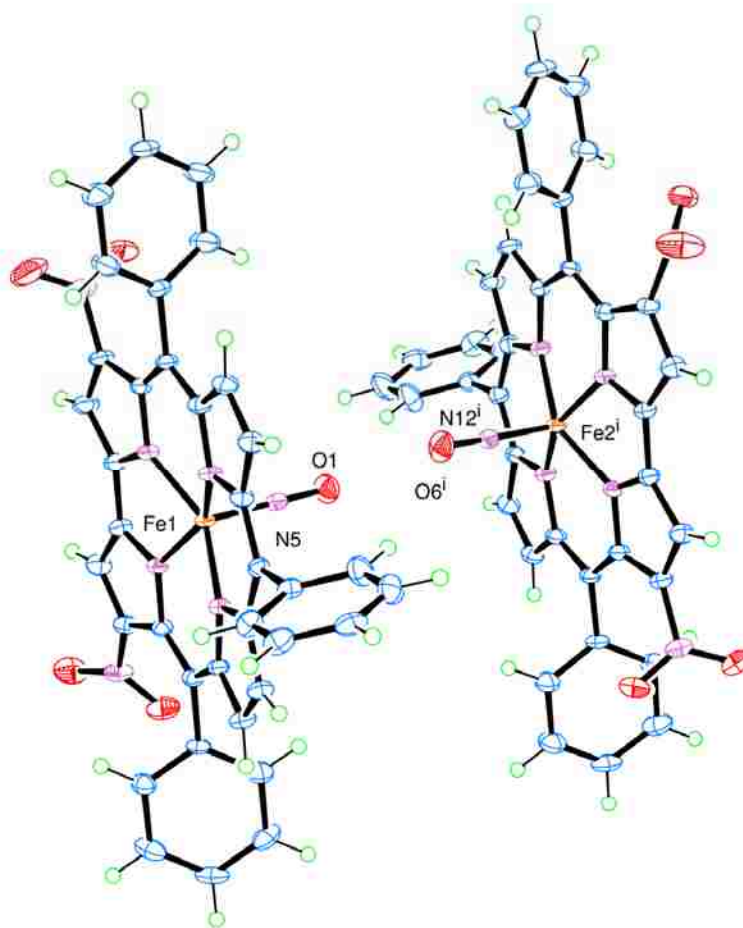
Figure 5.4. The packing relationship between Fe1 corrole and Fe2[i] corrole related by the symmetry code: (i) −x+1, −y, −z+1. The orientation of each complex's axial nitrosyl ligands are pointed towards each other with a short intermolecular O1···O6[i] distance of 2.897 (3) Å.[19]

−z+1. The reason for this interest lies in the orientation of each complex's axial nitrosyl ligands which are point towards each other and have a short intermolecular O1···O6[i] distance of 2.897 (3) Å without any traces of residual electron densities in between the two oxygen atomic sites."[19] Only a few other tetrapyrrolic "examples of axial nitrosyl ligands with such a short O···O distance"[19] have been reported.[30-34]

"[T]he packing relationship in the crystal structure is between the two different Fe complexes, Fe1 corrole and Fe2[i] corrole, with a short intermolecular O···O distance and related

by the symmetry code: (i) −x+1, −y, −z+1, there is a N5···O1···O6^i···N12^i torsion angle of −156.8 (19)°, a "pseudo" inversion center point near (½, 0, ¼), and a 1.85 (14)° dihedral angle between the least-squares plane defined by N1, N2, N3, N4 and the least-squares plane defined by N8^i, N9^i, N10^i, N11^i. The two Fe complexes have a Fe1···Fe2^i distance of 8.5068 (9) Å and are packed in relatively "staggered-like" arrangement with a torsion angle of 176.90 (6)° when measured with the following atomic sites: C10···Fe1···Fe2^i···C47^i. The most significant differences between this pair of nonequivalent iron complexes are the relative orientations of 2 out of the 3 phenyl groups located at the *meso*-positions (Torsion angles: C4—C5—C20—C21, 118.9 (3)°; C9—C10—C26—C31, 107.1 (3)°; C14—C15—C32—C37, 96.2 (3)°; and C41—C42—C57—C58, 64.3 (4)°; C46—C47—C63—C68, 106.9 (3)°; C51—C52—C69—C74, 73.5 (3)) and both the nitro substituents attached to β-pyrrole positions (Torsion angles: C2—C3—N6—O3, 144.3 (3)°; C16—C17—N7—O5, 83.0 (4)°; and C39—C40—N13—O7, 41.0 (4)°; C53—C54—N14—O10, 56.7 (4)°). (See **Tables 5.8 - 5.10** for more torsion angles within the two Fe complexes.) These orientation differences explain why the more than one independent complex is included in the refined model."[19]

"Note: ADDSYM algorithm detects additional 'pseudo' symmetry element, a Z "non-space-group" translation, $z + ½$, and suggests transforming the unit cell with the matrix (-1 0 0, 0 0 -½, 0 -1 0). Application of this matrix leads to a poor fitting model with only one independent Fe corrole that is disordered on all the peripheral substituents, except the *meso*-phenyl group attached to C10, due to the orientation differences listed above. The excessive positional disorder caused by two predominant orientations can be best modeled with two independent Fe corroles without the use of additional constraints/restraints. Also, supporting the modeling of two independent corrole complexes is observation that the *l* odd data are measurable and

Table 5.8.   Selected Torsion Angles (°) for Planarity of Corrole Framework

N1—C1—C2—C3	−2.5 (3)	N8—C38—C39—C40	0.4 (3)
C2—C3—C4—N1	−1.4 (3)	C39—C40—C41—N8	0.1 (3)
N1—C4—C5—C6	2.2 (4)	N8—C41—C42—C43	6.5 (4)
C4—C5—C6—N2	−4.3 (4)	C41—C42—C43—N9	−1.8 (4)
N2—C6—C7—C8	−1.3 (3)	N9—C43—C44—C45	1.1 (3)
C7—C8—C9—N2	1.2 (3)	C44—C45—C46—N9	2.3 (3)
N2—C9—C10—C11	1.7 (4)	N9—C46—C47—C48	−1.3 (4)
C9—C10—C11—N3	2.1 (4)	C46—C47—C48—N10	−0.1 (4)
N3—C11—C12—C13	−0.5 (3)	N10—C48—C49—C50	−0.7 (3)
C12—C13—C14—N3	−0.4 (3)	C49—C50—C51—N10	0.4 (3)
N3—C14—C15—C16	0.5 (4)	N10—C51—C52—C53	−0.2 (4)
C14—C15—C16—N4	−1.7 (4)	C51—C52—C53—N11	0.0 (4)
N4—C16—C17—C18	0.0 (3)	N11—C53—C54—C55	0.3 (3)
C17—C18—C19—N4	0.0 (3)	C54—C55—C56—N11	1.9 (3)
N1—C1—C19—N4	−0.8 (3)	N8—C38—C56—N11	−1.6 (3)

Table 5.9.   Selected Torsion Angles (°) for Domed Conformation of Metal Center

Fe1—N1—C1—C2	170.57 (18)	Fe2—N8—C38—C39	172.81 (17)
Fe1—N1—C1—C19	−9.3 (3)	Fe2—N8—C38—C56	−9.6 (3)
Fe1—N1—C4—C3	−166.64 (18)	Fe2—N8—C41—C40	−171.55 (18)
Fe1—N1—C4—C5	19.9 (4)	Fe2—N8—C41—C42	10.8 (4)
Fe1—N2—C6—C5	−14.0 (4)	Fe2—N9—C43—C42	−19.2 (4)
Fe1—N2—C6—C7	170.68 (17)	Fe2—N9—C43—C44	163.70 (17)
Fe1—N2—C9—C8	−170.76 (17)	Fe2—N9—C46—C45	−165.11 (18)
Fe1—N2—C9—C10	9.9 (4)	Fe2—N9—C46—C47	15.5 (4)
Fe1—N3—C11—C10	−17.0 (4)	Fe2—N10—C48—C47	−12.8 (4)
Fe1—N3—C11—C12	166.05 (17)	Fe2—N10—C48—C49	169.72 (17)
Fe1—N3—C14—C13	−165.58 (17)	Fe2—N10—C51—C50	−169.56 (17)
Fe1—N3—C14—C15	17.9 (4)	Fe2—N10—C51—C52	16.5 (4)
Fe1—N4—C16—C15	−17.1 (4)	Fe2—N11—C53—C52	−17.6 (4)
Fe1—N4—C16—C17	167.44 (19)	Fe2—N11—C53—C54	166.41 (18)
Fe1—N4—C19—C1	10.6 (3)	Fe2—N11—C56—C38	12.1 (3)
Fe1—N4—C19—C18	−169.55 (18)	Fe2—N11—C56—C55	−169.67 (17)

Table 5.10.   Selected Torsion Angles (°) for Peripheral Substituents

meso substituents

C4—C5—C20—C21	118.9 (3)	C41—C42—C57—C58	64.3 (4)
C4—C5—C20—C25	−64.5 (4)	C41—C42—C57—C62	−119.9 (3)
C6—C5—C20—C21	−64.8 (3)	C43—C42—C57—C58	−114.5 (3)
C6—C5—C20—C25	111.9 (3)	C43—C42—C57—C62	61.3 (3)
C9—C10—C26—C27	−74.9 (3)	C46—C47—C63—C64	−73.3 (3)
C9—C10—C26—C31	107.1 (3)	C46—C47—C63—C68	106.9 (3)
C11—C10—C26—C27	103.6 (3)	C48—C47—C63—C64	105.1 (3)
C11—C10—C26—C31	−74.4 (3)	C48—C47—C63—C68	−74.7 (4)
C14—C15—C32—C33	−83.3 (3)	C51—C52—C69—C70	−106.4 (3)
C14—C15—C32—C37	96.2 (3)	C51—C52—C69—C74	73.5 (3)
C16—C15—C32—C33	95.4 (3)	C53—C52—C69—C70	72.0 (4)
C16—C15—C32—C37	−85.1 (4)	C53—C52—C69—C74	−108.1 (3)

β-pyrrole substituents

O2—N6—C3—C2	−30.9 (4)	O7—N13—C40—C39	41.0 (4)
O2—N6—C3—C4	154.0 (3)	O7—N13—C40—C41	−145.2 (3)
O3—N6—C3—C2	144.3 (3)	O8—N13—C40—C39	−135.3 (3)
O3—N6—C3—C4	−30.8 (4)	O8—N13—C40—C41	38.6 (4)
O4—N7—C17—C16	−94.4 (4)	O9—N14—C54—C53	−124.6 (3)
O4—N7—C17—C18	87.4 (4)	O9—N14—C54—C55	59.7 (4)
O5—N7—C17—C16	83.0 (4)	O10—N14—C54—C53	56.7 (4)
O5—N7—C17—C18	−95.2 (4)	O10—N14—C54—C55	−119.0 (3)

included in the list of *hkl* reflections.   If only one corrole was needed for the structure determination, the *l* odd data would be systematically absent."[19]

"[O]ther close contact packing relationships, a pair of symmetrically equivalent Fe1 complexes, which are related by symmetry code: (ii) −x+1, −y+1, −z and located near an inversion center (½, ½, 0), are staggered "back-to-back" as shown in **Figure 5.5** with each corrole's respective axial nitrosyl ligand pointing in opposite directions and a Fe1···Fe1[ii] distance is 8.7399 (10) Å. One of the closest contacts of interest is the substituent attached to C3

and the pyrrole containing the β–carbon C8^{ii}. The relationship between least-squares planes of this β-nitro group and pyrrole B^{ii} is a dihedral angle of 45.83 (14)° with O2 atom angled toward pyrrole B^{ii} and the closest intermolecular distance (O2···C8^{ii}) of 3.360 (4) Å. Another close contact of interest involving these two equivalent Fe1 complexes is the substituent attached to C5 and the basal plane of nitrogen atoms coordinated to the central Fe1^{ii} square pyramid environment. The relationship between least-squares planes of this particular *meso*-phenyl group and four equatorial pyrrole N^{ii} atoms is a dihedral angle of 63.89 (7)° with the C24—C25 bond angled toward N1^{ii}···N4^{ii}. The details of this relationship include intermolecular distances of
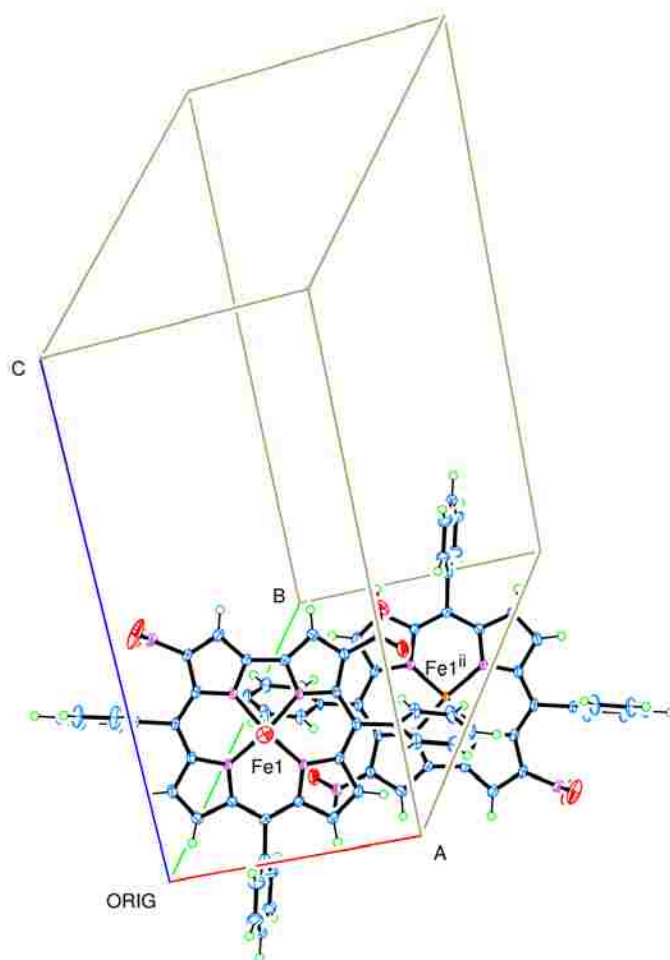
Figure 5.5.   A pair of symmetrically equivalent Fe1 complexes related by symmetry code: (ii) –x+1, –y+1, –z, located near an inversion center (½, ½, 0), and staggered "back-to-back" with each corrole's respective axial nitrosyl ligand pointing in opposite directions.[19]

93
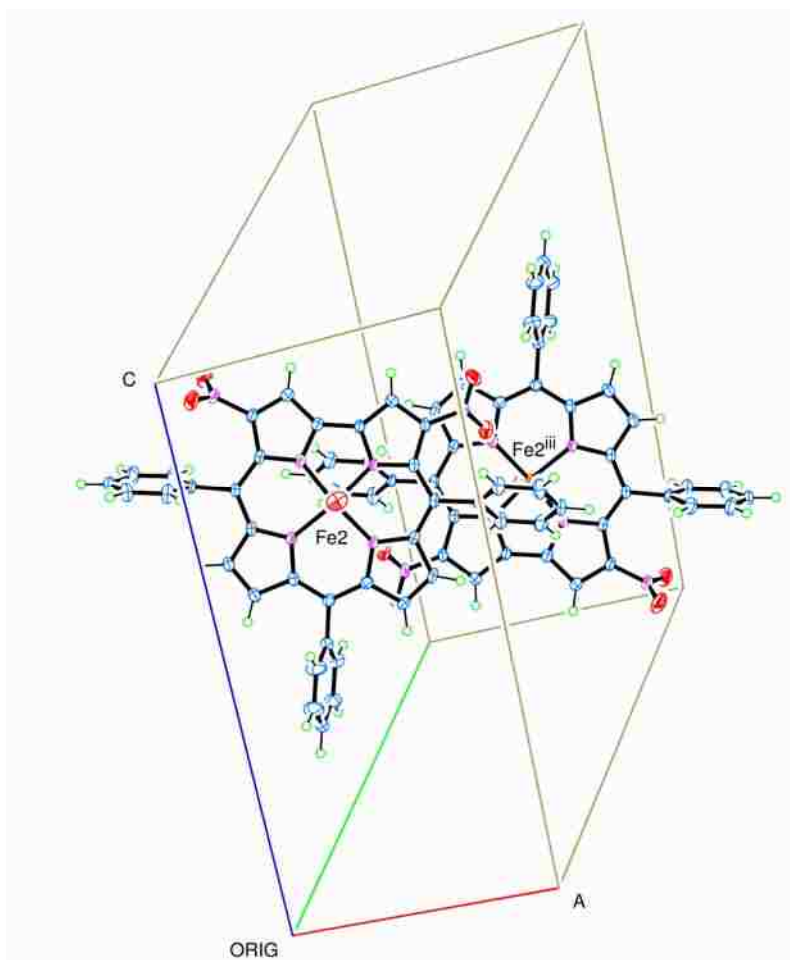
Figure 5.6. A pair of symmetrically equivalent Fe2 complexes related by symmetry code: (iii) –x+1, –y+1, –z+1, located near an inversion center (½, ½, ½), and staggered "back-to-back" with each corrole's respective axial nitrosyl ligand pointing in opposite directions.[19]

3.384 (4) Å (C25···N1[ii]) and 3.514 (4) Å (C24···N4[ii]) and a small torsion angle of 3.90 (14)° (N4[ii]···C24—C25···N1[ii])."[19]

"The final structural examination involves two symmetrical equivalent Fe2 complexes. These corroles are related by symmetry code: (iii) –x+1, –y+1, –z+1, located near an inversion center (½, ½, ½), and are staggered "back-to-back" as shown in **Figure 5.6** with a Fe2···Fe2[iii] distance is 8.6096 (10) Å. Similar to the comparison between symmetrically equivalent Fe1 complexes, there are close contacts between the substituent attached to C40 and pyrrole that

includes N9[iii]. The relationship between least-squares planes of the β-nitro group and pyrrole B[iii] is a dihedral angle of 34.70 (15)° with O8 atom angled toward pyrrole B[iii] and the closest distance (O8···N9[iii]) of 3.035 (3) Å. Also, there is a dihedral angle of 62.53 (7)° between least-squares planes of the *meso*-phenyl group attached to C42 and four equatorial pyrrole N[iii] atoms with two short intermolecular distances of 3.421 (4) Å (C62···N8[iii]) and 3.664 (4) Å (C61···N11[iii]), and a "*cis*-like" torsion angle of -0.01 (13)° (N11[iii]···C61—C62···N8[iii])."[19]

5.4   Conclusions

The structure determination of 3,17-$(NO_2)_2$-(TPC)FeNO was thoroughly compared to previously reported iron corrole complexes. This analysis highlighted a packing relationship of Fe complexes within the unit cell with an unusually short O···O distance between axial nitrosyl ligands. Two independent Fe complexes where modeled in the crystal structure of this compound. Although the complexes are similar in bond lengths, bond angles, and "domed confirmation", they are most obviously conformationally different when comparing the torsion angles of the *meso*-phenyl ring and β-nitro groups.

The elucidation of the structure for this compound validates the interpretation of the ^{1}H-NMR spectra regarding the nitro substitution on the C3 and C13 position. Interpreting chemical shifts in the β-pyrrole region (~ 8 to 10 ppm) is not always straightforward (especially in cases when unexpected β-substitution occurred). This was the case with another corrole complex, 3,12-$(NO_2)_2$-(TTC)CoPPh$_3$, which I solved and published with my collaborators (see **Figure 5.7**).[35] Until this structure determination, the general consensus regarding disubstitution trends is that the functionalization should only involve the β-carbons on the "A" and "D" pyrroles since all previous reports contain either the 3,17 or 2,17 substituted corroles. This is the 1st (to the best of our knowledge) antipodal 3,12 substituted corrole reported in literature.

Detailed electrochemical and spectroelectrochemical results have also been reported elsewhere by my collaborators.[19,35] These results show the influence of selective mono- and di-nitro substitution on the triarylcorroles substrate. The most interesting influence observed in their study is that the mono-nitro substitution has a significantly larger effect than di-nitro substitution on the redox behavior of the macrocycle. The combination of chemical and structural information will help researchers interested in tetrapyrrolic complexes determine the best complex design to fit their desired application.

Figure 5.7. Crystal structure of 3,12-$(NO_2)_2$-(TTC)CoPPh$_3$ with 50% ellipsoids.

5.5   References

(1)   Johnson, A. W.; Kay, I. T. *J. Chem. Soc.* **1965**, 1620-1629.

(2)   Aviv-Harel, I.; Gross, Z. *Chem.-Eur. J.* **2009**, *15*, 8382-8394.

(3)   Kupershmidt, L.; Okun, Z.; Amit, T.; Mandel, S.; Saltsman, I.; Mahammed, A.; Bar-Am, O.; Gross, Z.; Youdim, M. B. H. *J. Neurochem.* **2010**, *113*, 363-373.

(4)   Kanamori, A.; Catrinescu, M. M.; Mahammed, A.; Gross, Z.; Levin, L. A. *J. Neurochem.* **2010**, *114*, 488-498.

(5)   Barbe, J. M.; Canard, G.; Brandes, S.; Guilard, R. *Chem.-Eur. J.* **2007**, *13*, 2118-2129.

(6)   He, C. L.; Ren, F. L.; Zhang, X. B.; Han, Z. X. *Talanta* **2006**, *70*, 364-369.

(7)   Gatto, E.; Malik, M. A.; Di Natale, C.; Paolesse, R.; D'Amico, A.; Lundstrom, I.; Filippini, D. *Chem.-Eur. J.* **2008**, *14*, 6057-6060.

(8)   Paolesse, R.; Mandoj, F.; Marini, A.; Di Natale, C. In *Encyclopedia of Nanoscience and Nanotechnology*; Nalwa, H., Ed.; American Science Publishers: Valencia, CA, 2004.

(9)   Andrioletti, B.; Rose, E. *J. Chem. Soc.-Perkin Trans. 1* **2002**, 715-716.

(10)   Gross, Z.; Galili, N.; Saltsman, I. *Angew. Chem.-Int. Edit.* **1999**, *38*, 1427-1429.

(11)   Paolesse, R.; Jaquinod, L.; Nurco, D. J.; Mini, S.; Sagone, F.; Boschi, T.; Smith, K. M. *Chem. Commun.* **1999**, 1307-1308.

(12)   Paolesse, R. *Synlett* **2008**, 2215-2230.

(13)   Saltsman, I.; Mahammed, A.; Goldberg, I.; Tkachenko, E.; Botoshansky, M.; Gross, Z. *J. Am. Chem. Soc.* **2002**, *124*, 7411-7420.

(14)   Gryko, D. T.; Fox, J. P.; Goldberg, D. P. *J. Porphyrins Phthalocyanines* **2004**, *8*, 1091-1105.

(15)   Nardis, S.; Monti, D.; Paolesse, R. *Mini-Rev. Org. Chem.* **2005**, *2*, 355-374.

(16)   Stefanelli, M.; Nardis, S.; Tortora, L.; Fronczek, F. R.; Smith, K. M.; Licoccia, S.; Paolesse, R. *Chem. Commun.* **2011**, *47*, 4255-4257.

(17)   Walker, F. A.; Licoccia, S.; Paolesse, R. *J. Inorg. Biochem.* **2006**, *100*, 810-837.

(18)   Ye, S. F.; Tuttle, T.; Bill, E.; Simkhovich, L.; Gross, Z.; Thiel, W.; Neese, F. *Chem.-Eur. J.* **2008**, *14*, 10839-10851.

(19)   Nardis, S.; Stefanelli, M.; Mohite, P.; Pomarico, G.; Tortora, L.; Manowong, M.; Chen, P.; Kadish, K. M.; Fronczek, F. R.; McCandless, G. T.; Smith, K. M.; Paolesse, R. *Inorg. Chem.* **2012**, *51*, 3910-3920.

(20)   Altomare, A.; Burla, M. C.; Camalli, M.; Cascarano, G. L.; Giacovazzo, C.; Guagliardi, A.; Moliterni, A. G. G.; Polidori, G.; Spagna, R. *J. Appl. Crystallogr.* **1999**, *32*, 115-119.

(21)   Sheldrick, G. M. *Acta Crystallogr. Sect. A* **2008**, *64*, 112-122.

(22)   Spek, A. L. *J. Appl. Crystallogr.* **2003**, *36*, 7-13.

(23)   Autret, M.; Will, S.; Van Caemelbecke, E.; Lex, J.; Gisselbrecht, J. P.; Gross, M.; Vogel, E.; Kadish, K. M. *J. Am. Chem. Soc.* **1994**, *116*, 9141-9149.

(24)   Simkhovich, L.; Goldberg, I.; Gross, Z. *Inorg. Chem.* **2002**, *41*, 5433-5439.

(25)   Joseph, C. A.; Lee, M. S.; Iretskii, A. V.; Wu, G. A.; Ford, P. C. *Inorg. Chem.* **2006**, *45*, 2075-2082.

(26)   Bröring, M.; Milsmann, C.; Ruck, S.; Köhler, S. *J. Organomet. Chem.* **2009**, *694*, 1011-1015.

(27)   Simkhovich, L.; Galili, N.; Saltsman, I.; Goldberg, I.; Gross, Z. *Inorg. Chem.* **2000**, *39*, 2704-2705.

(28)   Simkhovich, L.; Mahammed, A.; Goldberg, I.; Gross, Z. *Chem.-Eur. J.* **2001**, *7*, 1041-1055.

(29)   Nardis, S.; Paolesse, R.; Licoccia, S.; Fronczek, F. R.; Vicente, M. G. H.; Shokhireva, T. K.; Cai, S.; Walker, F. A. *Inorg. Chem.* **2005**, *44*, 7030-7046.

(30)   Yi, G. B.; Khan, M. A.; Powell, D. R.; Richter-Addo, G. B. *Inorg. Chem.* **1998**, *37*, 208-214.

(31)   Ellison, M. K.; Scheidt, W. R. *J. Am. Chem. Soc.* **1999**, *121*, 5210-5219.

(32)   Richter-Addo, G. B.; Wheeler, R. A.; Hixson, C. A.; Chen, L.; Khan, M. A.; Ellison, M. K.; Schulz, C. E.; Scheidt, W. R. *J. Am. Chem. Soc.* **2001**, *123*, 6314-6326.

(33)   Cheng, L.; Powell, D. R.; Khan, M. A.; Richter-Addo, G. B. *Inorg. Chem.* **2001**, *40*, 125-133.

(34)   Lee, J.; Yi, G. B.; Powell, D. R.; Khan, M. A.; Richter-Addo, G. B. *Can. J. Chem.-Rev. Can. Chim.* **2001**, *79*, 830-840.

(35)   Stefanelli, M.; Pomarico, G.; Tortora, L.; Nardis, S.; Fronczek, F. R.; McCandless, G. T.; Smith, K. M.; Manowong, M.; Fang, Y. Y.; Chen, P.; Kadish, K. M.; Rosa, A.; Ricciardi, G.; Paolesse, R. *Inorg. Chem.* **2012**, *51*, 6928-6942.

CHAPTER 6 [†]

CRYSTAL STRUCTURE OF (*E*)-3,3',4,4',7,7',8,8'-OCTAMETHYL-2*H*,2'*H*-[1,1'-BI(CYCLOPENTA[*fg*]ACENAPHTHYLENYLIDENE)]-2,2',5,5',6,6'-HEXAONE DICHLOROMETHANE MONOSOLVATE

6.1   Introduction

(*E*)-3,3',4,4',7,7',8,8'-octamethyl-2*H*,2'*H*-[1,1'-bi(cyclopenta[*fg*]acenaphthylenylidene)]-2,2',5,5',6,6'-hexaone dichloromethane monosolvate is a side product of the previously reported oxidation reaction (**Figure 6.1**) of 3,4,7,8-tetramethylcyclopenta[*fg*]acenaphthylene-1,5(2*H*,6*H*)-dione with SeO$_2$ in a dioxane/water solvent mixture under reflux conditions into the desired 3,4,7,8-tetramethylcyclopenta[*fg*]acenaphthylene-1,2,5,6-tetraone major product.[1]   The yield of this minor product is < 5% and its crystal structure was not previously published.
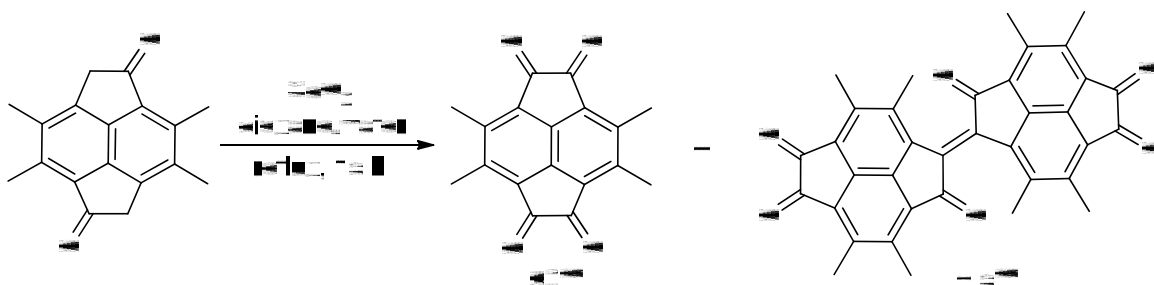
Figure 6.1.   Oxidation of 3,4,7,8-tetramethylcyclopenta[*fg*]acenaphthylene-1,5(2*H*,6*H*)-dione.[1]

The title compound, C$_{36}$H$_{24}$O$_6$·CH$_2$Cl$_2$, is a dimer of two planar tetracyclic pyracene frameworks (each with four methyl groups and three carbonyl groups on the peripheral carbons) twisted along a central C=C bond with a dihedral angle of 50.78 (3)° at 90 K. This compound is of interest with respect to the synthesis of fullerene fragments, such as corannulene and

----

semibuckminsterfullerene derivatives (or "buckybowls"). Recent reviews for the synthesis of fullerene fragments have been published[2-4] as well as compounds structurally related to the title compound.[1,5-7] Structural details, such as planarity analysis of fused rings, out-of-plane deviation of substituents, intermolecular interactions, and longer than typical bond lengths, of (*E*)-3,3',4,4',7,7',8,8'-octamethyl-2*H*,2'*H*-[1,1'-bi(cyclopenta[*fg*]acenaphthylenylidene)]-2,2',5,5',6,6'-hexaone dichloromethane monosolvate will be discussed and compared with compounds with similar structural features.

6.2   Experimental Details

Single crystals were obtained by recrystallizing the title compound in dichloromethane. For single crystal X-ray diffraction, a 0.17 x 0.27 x 0.33 mm^3 crystal was mounted on a glass fiber with vacuum grease. Diffraction data was collected on a Nonius KappaCCD diffractometer using MoKα radiation (λ = 0.71073 Å) and equipped with a graphite monochromator. The crystal kept cool (T = 90 K) throughout the experiment with the aid of Oxford Cryosystems cryostream and controller. The programs / software used are the following: data collection, COLLECT;[8] cell refinement, HKL SCALEPACK;[9] data reduction, HKL DENZO and SCALEPACK;[9] initial model, SIR97;[10] structural refinement, SHELXL97;[11] molecular graphics, ORTEP-3 for Windows;[12] and publication preparation, SHELXL97[11] and publCIF.[13]   A summary of the crystallographic parameters, fractional atomic coordinates, displacement parameters, interatomic distances, and torsion angles are provided in **Tables 6.1-6.7**.

All non-hydrogen atoms were identified and subsequently refined anisotropically. With the remaining unaccounted electron densities that are visible in SXGRAPH[14] difference Fourier map and approximately C—H bonding distance (~1 Å) away from a refined carbon site, hydrogen atomic sites were generated using HFIX commands and refined as idealized "riding"

Table 6.1.   Crystallographic Parameters

Crystal data

Formula	$C_{36}H_{24}O_6 \cdot CH_2Cl_2$	$F(000)$	660
MW (g mol^{-1})	637.48	d (g cm^{-3})	1.447
Crystal system	Triclinic	Mo $K\alpha$ radiation	
Space group	P-1 (No. 2)	λ (Å)	0.71073
a (Å)	8.6644 (15)	Cell parameters from:	
b (Å)	10.959 (2)	6338 reflections	
c (Å)	15.856 (3) Å	θ (°)	2.6–27.5
α (°)	94.241 (10)	μ (mm^{-1})	0.27
β (°)	101.501 (9)	T (K)	90.0 (5)
γ (°)	95.204 (10)°	Crystal shape	Tabular
V (Å^3)	1462.7 (5)	Crystal color	Red
Z	2		

Data collection

Nonius KappaCCD diffractometer		Total reflections	12739
(with an Oxford Cryosystems cryostream cooler)			
Radiation source	fine-focus sealed tube	Unique reflections	6679
Monochromator	graphite	Reflections $I>2\sigma(I)$	5001
Detector resolution (mm^{-1})	9 pixels	$^aR_{int}$	0.031
θ_{max}(°),θ_{min}(°)	27.5, 2.6		
CCD scans		h	-11→11
Absorption correction	multi-scan	k	-14→14
T_{min}, T_{max}	0.915, 0.956	l	-20→20

Refinement

Refinement on F^2		Secondary atom site location:	
Least-squares matrix	full	difference Fourier map	
$^bR_1[F^2>2\sigma(F^2)]$	0.045	Hydrogen site location:	
$^cwR_2(F^2)$	0.114	inferred from neighbouring sites	
^dS	1.03	H-atom parameters constrained	
Reflections	6679	$(\Delta/\sigma)_{max}$	0.001
Parameters	414	$\Delta\rho_{max}$ (eÅ^{-3})	0.8
Constraints	0	$\Delta\rho_{min}$ (eÅ^{-3})	-0.4
Primary atom site location:		Extinction coefficient	None
structure-invariant direct methods			

$^aR_{int} = \Sigma \, | \, F_o^2 - F_o^2 \text{ (mean)} \, | \, / \, \Sigma \, [\, F_o^2 \,]$

$^bR_1 = \Sigma \, | \, | \, F_o \, | - | \, F_c \, | \, | \, / \, \Sigma \, | \, F_o \, |$

$^cwR_2 = [\, \Sigma \, [\, w(\, F_o^2 - F_c^2 \,)^2 \,] \, / \, \Sigma \, [\, w(\, F_o^2 \,)^2 \,] \,]^{1/2}$ where $w = 1 \, / \, [\, \sigma^2(F_o^2) + (0.0463P)^2 + 0.9955P \,]$

$^dS = [\, \Sigma \, [\, w(\, F_o^2 - F_c^2 \,)^2 \,] \, / \, (n-p) \,]^{1/2}$

Table 6.2. Fractional Atomic Coordinates and Equivalent Isotropic Displacement Parameters of Non-hydrogen Atoms

Atom	x	y	z	U_{eq} (Å^2)[a]
O1	0.29471 (15)	0.01404 (12)	0.78727 (8)	0.0189 (3)
O2	−0.40015 (16)	−0.17056 (13)	0.40273 (9)	0.0229 (3)
O3	−0.47615 (16)	0.08134 (13)	0.40444 (9)	0.0241 (3)
C1	0.1538 (2)	0.18790 (17)	0.73469 (12)	0.0149 (4)
C2	0.1864 (2)	0.05194 (17)	0.73837 (12)	0.0148 (4)
C3	0.0352 (2)	−0.14369 (17)	0.63465 (12)	0.0156 (4)
C4	−0.0979 (2)	−0.17981 (17)	0.56337 (12)	0.0158 (4)
C5	−0.3252 (2)	−0.08908 (18)	0.45439 (12)	0.0170 (4)
C6	−0.3647 (2)	0.05076 (18)	0.45374 (12)	0.0175 (4)
C7	−0.2161 (2)	0.24347 (17)	0.56136 (12)	0.0153 (4)
C8	−0.0848 (2)	0.27807 (17)	0.63459 (12)	0.0152 (4)
C9	0.0192 (2)	0.19179 (17)	0.66238 (11)	0.0137 (4)
C10	−0.0186 (2)	0.06873 (17)	0.62502 (11)	0.0139 (4)
C11	0.0713 (2)	−0.01902 (17)	0.66389 (11)	0.0143 (4)
C12	−0.1463 (2)	0.03443 (17)	0.55865 (11)	0.0141 (4)
C13	−0.1852 (2)	−0.09025 (17)	0.52606 (12)	0.0148 (4)
C14	−0.2437 (2)	0.12224 (17)	0.52408 (12)	0.0149 (4)
C15	0.1294 (2)	−0.23962 (18)	0.67640 (13)	0.0213 (4)
C16	−0.1435 (2)	−0.31386 (17)	0.53295 (13)	0.0199 (4)
C17	−0.3239 (2)	0.33712 (18)	0.52803 (13)	0.0206 (4)
C18	−0.0708 (2)	0.40459 (18)	0.68069 (13)	0.0203 (4)

[a]U_{eq} is defined as one-third of the trace of the orthogonalized U^{ij} tensor.

positions. Final refinement cycles included the SHELXL97[11] recommended weighting scheme.

Missing symmetry was checked using ADDSYM feature in PLATON.[15]

Table 6.3. Fractional Atomic Coordinates and Equivalent Isotropic Displacement Parameters of Non-hydrogen Atoms (Continued)

Atom	x	y	z	U_{eq} (Å^2)[a]
O1A	0.25716 (16)	0.42583 (12)	0.66908 (8)	0.0198 (3)
O2A	0.93757 (17)	0.58456 (15)	1.06555 (10)	0.0319 (4)
O3A	0.79850 (17)	0.39242 (15)	1.15279 (9)	0.0278 (4)
C1A	0.2599 (2)	0.28086 (17)	0.78111 (12)	0.0151 (4)
C2A	0.3176 (2)	0.39486 (17)	0.73854 (12)	0.0161 (4)
C3A	0.5858 (2)	0.54462 (18)	0.79525 (13)	0.0192 (4)
C4A	0.7172 (2)	0.57293 (18)	0.86888 (14)	0.0208 (4)
C5A	0.8232 (2)	0.51493 (19)	1.03078 (14)	0.0245 (5)
C6A	0.7485 (2)	0.40834 (19)	1.07795 (13)	0.0204 (4)
C7A	0.4972 (2)	0.24708 (18)	1.01322 (12)	0.0186 (4)
C8A	0.3683 (2)	0.21677 (18)	0.93896 (12)	0.0171 (4)
C9A	0.3677 (2)	0.27995 (17)	0.86501 (12)	0.0156 (4)
C10A	0.4848 (2)	0.37987 (18)	0.86894 (12)	0.0166 (4)
C11A	0.4710 (2)	0.44799 (17)	0.79784 (12)	0.0160 (4)
C12A	0.6036 (2)	0.41108 (18)	0.94072 (12)	0.0180 (4)
C13A	0.7207 (2)	0.50925 (18)	0.94145 (13)	0.0207 (4)
C14A	0.6118 (2)	0.34447 (19)	1.01342 (12)	0.0187 (4)
C15A	0.5742 (2)	0.61827 (19)	0.71843 (14)	0.0238 (5)
C16A	0.8495 (2)	0.6702 (2)	0.86588 (16)	0.0280 (5)
C17A	0.5073 (2)	0.1721 (2)	1.08941 (13)	0.0246 (5)
C18A	0.2343 (2)	0.12270 (19)	0.94566 (13)	0.0214 (4)
Cl1	0.77328 (7)	−0.03949 (5)	0.77593 (4)	0.03263 (15)
Cl2	0.79071 (6)	0.22106 (5)	0.83069 (4)	0.03157 (15)
C19	0.6709 (2)	0.0932 (2)	0.76933 (15)	0.0276 (5)

[a]U_{eq} is defined as one-third of the trace of the orthogonalized U^{ij} tensor.

Table 6.4.   Anisotropic Atomic Displacement Parameters (Å^2) of Non-hydrogen Atoms

Atom	U^{11}	U^{22}	U^{33}	U^{12}	U^{13}	U^{23}
O1	0.0185 (7)	0.0184 (7)	0.0186 (7)	0.0039 (5)	−0.0002 (5)	0.0033 (6)
O2	0.0218 (7)	0.0223 (8)	0.0211 (7)	−0.0023 (6)	0.0003 (6)	−0.0035 (6)
O3	0.0206 (7)	0.0259 (8)	0.0221 (8)	0.0027 (6)	−0.0039 (6)	0.0006 (6)
C1	0.0144 (9)	0.0153 (9)	0.0149 (9)	0.0016 (7)	0.0027 (7)	0.0021 (7)
C2	0.0145 (9)	0.0168 (9)	0.0131 (9)	0.0009 (7)	0.0027 (7)	0.0029 (7)
C3	0.0178 (9)	0.0160 (10)	0.0139 (9)	0.0016 (7)	0.0049 (7)	0.0018 (7)
C4	0.0184 (9)	0.0148 (9)	0.0147 (9)	−0.0004 (7)	0.0055 (7)	0.0013 (7)
C5	0.0168 (9)	0.0191 (10)	0.0148 (9)	−0.0005 (8)	0.0040 (7)	0.0002 (8)
C6	0.0147 (9)	0.0231 (10)	0.0138 (9)	0.0001 (8)	0.0020 (7)	0.0019 (8)
C7	0.0142 (9)	0.0163 (10)	0.0152 (9)	0.0013 (7)	0.0019 (7)	0.0029 (7)
C8	0.0159 (9)	0.0151 (9)	0.0143 (9)	−0.0004 (7)	0.0029 (7)	0.0018 (7)
C9	0.0147 (9)	0.0141 (9)	0.0119 (9)	0.0000 (7)	0.0023 (7)	0.0016 (7)
C10	0.0145 (9)	0.0145 (9)	0.0129 (9)	0.0000 (7)	0.0039 (7)	0.0014 (7)
C11	0.0151 (9)	0.0164 (9)	0.0117 (9)	0.0020 (7)	0.0030 (7)	0.0022 (7)
C12	0.0151 (9)	0.0154 (9)	0.0120 (9)	−0.0002 (7)	0.0042 (7)	0.0013 (7)
C13	0.0155 (9)	0.0150 (9)	0.0130 (9)	−0.0017 (7)	0.0031 (7)	−0.0006 (7)
C14	0.0131 (8)	0.0176 (10)	0.0133 (9)	0.0004 (7)	0.0018 (7)	0.0022 (7)
C15	0.0289 (11)	0.0156 (10)	0.0185 (10)	0.0045 (8)	0.0016 (8)	0.0017 (8)
C16	0.0257 (10)	0.0150 (10)	0.0185 (10)	0.0003 (8)	0.0039 (8)	0.0020 (8)
C17	0.0184 (10)	0.0178 (10)	0.0226 (10)	0.0029 (8)	−0.0021 (8)	0.0000 (8)
C18	0.0205 (10)	0.0155 (10)	0.0227 (10)	0.0039 (8)	−0.0012 (8)	−0.0003 (8)

6.3   Results and Discussion

The structure of title compound (**Figure 6.2**) can be described as a dimer of two pyracene frameworks joined together with a C=C bond. Both individual tetracyclic subunits are nearly

Table 6.5.   Anisotropic Atomic Displacement Parameters (Å^2) of Non-hydrogen Atoms (Continued)

Atom	U^{11}	U^{22}	U^{33}	U^{12}	U^{13}	U^{23}
O1A	0.0241 (7)	0.0181 (7)	0.0148 (7)	0.0007 (6)	−0.0010 (5)	0.0013 (5)
O2A	0.0210 (8)	0.0343 (9)	0.0343 (9)	0.0041 (7)	−0.0043 (7)	−0.0110 (7)
O3A	0.0239 (8)	0.0415 (9)	0.0158 (7)	0.0114 (7)	−0.0029 (6)	−0.0009 (6)
C1A	0.0146 (9)	0.0168 (10)	0.0136 (9)	0.0037 (7)	0.0014 (7)	0.0010 (7)
C2A	0.0174 (9)	0.0155 (9)	0.0146 (9)	0.0027 (7)	0.0026 (7)	−0.0026 (7)
C3A	0.0185 (9)	0.0161 (10)	0.0233 (10)	0.0033 (8)	0.0061 (8)	−0.0017 (8)
C4A	0.0137 (9)	0.0159 (10)	0.0313 (11)	0.0032 (8)	0.0033 (8)	−0.0055 (8)
C5A	0.0161 (10)	0.0238 (11)	0.0308 (12)	0.0053 (8)	0.0013 (8)	−0.0109 (9)
C6A	0.0162 (9)	0.0264 (11)	0.0175 (10)	0.0093 (8)	−0.0002 (8)	−0.0039 (8)
C7A	0.0196 (10)	0.0232 (11)	0.0135 (9)	0.0100 (8)	0.0019 (7)	−0.0002 (8)
C8A	0.0181 (9)	0.0190 (10)	0.0145 (9)	0.0063 (8)	0.0027 (7)	−0.0004 (8)
C9A	0.0150 (9)	0.0160 (9)	0.0154 (9)	0.0052 (7)	0.0019 (7)	−0.0018 (7)
C10A	0.0142 (9)	0.0187 (10)	0.0159 (9)	0.0037 (7)	0.0013 (7)	−0.0028 (8)
C11A	0.0155 (9)	0.0148 (9)	0.0167 (9)	0.0029 (7)	0.0014 (7)	−0.0016 (7)
C12A	0.0157 (9)	0.0205 (10)	0.0166 (10)	0.0075 (8)	−0.0003 (7)	−0.0036 (8)
C13A	0.0141 (9)	0.0203 (10)	0.0253 (11)	0.0063 (8)	0.0000 (8)	−0.0076 (8)
C14A	0.0166 (9)	0.0245 (11)	0.0139 (9)	0.0086 (8)	−0.0006 (7)	−0.0036 (8)
C15A	0.0259 (11)	0.0192 (11)	0.0273 (11)	0.0008 (8)	0.0092 (9)	0.0012 (9)
C16A	0.0190 (10)	0.0215 (11)	0.0414 (13)	−0.0001 (8)	0.0033 (9)	0.0003 (10)
C17A	0.0257 (11)	0.0310 (12)	0.0172 (10)	0.0099 (9)	0.0009 (8)	0.0043 (9)
C18A	0.0210 (10)	0.0251 (11)	0.0185 (10)	0.0034 (8)	0.0040 (8)	0.0038 (8)
Cl1	0.0365 (3)	0.0235 (3)	0.0423 (3)	0.0051 (2)	0.0160 (3)	0.0086 (2)
Cl2	0.0280 (3)	0.0299 (3)	0.0350 (3)	0.0006 (2)	0.0079 (2)	−0.0095 (2)
C19	0.0209 (10)	0.0264 (12)	0.0328 (12)	0.0014 (9)	−0.0001 (9)	0.0017 (9)

Table 6.6.   Selected Interatomic Distances (Å) of Non-hydrogen Atoms

O1—C2	1.217 (2)	O1A—C2A	1.208 (2)
O2—C5	1.210 (2)	O2A—C5A	1.205 (2)
O3—C6	1.205 (2)	O3A—C6A	1.211 (2)
C1—C1A	1.369 (3)		
C1—C2	1.545 (3)	C1A—C2A	1.553 (3)
C1—C9	1.470 (2)	C1A—C9A	1.466 (3)
C2—C11	1.500 (2)	C2A—C11A	1.507 (3)
C3—C4	1.448 (3)	C3A—C4A	1.452 (3)
C3—C11	1.397 (3)	C3A—C11A	1.394 (3)
C3—C15	1.501 (3)	C3A—C15A	1.502 (3)
C4—C13	1.388 (3)	C4A—C13A	1.386 (3)
C4—C16	1.504 (3)	C4A—C16A	1.503 (3)
C5—C6	1.601 (3)	C5A—C6A	1.590 (3)
C5—C13	1.489 (3)	C5A—C13A	1.508 (3)
C6—C14	1.487 (2)	C6A—C14A	1.483 (3)
C7—C8	1.455 (2)	C7A—C8A	1.447 (3)
C7—C14	1.393 (3)	C7A—C14A	1.390 (3)
C7—C17	1.504 (3)	C7A—C17A	1.503 (3)
C8—C9	1.399 (3)	C8A—C9A	1.404 (3)
C8—C18	1.502 (3)	C8A—C18A	1.507 (3)
C9—C10	1.415 (3)	C9A—C10A	1.413 (3)
C10—C11	1.394 (3)	C10A—C11A	1.389 (3)
C10—C12	1.369 (2)	C10A—C12A	1.372 (3)
C12—C13	1.411 (3)	C12A—C13A	1.408 (3)
C12—C14	1.407 (3)	C12A—C14A	1.403 (3)
Cl1—C19	1.769 (2)	Cl2—C19	1.766 (2)

Table 6.7. Selected Bond Angles (°) of Non-hydrogen Atoms

C1A—C1—C2	121.11 (16)	C1—C1A—C2A	121.74 (16)
C1A—C1—C9	130.36 (17)	C1—C1A—C9A	128.93 (17)
C9—C1—C2	107.09 (15)	C9A—C1A—C2A	107.35 (15)
O1—C2—C1	125.78 (17)	O1A—C2A—C1A	126.17 (16)
O1—C2—C11	127.71 (18)	O1A—C2A—C11A	128.50 (18)
O2—C5—C6	122.48 (17)	O2A—C5A—C6A	122.96 (19)
O2—C5—C13	131.33 (18)	O2A—C5A—C13A	130.6 (2)
O3—C6—C5	122.29 (17)	O3A—C6A—C5A	122.96 (18)
O3—C6—C14	131.56 (19)	O3A—C6A—C14A	131.1 (2)
C3—C4—C16	119.67 (17)	C3A—C4A—C16A	119.99 (19)
C3—C11—C2	134.36 (17)	C3A—C11A—C2A	134.50 (18)
C4—C3—C15	120.00 (17)	C4A—C3A—C15A	120.57 (17)
C4—C13—C5	135.69 (17)	C4A—C13A—C5A	136.86 (18)
C4—C13—C12	120.16 (16)	C4A—C13A—C12A	119.78 (17)
C7—C8—C18	118.17 (17)	C7A—C8A—C18A	118.43 (17)
C7—C14—C6	135.84 (17)	C7A—C14A—C6A	135.27 (18)
C7—C14—C12	119.68 (16)	C7A—C14A—C12A	119.69 (17)
C8—C7—C17	120.13 (17)	C8A—C7A—C17A	119.78 (18)
C8—C9—C1	135.75 (17)	C8A—C9A—C1A	135.94 (17)
C8—C9—C10	118.30 (16)	C8A—C9A—C10A	118.45 (17)
C9—C8—C7	119.59 (17)	C9A—C8A—C7A	119.36 (18)
C9—C8—C18	122.17 (16)	C9A—C8A—C18A	122.13 (17)

planar (root mean square, or r.m.s., deviation of each fitted plane of 14 pyracene carbon atoms is

0.0539 Å and 0.0543 Å, respectively) and have four methyl groups and three carbonyl groups

attached to the peripheral carbons. The least-squares planes for the two halves of this highly

Table 6.7.   Selected Bond Angles (°) of Non-hydrogen Atoms (Continued)

C10—C9—C1	104.98 (16)	C10A—C9A—C1A	105.09 (16)
C10—C11—C2	104.74 (16)	C10A—C11A—C2A	105.24 (16)
C10—C11—C3	120.70 (16)	C10A—C11A—C3A	120.23 (17)
C10—C12—C14	120.52 (17)	C10A—C12A—C14A	120.61 (18)
C10—C12—C13	120.37 (17)	C10A—C12A—C13A	120.15 (19)
C11—C2—C1	106.15 (15)	C11A—C2A—C1A	105.05 (15)
C11—C3—C4	118.54 (17)	C11A—C3A—C4A	118.41 (18)
C11—C3—C15	121.45 (16)	C11A—C3A—C15A	121.03 (17)
C11—C10—C9	116.98 (16)	C11A—C10A—C9A	116.85 (16)
C12—C10—C11	120.79 (17)	C12A—C10A—C11A	121.38 (18)
C12—C10—C9	121.98 (17)	C12A—C10A—C9A	121.74 (18)
C12—C13—C5	104.14 (16)	C12A—C13A—C5A	103.36 (17)
C12—C14—C6	104.37 (16)	C12A—C14A—C6A	104.90 (17)
C13—C4—C3	119.39 (17)	C13A—C4A—C3A	119.75 (18)
C13—C4—C16	120.90 (17)	C13A—C4A—C16A	120.26 (18)
C13—C5—C6	106.18 (15)	C13A—C5A—C6A	106.45 (16)
C14—C6—C5	106.12 (15)	C14A—C6A—C5A	105.93 (16)
C14—C7—C8	119.45 (17)	C14A—C7A—C8A	119.88 (17)
C14—C7—C17	120.39 (16)	C14A—C7A—C17A	120.33 (17)
C14—C12—C13	119.07 (16)	C14A—C12A—C13A	119.23 (17)
Cl2—C19—Cl1	110.44 (11)		

conjugated molecule are twisted along the central C=C bond with a dihedral angle of 50.78 (3)°

at 90 K. A visual "side-view" ORTEP representation of this twist is shown in **Figure 6.3**.

The out-of-plane linear deviation of the methyl substituents from a least squares plane of

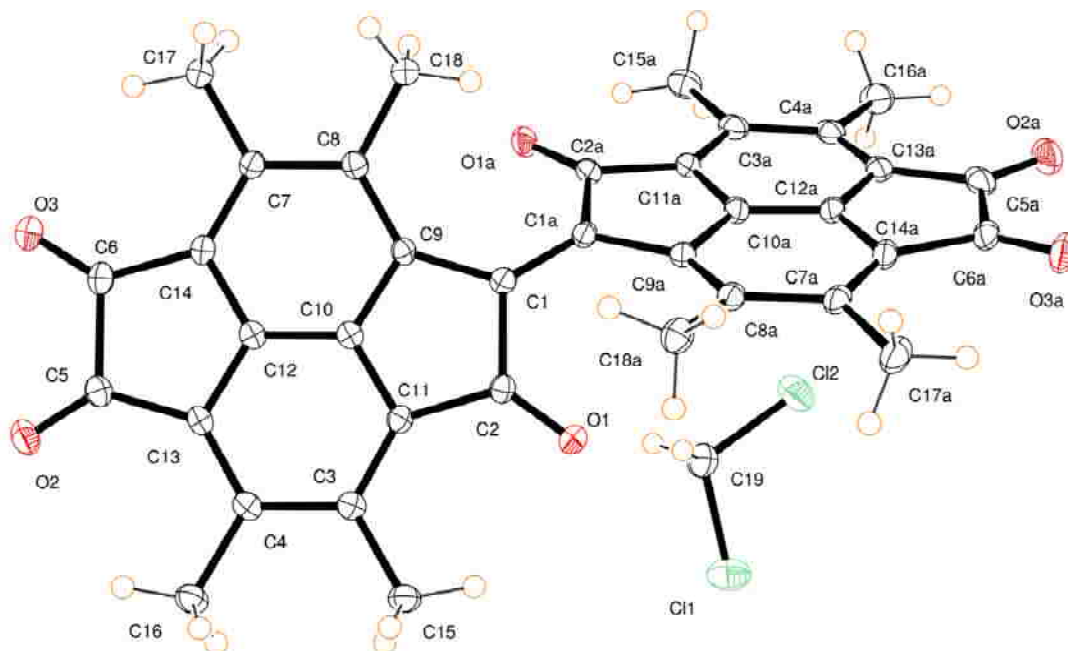the pyracene carbon atoms ranges from 0.029 (3) Å to 0.365 (3) Å. In comparison to another

Figure 6.2. ORTEP representation of the title molecule with 50% probability level atomic displacement ellipsoids at T = 90 K.
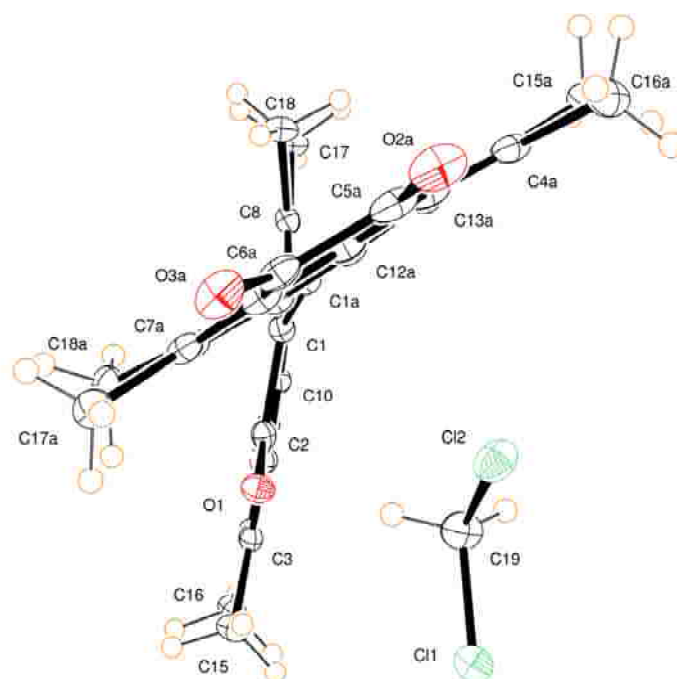

Figure 6.3. Side profile ORTEP representation showing dihedral angle between the two halves of the title molecule connected by the central C=C bond with 50% probability level atomic displacement ellipsoids at T = 90 K.

compound in the Cambridge Structural Database or CSD,[16] this range is below the maximum

substituent deviation reported for 1,4,5,6,7,10,11,12-octamethylindeno[1,2,3-*cd*]fluoranthene

(CSD Refcode NOTVAT, see **Figure 6.4a**) which is a fullerene fragment with 4 methyl groups

on the peripheral naphthalene carbons and 4 methyl groups on the peripheral phenyl carbons.[1]

The methyl carbons were reported to deviate up to 0.4 Å with respect to a fitted least squares

plane.

a)   b)

c)   d)
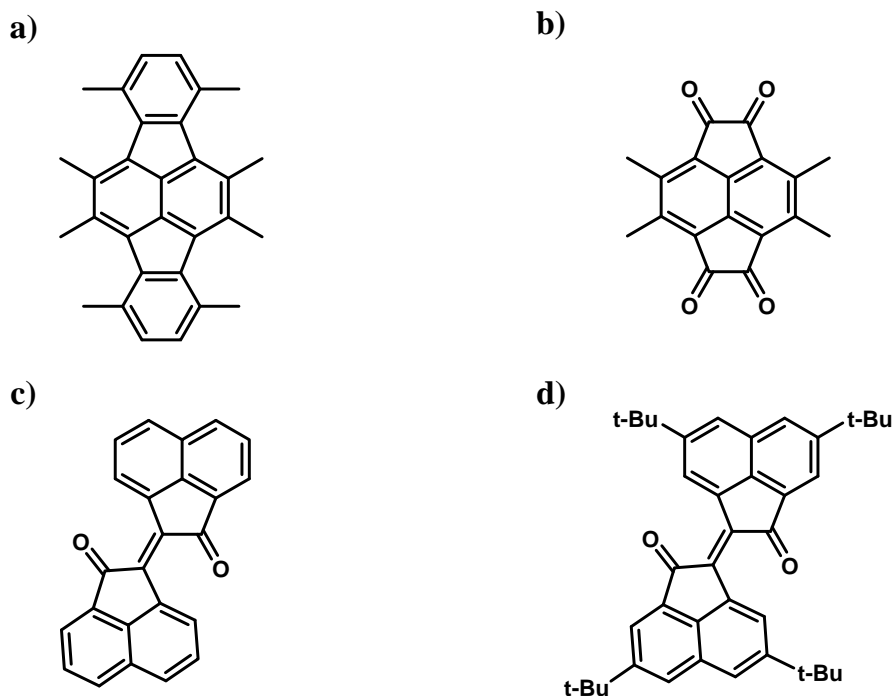
Figure 6.4. Structurally related compounds are compared to the title compound in this chapter during discussion of methyl substituent deviation, ring distortion, and longer than typical bond lengths. These structures are identified by the following CSD Refcodes: a) NOTVAT, b) YEHHAU, c) GOZNOY, and d) ITILEC.

For the planar distortion along the fused bond of one naphthalene subunit of the title

compound, a 6.69 (10)° dihedral angle is calculated between least squares planes of two *ortho*-

fused phenyl groups, C3—C4—C13—C12—C10—C11 (r.m.s. deviation of 0.0075 Å) and C7—

C8—C9—C10—C12—C14 (r.m.s. deviation of 0.0275 Å). For the other naphthalene subunit,

the dihedral angle, 1.53 (12)°, is much smaller between fitted planes of phenyl groups, C7A—C8A—C9A—C10A—C12A—C14A (r.m.s. deviation of 0.0193 Å) and C3A—C4A—C13A—C12A—C10A—C11A (r.m.s. deviation of 0.0226 Å).

The dihedral angle is 3.92 (12)° between two respective least squares planes of the 5-membered carbon rings C5—C6—C14—C12—C13 (r.m.s. deviation of 0.0137 Å) and C1—C2—C11—C10—C9 (r.m.s. deviation of 0.0105 Å) which are connected across the aromatic fused $C(sp^2)$—$C(sp^2)$ bond of the naphthalene framework. In a similar comparison to the other half of the compound, there is a significantly larger dihedral angle, 6.57 (14)°, between least squares planes defined by C1A—C2A—C11A—C10A—C9A (r.m.s. deviation of 0.0279 Å) and C5A—C6A—C14A—C12A—C13A (r.m.s. deviation of 0.0147 Å).

An examination of intermolecular carbonyl-carbonyl interactions[17] reveals the presence of antiparallel and parallel motifs (**Figure 6.5**), but not any perpendicular carbonyl arrangement. The C5a=O2a carbonyls interact with each other in an antiparallel fashion with a torsion angle of zero (C5a=O2a⋯C5a=O2a) and interatomic distance of 3.041 (3) Å (O2a⋯C5a). Two different carbonyls, C2a=O1a and C6a=O3a, pack in a parallel relative orientation with -179.65 (17)° torsion angle (C6a=O3a⋯C2a=O1a) and interatomic distance of 3.152 (2) Å (O3a⋯C2a). Close O⋯C contacts can also be observed among the remaining carbonyls, such as 3.085 (2) Å between O3⋯C5 and 3.431 (2) Å between O2⋯C2. However, the torsion angles for these interactions deviate significantly from the expected carbonyl-carbonyl torsion angles. C6=O3⋯C5=O2 is *pseudo*-antiparallel with a torsion angle 63.87 (17)° and C5=O2⋯C2=O1 is *pseudo*-parallel with a torsion angle -112.68 (16)°.

For every equivalent of the title compound, there is an equimolar amount of dichloromethane solvent. A close contacts between one of the solvent's Cl atoms and a carbonyl of the title compound has angles of 167.82 (8)° and 173.25 (15)° for the atoms C19—Cl2⋯O2a

and Cl2···O2a=C5a, respectively, and an interatomic distance between Cl2···O2a of 3.1328 (16) Å, which is less than the sum of the van der Waals radii[18] of 3.27 Å (r_O = 1.52 Å, r_{Cl} = 1.75 Å). The angles adopted for this halogen-carbonyl interaction are approaching 180°. The next closest interaction with a halogen and a carbonyl O atom is outside the calculated van der Waals sphere, Cl1···O3 of 3.4166 (16) Å, and deviates away from 180° with a C19—Cl1···O3 angle of 71.06 (8)° and Cl1···O3=C6 angle of 153.92 (13)°.

(a)   (b)
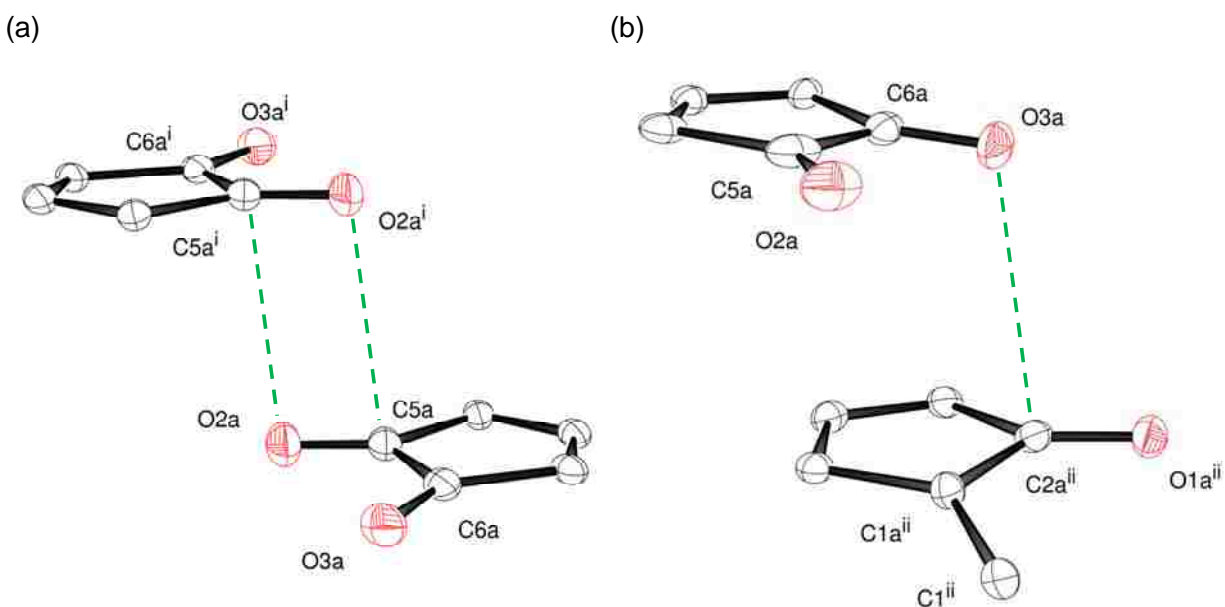
Figure 6.5.   Examples of (a) antiparallel and (b) parallel motifs of intermolecular carbonyl-carbonyl interactions within the crystal structure of this compound. Molecular fragments are shown with connecting dashed lines to help emphasize the difference in two orientations.

There are long C(sp^2)—C(sp^2) bond lengths between the carbonyl carbons with a C5—C6 bond length of 1.601 (3) Å and a C5A—C6A bond length of 1.590 (3) Å. These long bond lengths involve 5-membered carbon rings that are fused to a naphthalene framework. The angle between the 3 carbon atoms shared by the 5-membered carbon rings and the naphthalene rings

112

form angles (119.07 (16)° and 119.23 (17)° for C14—C12—C13 and C14A—C12A—C13A, respectively) that are closer to the angles observed in hexagons, 120°, instead of pentagons, 108°. The combination of a long bond length and the deviation in bond angles up to ~119° results in a significantly distorted, yet planar, ring.

An example of this type of ring distortion is found in the structure of 1,2,5,6 tetraketopyracene,[5] CSD Refcode YEHHAU (**Figure 6.4b**), which contains two $C(sp^2)$—$C(sp^2)$ bonds between carbonyl carbons that are both separated by 1.579 (9) Å based on diffraction data collected at T = 115 K. This example also has two enlarged bond angles; both measuring 119.2 (3)° between the fused carbons connecting the 5-membered carbon rings to the naphthalene framework. In the publication[5] containing the 1,2,5,6 tetraketopyracene crystal structure, calculation results were also published and are in good agreement with this structural elongation (using either the PM3 or *ab initio* method).

Also, there are long $C(sp^2)$—$C(sp^2)$ bond lengths of 1.545 (3) Å for the C1—C2 bond and 1.553 (3) Å for the C1A—C2A bond. These bond lengths are shorter than the bonds discussed in the previous paragraphs. This observation coincides with less bond angle distortion for the carbons in the 5-membered rings that are fused with the naphthalene subunit. The bond angles between fused bonds are 116.98 (16)° and 116.85 (16)° for C9—C10—C11 and C9A—C10A—C11A, respectively, and near the average of 120° (hexagon) and 108° (pentagon).

1,1'-bi(acenaphthen-1-ylidene)-2,2'-dione (CSD Refcode GOZNOY, **Figure 6.4c**) is structurally similar to the central part of the title compound. The bond distance for $C(sp^2)$—$C(sp^2)$ bond length between the carbonyl carbon and the carbon connecting the two acenaphthylen-1(2*H*)-one halves is 1.526 (3) Å at T = 295 K.[6] A derivative of this diketone compound with the addition of 4 tert-butyl groups (CSD Refcode ITILEC, **Figure 6.4d**) has a $C(sp^2)$—$C(sp^2)$ bond length of 1.532 (2) Å at T = 200 K.[7]

6.4   Conclusions

(*E*)-3,3',4,4',7,7',8,8'-octamethyl-2*H*,2'*H*-[1,1'-bi(cyclopenta[*fg*]acenaphthylenylidene)]-2,2',5,5',6,6'-hexaone is a highly conjugated organic compound with antiparallel and parallel motifs of intermolecular carbonyl-carbonyl interactions. Structural comparisons were made with this compound with other previously reported compounds. These comparisons demonstrate that the planarity of the fused rings, out-of-plane deviation of substituents, and longer than typical bond lengths are normal.

The most notable feature of this molecule is the twist along the central bond between two pyracene frameworks with an angle of 50.78 (3)° at 90 K. This twist is due to steric interactions near the central C=C bond between a peripheral methyl group on one half of the compound and a carbonyl on the other half (as shown in space-filling representation, **Figure 6.6**).
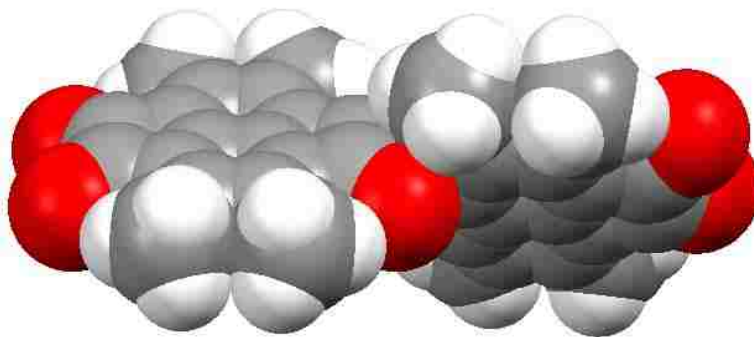

Figure 6.6.   Space-filling representation of the title molecule (red = oxygen, grey = carbon, white = hydrogen) showing the steric interaction between the molecule's two halves that are connected by a central C=C bond.

6.5   References

(1)   Sygula, A.; Fronczek, F. R.; Rabideau, P. W. *Tetrahedron Lett.* **1997**, *38*, 5095-5098.

(2)   Tsefrikas, V. M.; Scott, L. T. *Chem. Rev.* **2006**, *106*, 4868-4884.

(3)   Wu, Y. T.; Siegel, J. S. *Chem. Rev.* **2006**, *106*, 4843-4867.

(4)   Sygula, A. *Eur. J. Org. Chem.* **2011**, 1611-1625.

(5)   Abdourazak, A. H.; Marcinow, Z.; Folsom, H. E.; Fronczek, F. R.; Sygula, R.; Sygula, A.; Rabideau, P. W. *Tetrahedron Lett.* **1994**, *35*, 3857-3860.

(6)   Mehta, G.; Sarma, P.; Uma, R.; Pogodin, S.; Cohen, S.; Agranat, I. *J. Chem. Soc.-Perkin Trans. 1* **1999**, 1871-1876.

(7)   Kilway, K. V.; Lindgren, K. A.; Vincent, J. W.; Watson, J. A.; Clevenger, R. G.; Ingalls, R. D.; Ho, D. M.; Pascal, R. A. *Tetrahedron* **2004**, *60*, 2433-2438.

(8)   Nonius *COLLECT*; Delft, The Netherlands: Nonius BV, 2000.

(9)   Otwinowski, Z.; Minor, W. In *Methods in Enzymology*; Carter Jr., C. W., Sweet, R. M., Eds.; Academic Press Inc.: New York, 1997; Vol. 276, Macromolecular Crystallography, Part A, p 307-326.

(10)   Altomare, A.; Burla, M. C.; Camalli, M.; Cascarano, G. L.; Giacovazzo, C.; Guagliardi, A.; Moliterni, A. G. G.; Polidori, G.; Spagna, R. *J. Appl. Crystallogr.* **1999**, *32*, 115-119.

(11)   Sheldrick, G. M. *Acta Crystallogr. Sect. A* **2008**, *64*, 112-122.

(12)   Farrugia, L. J. *J. Appl. Crystallogr.* **1997**, *30*, 565.

(13)   Westrip, S. P. *J. Appl. Crystallogr.* **2010**, *43*, 920-925.

(14)   Farrugia, L. J. *J. Appl. Crystallogr.* **1999**, *32*, 837-838.

(15)   Spek, A. L. *J. Appl. Crystallogr.* **2003**, *36*, 7-13.

(16)   Allen, F. H. *Acta Crystallogr. Sect. B-Struct. Sci.* **2002**, *58*, 380-388.

(17)   Allen, F. H.; Baalham, C. A.; Lommerse, J. P. M.; Raithby, P. R. *Acta Crystallogr. Sect. B-Struct. Sci.* **1998**, *54*, 320-329.

(18)   Bondi, A. *J. Phys. Chem.* **1964**, *68*, 441-451.

CHAPTER 7

SYNTHESIS AND CHARACTERIZATION OF BIOCERAMICS:POLYMER COMPOSITE SCAFFOLDS FOR BONE TISSUE ENGINEERING

Tremble, for dire peril walks,
Monstrous acrimony's spurning mercy's laws.[1]
- Norman L. Bowen

7.1   Introduction

Regenerating bone that was either damaged by injury or disease is a major challenge in bone tissue engineering. A recent method for tissue regeneration is the development of a three-dimensional scaffolded architecture from materials that are both biocompatible and bioactive.[2] The development of scaffolded materials that will promote bone tissue regeneration requires a trade-off of various properties in order to produce a suitable implant. The scaffolds should be porous with pore diameter similar to actual bone (75 – 200 μm)[3-5] and deep interconnectivity between pores to allow cell penetration, flow of nutrients in and waste out for cell viability, and bone tissue growth within the scaffold interior which will help secure the scaffold to neighboring bone.[6] The material used for the scaffolds also need to be biodegradable in order to slowly free up space as the bone tissue grows. As the scaffold degrades, it is paramount that it releases bioactive ions (Ca, Mg, and Si)[7,8] that promote osteoblast proliferation[9-11] and calcified tissue mineralization[12] while not adversely increasing the acidity of the local environment.[13] However, the porous, biodegradeable scaffold needs to be mechanically robust to withstand compressive loads that are typical for the site of implantation.   Additionally, the material needs to be moldable so that the surgeon can form the implant to fit the desired location using minimal invasive surgery.[13,14]

Bioceramic scaffolds can be made to meet the porous and biodegradeable requirements. Due to their porosity and specific surface area, bioceramic scaffolds have also proven to be both

116

osteoinductive and osteoconductive materials under physiological conditions (20-40 °C, 6-9 pH, atmospheric pressure). Unfortunately, bioceramics do not have the desired mechanical properties for load bearing applications due to their intrinsic brittleness.[13,14]

To overcome the mechanical property issue, we developed several composites of bioceramic and polymeric materials. This chapter discusses the synthesis of these composites and summarizes preliminary results from experiments[15] using composites of akermanite ($Ca_2MgSi_2O_7$) and poly-ε-caprolactone (PCL, $-[C(=O)CH_2CH_2CH_2CH_2CH_2O]_n-$) that demonstrate a balance of desired properties can be achieved. The targeted synthesis of CaO-MgO-SiO$_2$ bioceramics will be covered for which merwinite ($Ca_3MgSi_2O_8$), monticellite ($CaMgSiO_4$), and diopside ($CaMgSi_2O_6$) will be evaluated in the near future for their potential incorporated into composites for tissue engineering application.

7.2   Experimental Details

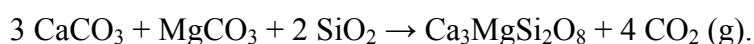### 7.2.1   Synthesis of Akermanite (Ceramic Method)

A detailed description of preparation of akermanite has been reported[15] and a brief description of the ceramic method is provided. Stoichiometric amounts of starting materials ($CaCO_3$, $MgCO_3$, and SiO_2) were weighed out for the synthesis of akermanite, $Ca_2MgSi_2O_7$. These reagents were mixed together and ground thoroughly in an agate mortar and pestle (5 minutes). After grinding, the powder mixture was pressed into a pellet and calcined at 950 °C for 48 hours to allow decarbonization. Multiple 48 hour heat treatments were then carried out at 1300 °C and furnace cooled (with grinding and reaction monitoring by powder X-ray diffraction in between heat treatments) until pure sample of akermanite was obtained indicating composition equilibrium of the following net reaction:

$$2 \; CaCO_3 + MgCO_3 + 2 \; SiO_2 \rightarrow Ca_2MgSi_2O_7 + 3 \; CO_2 \; (g).$$
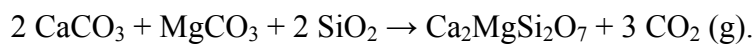
The required amount of 1300 °C heat treatment cycles was determined by proof of purity. This proof was provided in evaluation of the powder X-ray diffraction results.
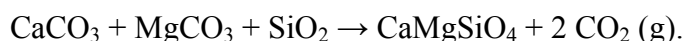
7.2.2 Synthesis of Merwinite (Ceramic Method)

Merwinite ($Ca_3MgSi_2O_8$) was synthesized by a similar ceramic method as used in Section 7.2.1 for akermanite. For this bioceramic material, the heat treatments are carried out at 1100 °C, instead of 1300 °C, after the initial decarbonation step. Also, the amount of starting materials was changed to match the desired product's stoichiometry – calcium carbonate (1.487 g, 14.9 mmol), magnesium carbonate (0.418 g, 5.0 mmol), and silicon dioxide (0.595 g, 9.9 mmol) – needed to produce a 2.5 g powder mixture for the following net reaction:

$$3\ CaCO_3 + MgCO_3 + 2\ SiO_2 \rightarrow Ca_3MgSi_2O_8 + 4\ CO_2\ (g).$$

7.2.3 Synthesis of Monticellite (Ceramic Method)

Monticellite ($CaMgSiO_4$) was synthesized with significant amount of akermanite impurities by a similar ceramic method as used in Section 7.2.1 for akermanite. The only changes in the procedure are the amount of starting materials – calcium carbonate (1.023 g, 10.2 mmol), magnesium carbonate (0.862 g, 10.2 mmol), and silicon dioxide (0.614 g, 10.2 mmol) – needed to produce a 2.5 g powder mixture for the following net reaction:

$$CaCO_3 + MgCO_3 + SiO_2 \rightarrow CaMgSiO_4 + 2\ CO_2\ (g).$$

7.2.4 Synthesis of Diopside (Ceramic Method)

Diopside ($CaMgSi_2O_6$) was synthesized by a similar ceramic method as used in Section 7.2.1 for akermanite. The only changes in the procedure are the amount of starting materials – calcium carbonate (0.822 g, 8.2 mmol), magnesium carbonate (0.692 g, 8.2 mmol), and silicon dioxide (0.986 g, 16.4 mmol) – needed to produce a 2.5 g powder mixture needed for the following net reaction:

$$CaCO_3 + MgCO_3 + 2SiO_2 \rightarrow CaMgSi_2O_6 + 2\ CO_2\ (g).$$
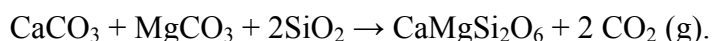
7.2.5 Characterization of Akermanite by Powder X-ray Diffraction

Phase identification and sample purity confirmation obtained using a Bruker D8 Advance powder X-ray diffractometer equipped with Cu Kα radiation source (λ = 1.54184 Å) and a germanium incident beam monochromator. Diffraction maxima (or peaks) were recorded at room temperature over a 2θ range of 15-60° (step size of 0.02° and step time of 2 sec). Experimental powder patterns were overlaid with calculated powder patterns.[15] The calculated patterns are based on single crystal data in the Inorganic Crystal Structure Database (ICSD). This single crystal data is the following ICSD reference codes: $Ca_2MgSi_2O_7$, akermanite, ICSD 26683;[16] $Ca_3MgSi_2O_8$, merwinite, ICSD 26002;[17] $CaMgSiO_4$, monticellite, ICSD 31106;[18] and $CaMgSi_2O_6$, diopside, ICSD 31116.[19]

7.2.6 Fabrication of Akermanite and β-TCP:HA Scaffolds

Scaffolds made with in-house prepared akermanite or commercially available 40:60 (wt%) β-tricalcium phosphate:hydroxyapapite (β-TCP:HA, Sigma-Aldrich) were prepared using the method previously described by Wu *et al.*[20] Briefly, this method involves: 1) creating a slurry by mixing ceramic powder with a polyvinyl alcohol aqueous solution (10 wt%); 2) completely saturating pieces of polyurethane foam (Scotch-Brite Scrub Sponge 74, 3M) templates with slurry; 3) drying the slurry-filled foam templates for 24 hours at 60 °C; 4) transferring the slurry-filled foam templates to a boat-shaped alumina crucible (see **Figure 7.1**); 5) burning away the foam template from the ceramic phase by heating up to 500 °C (after ramping the temperature up at rate of 50 °C/h) and dwelling for 5 hours; and 6) annealing for 3 hours at 1300 °C (using a ramp rate of 60 °C/h).[15]

7.2.8 Fabrication of PCL and Akermanite:PCL Composite Scaffolds

A 10 % PCL solution in 8 mL of 1,4-dioxane was prepared and akermanite was added at akermanite:PCL weight ratio of 0.0 g : 0.8 g (100 wt% PCL); 0.2 g : 0.6 g (25 wt% : 75 wt%

akermanite:PCL); 0.4 g : 0.4 g (50 wt% : 50 wt% akermanite:PCL); or 0.6 g : 0.2 g (75 wt% : 25 wt% akermanite:PCL) in a glass bottle. The mixtures were molded into 10 mm x 10 mm x 4 mm polydimethylsiloxane (PDMS) templates (Sylgard® 184 Silicone Elastomer Kit, Dow Corning), or into 17 mm x 10 mm glass cylinder vials. Composites (akermanite:PCL) and pure PCL solutions were immediately frozen with liquid nitrogen with a drop ratio of 1 inch/hour using a unidirectional thermally induced phase separation technique over 2 hours (10 mm x 10 mm x 10 mm cylinders) or frozen at -80 °C overnight (10 mm x 10 mm x 4 mm discs). After freezing, the samples were immediately incubated in a freeze-drier for 48 hours.[15]

Figure 7.1. Mixtures of bioceramic and polymeric materials are converted to a slurry, mixed with polyurethane foam, and then annealed to produce a porous material. The scaffolded product (prior to annealing) is shown in a boat-shaped alumina crucible.

7.3   Results and Discussion

7.3.1   Bioceramic Products and Evaluation by Powder X-ray Diffraction

In the early stages of this project, we attempted to synthesis akermanite ($Ca_2MgSi_2O_7$) by Wu and Chang's published sol-gel method.[21] Briefly, this method involves: 1) hydrolyzing tetraethyl orthosilicate [$(C_2H_5O)_4Si$] in aqueous solution for 30 min to produce SiO_2; 2) adding magnesium nitrate hexahydrate [$Mg(NO_3)_2 \cdot 6H_2O$] and calcium nitrate tetrahydrate [$Ca(NO_3)_2 \cdot 4H_2O$] to this solution and stirring for 5 hours at room temperature; 3) heating the

solution for 24 hours at 60 °C; 4) increasing the temperature up to 120 °C and heating for 48 hours to produce a dry gel; 5) grinding up gel thoroughly using an agate mortar and pestle; and 6) placing the gel in a boat-shaped alumina crucible and annealing at 1300 °C for 3 hours. The sol-gel method resulted in a mixture of two phases, akermanite and merwinite, as observed in the powder X-ray diffraction pattern (**Figure 7.2a**). Diffraction maxima (or peaks) can be matched with calculated powder X-ray diffraction patterns of akermanite (**Figure 7.2b**) and merwinite (**Figure 7.2c**) based on crystallographic data obtained in the ICSD. Even with multiple heat treatments at 1300 °C with intermittent grinding, the merwinite phase could not be removed.
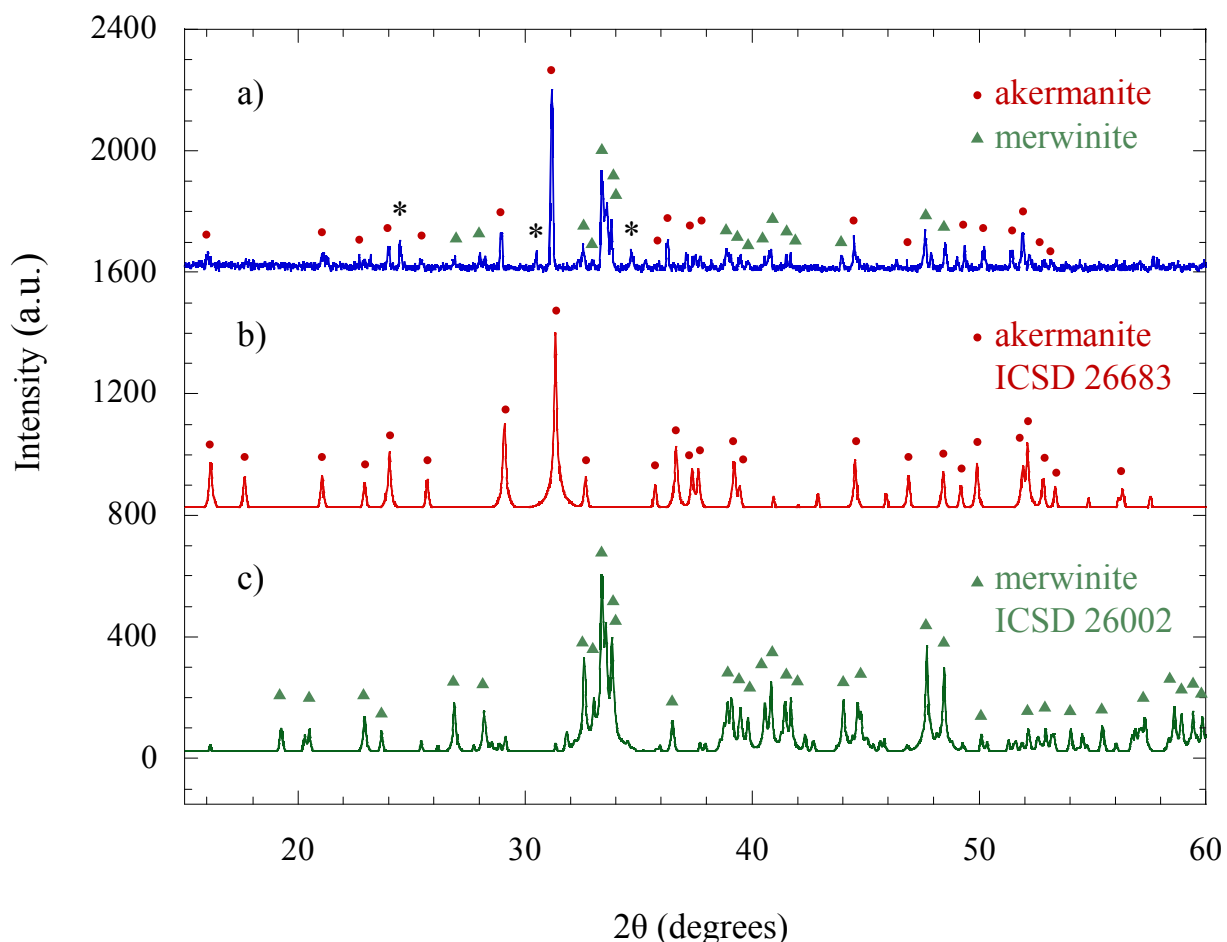

Figure 7.2.   (a) The sol-gel method resulted in a mixture of akermanite and merwinite as shown in the experimental powder X-ray diffraction pattern. For comparison, calculated powder X-ray diffraction patterns of (b) ICSD 26683 for akermanite and (c) ICSD 26002 merwinite are also provided.

121

A mixture of ceramic phases is not a problem because recent studies with merwinite demonstrated that it also promotes osteogenesis and bone regeneration.[22,23] It was only removed in order to study the intrinsic osteogenic and mechanical properties of the akermanite phase. Promising results were discovered in mixtures of two or more biocompatible materials. One of these examples is a study with a multiphase mixture of three compounds (akermanite, merwinite, and dicalcium silicate) doped with a small amount (1 and 2 wt%) of boron dioxide.[24] However, to better understand the contribution of a particular ceramic material in the bone regeneration process required a single phase.

Our synthetic efforts then switched to a ceramic method approach using $CaCO_3$, $MgCO_3$, and SiO_2 as starting materials. After mixing these materials and an initial heat treatment at 950 °C to form CaO and MgO by decarbonation, the first heat treatment at 1300 °C would generate two predominant mineralogical phases, akermanite and merwinite. However, with 2-3 more heat treatments at 1300 °C, the merwinite phase was eventually removed and only akermanite remained (**Figure 7.3a**).

Due to the vast improvement demonstrated by the ceramic method in producing synthetic akermanite, this method was extended to other related $CaO-MgO-SiO_2$ phases. For merwinite, single phase results were achieved when heat treatments are carried out at 1100 °C, instead of 1300 °C, after the decarbonation step (**Figure 7.3b**). Experiments at higher reaction temperatures (such as 1300 °C) resulted in the formation of a secondary phase (akermanite) which could not be removed by further heat treatments once it was formed.

Single phase monticellite could not be achieved from multiple heat treatments at 1300 °C (attempted up to four 24 hour heat treatments). Akermanite was always present as a secondary phase (**Figure 7.3c**). Higher temperature heat treatments are needed (based on previously
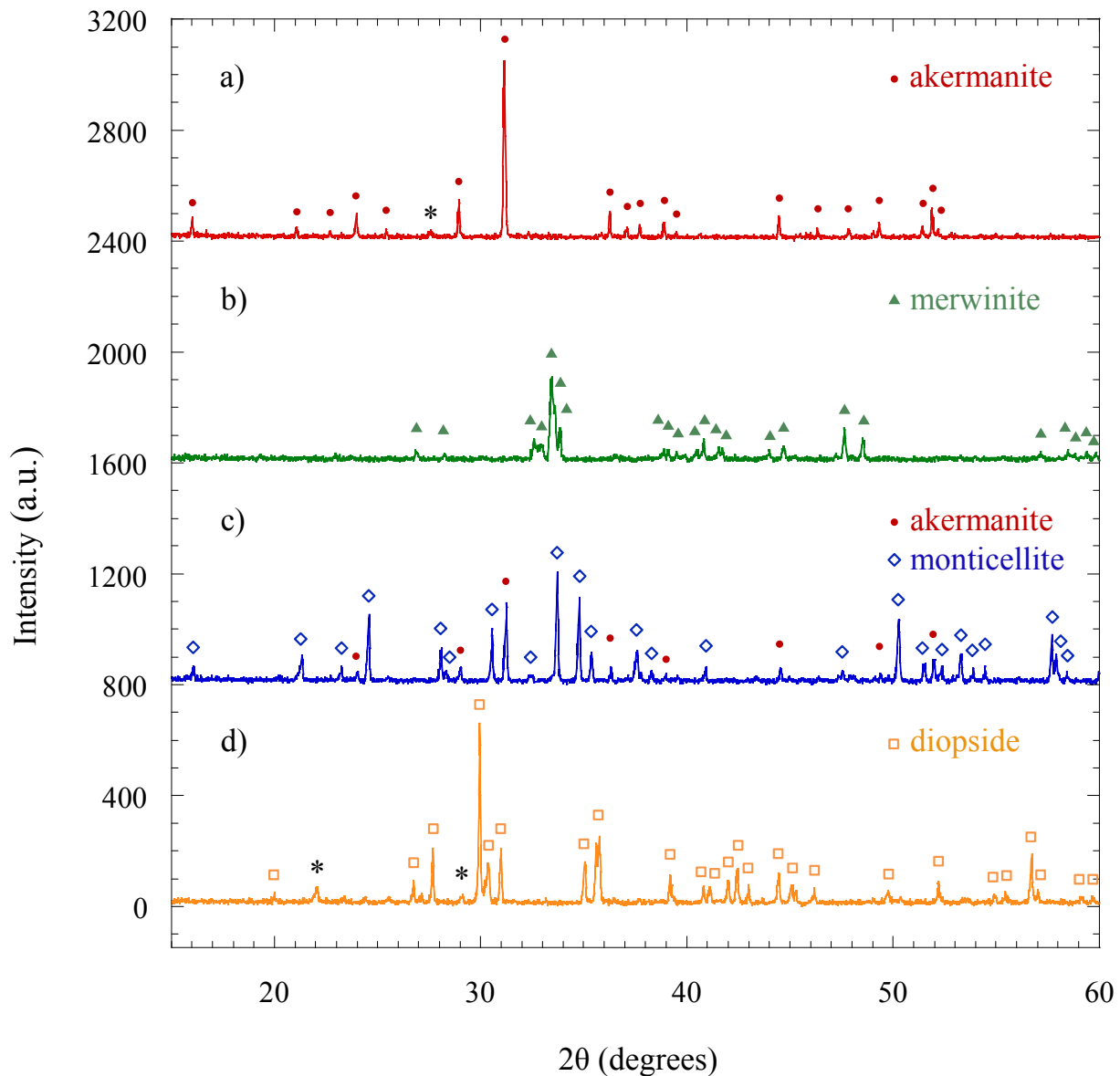
Figure 7.3. Powder X-ray diffraction patterns of the following synthetic bio-ceramic materials: (a) akermanite, (b) merwinite, (c) mixture of akermanite and monticellite, and (d) diopside.

reported synthesis at 1480 °C)[25] to produce monticellite as the only phase present. However, higher temperatures are above the normal operating temperature range for our furnaces.

Diopside was synthesized using the same heat treatment temperature as akermanite (1300 °C), diopside can be made with small unidentified impurities (**Figure 7.3d**). Fine tuning of the reaction temperature profile needed for this ceramic phase in order to obtain higher phase purity.

7.3.2 Results of Scaffold Morphology Characterization, *In Vitro* Experiments

A detailed scaffold characterization and *in vitro* experiments with human adipose-derived stem cell (hASC) loaded scaffolds, which are fully described in a recent dissertation.[26] The main conclusions drawn from this work are that scaffolds containing a mixture of PCL and akermanite had significantly higher porosity (~1.5x), higher compression strength (~3x), comparable hASC viability, comparable alkaline phosphatase (ALP, early osteogenic marker) expression, comparable osteocalcin (OCN, indicator of mature osteoblast differentiation) expression, comparable interleukin-6 (Il-6, indicator of proinflammatory upregulation) expression, lower pore size (~0.4x), and lower degradation rates (~0.8x) than the scaffolds containing only ceramic material. Overall, the 75:25 akermanite:PCL scaffolds showed the best characteristics and osteogenic response for a scaffold designed for bone tissue regeneration when combined with hASC.[15]

7.4 Conclusions

A series of scaffolds that are either ceramic, polymeric, or a combination of both were achieved by using ceramic methods. Composites of akermanite and PCL proved to be better candidates for bone tissue regeneration than scaffolds containing only ceramic or only polymeric material.[15] Furthermore, this study demonstrates that the compressive strength of scaffolds can be improved significantly with the addition of polymeric material (4.59 ± 0.41 MPa for 75:25 akermanite:PCL scaffold and 1.59 ± 0.41 MPa for akermanite scaffold) without adversely affecting the regenerative properties of the bioceramic material.[15] (For reference, the compressive strength of compact bone is 131-224 MPa and trabecular bone is 5-10 MPa.)[27]

Future studies will involve other related CaO-MgO-SiO$_2$ bioceramics, such as merwinite (Ca$_3$MgSi$_2$O$_8$), monticellite (CaMgSiO$_4$), and diopside (CaMgSi$_2$O$_6$), in scaffolded composites.

7.5   References

(1)   Bowen, N. L. *J. Geol.* **1940**, *48*, 225-274.

(2)   Haimi, S.; Suuriniemi, N.; Haaparanta, A. M.; Ella, V.; Lindroos, B.; Huhtala, H.; Raty, S.; Kuokkanen, H.; Sandor, G. K.; Kellomaki, M.; Miettinen, S.; Suuronen, R. *Tissue Eng. Part A* **2009**, *15*, 1473-1480.

(3)   Hulbert, S. F.; Young, F. A.; Mathews, R. S.; Klawitter, J. J.; Talbert, C. D.; Stelling, F. H. *J. Biomed. Mat. Res.* **1970**, *4*, 433-456.

(4)   Story, B. J.; Wagner, W. R.; Gaisser, D. M.; Cook, S. D.; Rust-Dawicki, A. M. *Int. J. Oral Maxillofac. Implants* **1998**, *13*, 749-757.

(5)   Reichert, J. C.; Hutmacher, D. W. In *Tissue Engineering*; Pallua, N., Suscheck, C. V., Eds.; Springer: USA, 2011, p 431-456.

(6)   Lawrence, B. J.; Madihally, S. V. *Celll Adhes. Migr.* **2008**, *2*, 9-16.

(7)   Liu, Q. H.; Cen, L.; Yin, S.; Chen, L.; Liu, G. P.; Chang, J.; Cui, L. *Biomaterials* **2008**, *29*, 4792-4799.

(8)   Gu, H. J.; Guo, F. F.; Zhou, X.; Gong, L. L.; Zhang, Y.; Zhai, W. Y.; Chen, L.; Cen, L.; Yin, S.; Chang, J.; Cui, L. *Biomaterials* **2011**, *32*, 7023-7033.

(9)   Xynos, I. D.; Edgar, A. J.; Buttery, L. D. K.; Hench, L. L.; Polak, J. M. *J. Biomed. Mater. Res.* **2001**, *55*, 151-157.

(10)   Valerio, P.; Pereira, M. M.; Goes, A. M.; Leite, M. F. *Biomaterials* **2004**, *25*, 2941-2948.

(11)   Wu, C.; Chang, J.; Ni, S.; Wang, J. *J. Biomed. Mater. Res. A* **2006**, *76*, 73-80.

(12)   LeGeros, R. Z. In *Monographs in Oral Science* 1991; Vol. 15, p 1-201.

(13)   Dorozhkin, S. V. *J. Funct. Biomater.* **2010**, *1*, 22-107.

(14)   van Gaalen, S.; Kruyt, M.; Meijer, G.; Mistry, A.; Mikos, A.; van den Beucken, J.; Jansen, J.; de Groot, K.; Cancedda, R.; Olivo, C.; Yaszemski, M.; Dhert, W. In *Tissue Engineering*; Blitterswijk, C., Hubbel, J., Eds.; Academic Press: London, UK, 2008, p 559-610.

(15)   Zanettii, A. S.; McCandless, G. T.; Chan, J. Y.; Gimble, J.; Hayes, D. J. *J. Tissue Eng. Regen. Med.* **2012**, Accepted for publication.

(16)   Warren, B. E. *Z. Kristall.* **1930**, *74*, 131-138.

(17)   Moore, P. B.; Araki, T. *Am. Miner.* **1972**, *57*, 1355-1374.

(18)   Brown, G. B.; West, J. *Z. Kristall.* **1927**, *66*, 154-161.

(19)   Warren, B.; Bragg, W. L. *Z. Kristall.* **1928**, *69*, 168-193.

(20)   Wu, C. T.; Chang, J. A.; Zhai, W. Y.; Ni, S. Y.; Wang, J. Y. *J. Biomed. Mater. Res. Part B* **2006**, *78*, 47-55.

(21)   Wu, C. T.; Chang, J. *Mater. Lett.* **2004**, *58*, 2415-2417.

(22)   Ou, J.; Kang, Y. Q.; Huang, Z. B.; Chen, X. C.; Wu, J.; Xiao, R. C.; Yin, G. F. *Biomed. Mater.* **2008**, *3*, 015015.

(23)   Chen, X. C.; Ou, J.; Wei, Y.; Huang, Z. B.; Kang, Y. Q.; Yin, G. F. *J. Mater. Sci. Mater. Med.* **2010**, *21*, 1463-1471.

(24)   Chen, X. C.; Wei, Y.; Huang, Z. B.; Kang, Y. Q.; Yin, G. F. *J. Mater. Res.* **2008**, *23*, 2873-2879.

(25)   Chen, X.; Ou, J.; Kang, Y.; Huang, Z.; Zhu, H.; Yin, G.; Wen, H. *J. Mater. Sci.: Mater. Med.* **2008**, *19*, 1257-1263.

(26)   Zanetti, A. S. Dissertation, Louisiana State University, 2011.

(27)   Yaszemski, M. J.; Payne, R. G.; Hayes, W. C.; Langer, R.; Mikos, A. G. *Biomaterials* **1996**, *17*, 175-185.

CHAPTER 8

CONCLUDING REMARKS

My first exposure to crystallography began as an organic chemist working on sterically hindered unnatural amino acid derivatives – compounds that would later be incorporated into peptide inhibitors of the aggregation process linked to Alzheimer's disease.[1] While purifying one of my dibenzylated intermediates by crystallization, I grew the large, beautiful crystals shown below (**Figure 8.1**). With these crystals, I was amazed by the amount of structural information that one could obtain from single crystal X-ray diffraction compared to other analytical techniques, such as NMR, MS, and IR. I knew very little about single crystal diffraction – a tragedy resulting from a lack of crystallography education and training in most undergraduate and graduate curricula.[2,3] Fortunately, I was encouraged by our staff crystallographer, Dr. Frank Fronczek, to learn how to select suitable crystals, collect diffraction data, and solve structures. This encouragement would lead to my growing interest in crystallography and, ultimately, to my involvement in the collaborative, multi-disciplinary projects described in this dissertation.

Figure 8.1.   Single crystals of ethyl 2-benzyl-2-nitro-3-phenylpropanoate which were synthesized by the dialkylation on the alpha carbon of ethyl nitroacetate with benzyl bromide under basic conditions (adapted from McCandless, G. T. Thesis, Louisiana State University, 2008).[1]

In the first project discussed in this dissertation, four refined models were developed and carefully evaluated by refinement statistics and chemical reasoning during the structure determination of $Yb_2Pd_3Ga_9$. Of these models, an orthorhombic *Cmcm* model with translational disorder provides the best fit to the data. Although a large number of 2-3-9 ternary phases adopt an ordered $Y_2Co_3Ga_9$ structure-type, there are two structural examples in literature, $Ho_2Rh_3Al_9$ and $Er_2Ir_3Al_9$, where similar unexpected disorder occurs and makes the refinement very difficult with misleading *pseudo*-hexagonal symmetry.

In the case of doped $CaFe_4As_3$, dopants, such as P, Yb, Co, and Cu, had a significant impact on the magnetic transition temperatures even when the doping concentration is small (below the limits of detection by X-ray) and the structural changes are barely (or, in some case, not) statistically significant. Compared to the undoped $CaFe_4As_3$ compound, Co doping had the largest effect in terms of suppressing the magnetic transitions (the first transition temperature, T_N, dropped from ~88 K to ~65 K and the second transition temperature, T_2, was suppressed below 2 K) and decreasing the unit cell volume (shrinks by 1.2%).

$Sr_3Ru_2O_7$ was best modeled in the tetragonal space group $I4/mmm$ using a split occupancy method for the equatorial oxygens. The maximum RuO_6 octahedral rotation of ~7° at room temperature is in excellent agreement with previous structural studies. Thermal cycling experiments did not reveal a systematic increase in the lattice c/a ratio as previously reported. However, systematic Mn-doping samples demonstrated an octahedral realignment from the Ru end-member, $Sr_3Ru_2O_7$, to the Mn end-member, $Sr_3Mn_2O_7$, where the octahedral rotation decreases as a function of doping concentration, x, and is absent when x is ~15% at room temperature. Also, interesting Bragg angle similarities are observed in the X-ray powder diffraction patterns between two different Ruddlesden-Popper phases, $Sr_3(Ru_{1-x}Mn_x)_2O_7$ and $Sr_4(Ru_{1-x}Mn_x)_3O_{10}$. It is only by careful examination of the *hkl* reflections that the phases can be

128

barely distinguished. The structure difference, however, between the two phases is unequivocally determined by single crystal diffraction experiments.

A thorough analysis of an iron corrole structure revealed an interesting crystal packing relationship between two independent complexes with an unusually short O···O distance between axial nitrosyl ligands. This corrole is part of a series of compounds for which both the understanding of regioselectivity of β-substitution and the influence of substitution patterns on the electrochemical properties are important for design of various chemical sensors. Unexpected substitution with a Co corrole was discovered where di-nitro substitution occurred at β-carbons on the "A" and "C" pyrrole rings, instead of the expected "A" and "D" rings. Future oxidation-reduction experiments are needed on this antipodal complex to determine the ramifications of this substitution pattern on the electrochemical properties.

Shifting to another structure determination project, the refinement of a highly conjugated side product revealed an interesting dimerization of two planar, fused-carbon ring moieties that are twisted by ~51° along a C=C bond which, considering the significant amount of twist, would be expected to be longer than 1.369 (3) Å. It is of interest in the design of fullerene fragments to understand from the elucidated structure how (mechanistically) this minor product was formed and to determine how to avoid or promote the formation of this discrete organic molecule.

Promising *in vitro* results with a scaffolded composite of akermanite and poly-ε-caprolactone (75:25 wt%) loaded with human adipose-derived stem cells (hASC) demonstrate that the mechanical properties of bioceramics can be improved with the addition of a polymeric phase without compromising the regenerative properties desired for bone tissue growth. Ceramic methods were developed for akermanite that have also shown potential in the synthesis of other related CaO-MgO-SiO_2 phases. In our experience, this method has also proven to be better than the sol-gel method. Future studies will involve other related Ca-Mg-Si-O

bioceramics, such as merwinite ($Ca_3MgSi_2O_8$), monticellite ($CaMgSiO_4$), and diopside ($CaMgSi_2O_6$), in scaffolded composites.

This series of projects clearly demonstrates the importance of crystallography in several different research areas. Unfortunately, the current trend demonstrates neglect in the educational training of the next generation of crystallographers and a growing misconception that structure determination is now an automated "black-box" technique requiring little human decision-making.[4] Just as crystal structures are constructed (**Figure 8.2**) and solved by using established chemical knowledge (such as bonding theories, coordination and site preferences, intermolecular forces, structural trends obtained from crystallographic databases, and results from other complementary analytical techniques), research advances occur by building on the major scientific advances made in the past. This is as true today as it was in 1912 when Bragg established his famous equation on the foundation laid by the work of others, such as Röntgen, Miller, and Laue. It is essential that universities continue to train students in crystallography so that the structural determination advances made so far will continue to foster new award-winning discoveries and a better understanding of unusual phenomena.

unit cell

Figure 8.2.   Building the structure of a crystal with unit cells (as obtained from Pynn, R. *Los Alamos Science* **1990**, 1-31).[5]

8.1 References

(1)   McCandless, G. T. Thesis, Louisiana State University, 2008.

(2)   Kantardjieff, K. A.; Kaysser-Pyzalla, A. R.; Spadon, P. *J. Appl. Crystallogr.* **2010**, *43*, 1137-1138.

(3)   Kantardjieff, K. A.; Lind, C.; Ng, J.; Santarsiero, B. D. *J. Appl. Crystallogr.* **2010**, *43*, 1181-1188.

(4)   Dauter, Z.; Jaskolski, M. *J. Appl. Crystallogr.* **2010**, *43*, 1150-1171.

(5)   Pynn, R. *Los Alamos Science* **1990**, 1-31.

APPENDIX - CONSENT POLICIES

American Chemical Society:

American Chemical Society's Policy on Theses and Dissertations

**If your university requires you to obtain permission, you must use the RightsLink permission system.
See RightsLink instructions at http://pubs.acs.org/page/copyright/permissions.html.**

This is regarding request for permission to include **your** paper(s) or portions of text from **your** paper(s) in your thesis. Permission is now automatically granted; please pay special attention to the **implications** paragraph below. The Copyright Subcommittee of the Joint Board/Council Committees on Publications approved the following:

Copyright permission for published and submitted material from theses and dissertations
ACS extends blanket permission to students to include in their theses and dissertations their own articles, or portions thereof, that have been published in ACS journals or submitted to ACS journals for publication, provided that the ACS copyright credit line is noted on the appropriate page(s).

Publishing **implications** of electronic publication of theses and dissertation material
Students and their mentors should be aware that posting of theses and dissertation material on the Web prior to submission of material from that thesis or dissertation to an ACS journal <u>may</u> affect publication in that journal. Whether Web posting is considered prior publication may be evaluated on a case-by-case basis by the journal's editor. If an ACS journal editor considers Web posting to be "prior publication", the paper will not be accepted for publication in that journal. If you intend to submit your unpublished paper to ACS for publication, check with the appropriate editor prior to posting your manuscript electronically.

Reuse/Republication of the Entire Work in Theses or Collections: Authors may reuse all or part of the Submitted, Accepted or Published Work in a thesis or dissertation that the author writes and is required to submit to satisfy the criteria of degree-granting institutions. Such reuse is permitted subject to the ACS' "Ethical Guidelines to Publication of Chemical Research" (http://pubs.acs.org/page/policy/ethics/index.html); the author should secure written confirmation (via letter or email) from the respective ACS journal editor(s) to avoid potential conflicts with journal prior publication*/embargo policies. Appropriate citation of the Published Work must be made. If the thesis or dissertation to be published is in electronic format, a direct link to the Published Work must also be included using the ACS Articles on Request author-directed link – see http://pubs.acs.org/page/policy/articlesonrequest/index.html

* Prior publication policies of ACS journals are posted on the ACS website at
http://pubs.acs.org/page/policy/prior/index.html

If your paper has **not** yet been published by ACS, please print the following credit line on the first page of your article: "Reproduced (or 'Reproduced in part') with permission from [JOURNAL NAME], in press (or 'submitted for publication'). Unpublished work copyright [CURRENT YEAR] American Chemical Society." Include appropriate information.

If your paper has already been published by ACS and you want to include the text or portions of the text in your thesis/dissertation, please print the ACS copyright credit line on the first page of your article: "Reproduced (or 'Reproduced in part') with permission from [FULL REFERENCE CITATION.] Copyright [YEAR] American Chemical Society." Include appropriate information.

Submission to a Dissertation Distributor: If you plan to submit your thesis to UMI or to another dissertation distributor, you should not include the unpublished ACS paper in your thesis if the thesis will be disseminated electronically, until ACS has published your paper. After publication of the paper by ACS, you may release the <u>entire</u> thesis (**not the individual ACS article by itself**) for electronic dissemination through the distributor; ACS's copyright credit line should be printed on the first page of the ACS paper.

10/10/03, 01/15/04, 06/07/06, 04/07/10, 08/24/10, 02/28/11

American Physical Society:

APS Copyright Policies and Frequently Asked Questions

- What is Copyright?
- What does copyright protect?
- How is a copyright different from a patent or a trademark?
- What is the difference between copyright infringement and plagiarism?
- Why should I transfer copyright to APS?
- Why should I transfer copyright to APS before the article is accepted for publication by an APS journal?
- Does transferring copyright affect my patent rights?
- As the author of an APS-published article, may I post my article or a portion of my article on my own website?
- What happens if the author has posted an APS-published article on a free access e-print server or on the authors' or institutions' web pages and subsequently a fee is imposed for access to those sites?
- As the author of an APS-published article, may I post my article or a portion of my article on an e-print server?
- As the author of an APS-published article, can I post my article or a portion of my article on a web resource like wikipedia or quantiki?
- As the author of an APS-published article, will I hold copyright to a "derived work", as described above, even if the original article was published prior to 1 October 2008?
- As the author (or the author's employer) of an APS-published article, may I use copies of part or all of my articles in the classroom?
- As the author of an APS-published article, may I use figures, tables, graphs, etc. in future publications?
- As the author of an APS-published article, may I include my article or a portion of my article in my thesis or dissertation?
- As the author of an APS-published article, may I give permission to a colleague or third party to republish all or part of the article in a print publication?
- As the author of an APS-published article, may I give permission to a colleague or third party to republish all or part of the article in an online journal, book, database compilation, etc.?
- As the author of an APS-published article, may I provide a PDF of my paper to a colleague or third party?
- As a third party (not an author), may I republish an article or portion of an article published by APS?
- As a third party, may I use articles published by APS for lecture and classroom purposes?
- How do I request permission to republish APS-copyrighted material?
- How do I provide a proper bibliographic citation and notice of the APS copyright?
- Copyright Transfer Form

What is copyright? http://www.copyright.gov/
Copyright is a form of legal protection for original works of authorship. Copyright covers both published and unpublished works.

What does copyright protect?
Copyright, a form of intellectual property law, protects original works of authorship including literary, dramatic, musical, and artistic works, such as poetry, novels, movies, songs, computer software, and architecture. Copyright does not protect facts, ideas, systems, or methods of operation, although it may protect the way these things are expressed. See Circular 1, Copyright Basics, section "What Works Are Protected", see http://www.copyright.gov/circs/circ1.html#wwp

How is a copyright different from a patent or a trademark?
Copyright protects original works of authorship, while a patent protects inventions or discoveries. Ideas and discoveries are not protected by the copyright law, although the way in which they are expressed may be. A trademark protects words, phrases, symbols, or designs identifying the source of the goods or services of one party and distinguishing them from those of others.

What is the difference between copyright infringement and plagiarism?
Copyright infringement occurs when an author's work is reused or republished without the permission of the copyright owner, whether or not author attribution accompanied the reuse.

Plagiarism occurs when an author's work has been reused or republished in such a manner as to make it appear as someone else's work, e.g., without quotation marks and citation of the original work.

Why should I transfer copyright to APS?
Like many other scientific publishers, the American Physical Society (APS) requires authors or their employers to provide transfer of copyright prior to publication. This permits APS to publish the article and to defend against improper use (or even theft) of the article. It also permits APS to mount the article online and to use the article in other forms or media, such as PROLA. By the APS transfer agreement, authors and their employers retain substantial rights in the work, as specified in the agreement (http://forms.aps.org/author/copytmsfr.pdf) and discussed in this document.

Why should I transfer copyright to APS before the article is accepted for publication by an APS journal?
Transferring copyright early in the process avoids the possibility of delaying publication if the transfer has to be obtained later in the process. By the terms of the copyright transfer agreement itself, it has no effect until the paper is accepted by an APS journal. The author retains the

copyright until acceptance, and has the full freedom, for example, to withdraw the paper from consideration by an APS journal and submit it elsewhere.

Does transferring copyright affect my patent rights?

No. Copyright is separate from any patent rights, and the APS transfer agreement specifically states that patent rights are not affected. However, you should be aware that submitting a manuscript to a journal without first taking steps to protect your patent rights (e.g., filing for a patent) could endanger those rights. Consult your patent attorney.

As the author of an APS-published article, may I post my article or a portion of my article on my own website?

Yes, the author or the author's employer may use all or part of the APS published article, including the APS-prepared version (e.g., the PDF from the online journal) without revision or modification, on the author's or employer's website as long as a fee is not charged. If a fee is charged, then APS permission must be sought. In all cases, the appropriate bibliographic citation and notice of the APS copyright must be included.

What happens if the author has posted an APS-published article on a free access e-print server or on the authors' or institutions' web page and subsequently a fee is imposed for access to those sites?

When a fee is imposed, the author must either obtain permission from APS or withdraw the article from the e-print server or Institutional Repository.

As the author of an APS-published article, may I post my article or a portion of my article on an e-print server?

The author has the right to post and update the article on a free-access e-print server using files prepared and formatted by the author. Any such posting made or updated after acceptance of the article for publication by APS shall include a link to the online abstract in the APS journal or to the entry page of the journal. In all cases, the appropriate bibliographic citation and notice of the APS copyright must be included. If the author wishes to use the APS-prepared version (e.g., the PDF from the online journal) on an e-print server other than authors' or employer's website, then APS permission must be sought. Similarly, if the author wishes to post the article (any version) on an e-print server that charges a fee for use, APS permission must be sought.

As the author of an APS-published article, can I post my article or a portion of my article on a web resource like wikipedia or quantiki?

Sites like wikipedia and quantiki are strict about permissions and require that authors hold copyright to articles that they post there. In order to allow authors to comply with this requirement, APS permits authors to hold copyright to a "derived work" based on an article published in an APS journal as long as the work contains at least 10% new material not covered by APS's copyright and does not contain more than 50% of the text (including equations) of the original article.

As the author of an APS-published article, will I hold copyright to a "derived work", as described above, even if the original article was published prior to 1 October 2008?

Yes. The APS will extend this author right to all papers published in APS journals.

As the author (or the author's employer) of an APS-published article, may I use copies of part or all of my article in the classroom?

Yes, the author or his/her employer may use all or part of the APS-prepared version for educational purposes without requesting permission from the APS as long as the appropriate bibliographic citation is included.

As the author of an APS-published article, may I use figures, tables, graphs, etc. in future publications?

Yes, as the author you have the right to use figures, tables, graphs, etc. in subsequent publications using files prepared and formatted by you or the APS-prepared versions. The appropriate bibliographic citation must be included.

As the author of an APS-published article, may I include my article or a portion of my article in my thesis or dissertation?

Yes, the author has the right to use the article or a portion of the article in a thesis or dissertation without requesting permission from APS, provided the bibliographic citation and the APS copyright credit line are given on the appropriate pages.

As the author of an APS-published article, may I give permission to a colleague or third party to republish all or part of the article in a print publication?

Yes, as the author you can grant permission to third parties to republish print versions of the article provided the APS-prepared version (e.g., the PDF from the online journal, or a copy of the article from the print journal) is not used for this purpose, the article is not published in another journal, and the third party does not charge a fee. The appropriate bibliographic citation and notice of the APS copyright must be included.

As the author of an APS-published article, may I give permission to a colleague or third party to republish all or part of the article in an online journal, book, database compilation, etc.?

Authors should direct the third party request to APS.

As the author of an APS-published article, may I provide a PDF of my paper to a colleague or third party?

The author is permitted to provide, for research purposes and as long as a fee is not charged, a PDF copy of his/her article using either the APS-prepared version or the author prepared version.

As a third party (not an author), may I republish an article or portion of an article published by APS?

Yes, APS will grant permission to republish articles or portions of articles (e.g., tables, graphs, excerpts) published by APS. Depending on the reuse and medium APS has the right to grant permission subject to APS terms and conditions and a fee may be assessed.

As a third party, may I use articles published by APS for lecture and classroom purposes?

Yes, you may use photocopied articles published by APS for lecture and classroom purposes for a single semester without asking permission from APS. However, if the article becomes part of your course material beyond one semester, you must obtain permission from APS. Also, there is no limitation on the use of APS articles using links to the material accessible through institutional subscriptions.

How do I request permission to republish APS-copyrighted material?

To request permission to republish APS-copyrighted material, please provide the following information:

1. Title of journal
2. Title of article
3. Name of author
4. Volume number, page number (or article identifier), year
5. Indicate if you are requesting to republish in print, online, CD-ROM, and/or other format
6. Indicate if you wish to republish all or portion of article; if a portion describe the specific material, e.g., figure numbers, excerpt
7. Indicate how the material will be used, e.g., in a book, journal, proceeding, thesis, etc.

8. Indicate the title of publication

9. Indicate the name of the publisher

10. Indicate whether or not a fee will be charged for the publication

All permission requests must be in writing (email is acceptable). Blanket permissions are not granted. Please note all requests are subject to APS terms and conditions and a fee may be assessed.

Please allow 5-7 business days for us to respond to a permission request provided all the above information is provided at the time of the request.

Send all permission requests to:

Associate Publisher
American Physical Society
One Physics Ellipse
College Park, MD 20740
Email: assocpub@aps.org

If your questions have not been addressed and you need further assistance, please call: 301-209-3283.

How do I provide a proper bibliographic citation and notice of the APS copyright?
Provide the following information in this order:

Authors names, journal title, volume number, page number (or article identifier), year of publication. "Copyright (year) by the American Physical Society."

Further information
For further information about copyright in general, please refer to the Library of Congress FAQ at: http://www.copyright.gov/help/faq/

Journals published by the American Physical Society can be found at http://publish.aps.org/

APS COPYRIGHT TRANSFER FORM can be found at http://forms.aps.org/author/copytrnsfr.pdf

FAQ Version: October 1, 2008

135

International Union of Crystallography:

permissions

Reuse permissions

Requests for permission to reuse material from this journal should be addressed to:

Managing Editor
IUCr Journals
5 Abbey Square
Chester CH1 2HU
UK

Email: med@iucr.org or click here

Please be sure to include the following information:

- The title, author(s) and page extent of the article you wish to republish, or, in the case where you do not wish to reproduce the whole article, details of the section(s) to be reproduced.
- The journal title, volume/issue number and year of publication in which the article appeared, and the page numbers of the article.
- Details of the publication in which you wish to reprint the Journal material.
- If the material is being edited or amended in any way, a copy of the final material as it will appear in your publication.
- Contact details for yourself, including a postal address.

If you wish to include material from **your own article** in a publication, prior permission is not required, subject to the following conditions:

- Reproduction is intended in a primary journal, secondary journal, CD-ROM, book or thesis.
- The original article in which the material appeared is cited.
- IUCr's copyright permission is indicated by the wording "Reproduced with permission of the International Union of Crystallography". In electronic form, this acknowledgement must be visible at the same time as the reused materials, and must be hyperlinked to **Crystallography Journals Online** (http://journals.iucr.org/).

Photocopying permissions

Teaching institutions with a current paid subscription to the journal may make multiple copies for teaching purposes without charge, provided such copies are not resold or copied. In all other cases, permission should be obtained from a reproduction rights organisation (see below) or directly from the Publisher.

Copyright Licensing Agency

Institutions based in the UK with a valid photocopying and/or digital license with the Copyright Licensing Agency may copy excerpts under the terms of their license. For further information go to CLA.

Copyright Clearance Center

Institutions based in the US with a valid photocopying and/or digital license with the Copyright Clearance Center may copy excerpts under the terms of their license, please go to CCC.

Other Territories:

Please contact your local reproduction rights organisation.

Useful links

- Detailed statement of author rights
- Obtaining copyright permission for published works

VITA

Gregory T. McCandless received his Bachelor of Science degree (industrial engineering) in December of 1999 and, after working in industry, he returned to Louisiana State University to obtain his Master of Science degree (chemistry) in December of 2008 (Professor Robert Hammer, research advisor). He would go on to work as a Research Associate at Louisiana State University in Professor Rongying Jin's condensed matter physics group.

Gregory would later continue his graduate studies in chemistry under the direction of Professor George Stanley and Dr. Frank Fronczek. He will graduate with a Doctor of Philosophy in chemistry from Louisiana State University in December of 2012.